

PROGRAMA DE DOCTORADO EN ENERGIAS RENOVABLES Y EFICIENCIA

TESIS DOCTORAL

INTEGRATION IMPROVEMENT OF DFIG-BASED WIND TURBINE INTO THE ELECTRICAL GRID

Presentada por Yassir EL KARKRI para optar al grado de
Doctor
por la Universidad Politécnica de Cartagena

Dirigida por:
Dr. Alexis Bonifacio Rey Boué
D. Hassan El Moussaoui
Dr. Tijani Lamhamdi

DOCTORAL PROGRAMME IN ENERGIAS RENOVABLES Y EFICIENCIA

PhD THESIS

INTEGRATION IMPROVEMENT OF DFIG-BASED WIND TURBINE INTO THE ELECTRICAL GRID

**Presented to the Technical University of Cartagena in
fulfilment of the thesis requirement for the award of
PhD**

Supervisors:
Dr.Alexis Bonifacio Rey Boué
Dr. Hassan El Moussaoui
Dr. Tijani Lamhamdi

Declaration of Authorship

I, Yassir EL KARKRI, declare that this thesis titled, ‘Integration Improvement of DFIG-based Wind Turbine Into The Electrical Grid’ and the work presented in it are my own. I confirm that:

- This work was done wholly or mainly while in candidature for a research degree at this University.
- Where any part of this thesis has previously been submitted for a degree or any other qualification at this University or any other institution, this has been clearly stated.
- Where I have consulted the published work of others, this is always clearly attributed.
- Where I have quoted from the work of others, the source is always given. With the exception of such quotations, this thesis is entirely my own work.
- I have acknowledged all main sources of help.
- Where the thesis is based on work done by myself jointly with others, I have made clear exactly what was done by others and what I have contributed myself.

Signed:

Date:

“It's one small step for man, one giant leap for mankind.”

Neil Armstrong

Abstract

This doctoral thesis in electrical engineering is presented as five research works linked together by the same theme. Five articles were published in indexed journals. In this sense, each of these works forms a piece of the puzzle constructed around the subject "wind farms integration into the electricity grid." To better understand the articulation between these works, this thesis is structured in three parts: The first part treats the Fault Ride Through (*FRT*) capability of the Grid-connected DFIG-based Wind Turbine. The first proposed approach is a hybrid method combining two methods (active and passive methods): The active method aims to develop the control of DFIG. In contrast, the passive method is applied for severe voltage faults using hardware protection circuits. Otherwise, the second proposed approach is a control design implemented to the power converters using Proportional- Resonant regulators in a stationary two-phase ($\alpha - \beta$) reference frame. The control performance is significantly validated by applying the real-time simulation for the rotor side converter and the hardware in the loop simulation technic for the experiment part of the generator's grid side converter control. This thesis's second part presents a new fault diagnosis and fault-tolerant control strategy for doubly fed induction generator with DC output based on predictive torque control. Generally, the current sensor failures can deteriorate the reliability and the performance of the control system and can lead to the malfunction of the predictive control strategy since the rotor- and stator flux cannot be estimated correctly. The proposed fault diagnosis can deal with all types of sensor faults. A non-linear observer adapted to the studied system to achieve smooth operation continuity when two or all the current sensors are faulty. The proposed approach's feasibility and robustness are achieved by testing different sensor faults on the stator- and rotor- current and under different operation mode cases. The third part focuses on calculating the wind capacity credit by integrating the Moroccan project on the wind energy of 1000 MW in 2020. After introducing the Moroccan Integrated Wind Energy Project, a wind capacity credit assessment program will be implemented on Matlab software, including the complete information about "installed capacity, number of plants, failure rate, types of installed units, peak demand, etc." This program will be used to calculate the safety rate of an electrical system as well as the capacity credit of Morocco's electricity production network. The research provides conclusions according to comments and assessment of the impact of this electric energy integration based on wind generation.

Acknowledgements

This research project has been carried out at the Electrical Engineering Department, at University of Sidi Mohamed Ben Abdellah. The financial support provided by " Erasmus + International Credit Mobility program (KA107) " and " L'Agence universitaire de la Francophonie AUF " is gratefully acknowledged. First of all, I would like to express my deep and sincere gratitude to my supervisors Prof. TIJANI LAMHAMDI et Prof. HASSAN EL MOUSSAOUI for his excellent supervision and helps during this work. I would like to thank all my professors at the Department of Electrical Engineering for all their technical, professional and administrative support. I want in special thanks to, Prof. HASSANE EL MARKHI, for encouraging my research and for allowing me to grow as a research scientist.

It is a pleasure for me to take the opportunity to thank all my colleagues in the research group. My greatest thanks go to the person, who aided me during my final stage of PhD work. I would like to express my deepest gratitude to Prof. Alexis Bonifacio Rey Boué, my supervisor at Universidad Politécnica de Cartagena - Spain (UPCT) and Prof. Sérgio Cruz my supervisor at the University of Coimbra - Portugal (UC), for all his guidance and support as well as teaching me numerous skills of doing scientific work.

Many thanks go to all my colleagues at Electrical Engineering, who have assisted me during the work of this Ph.D. thesis. I cannot begin to express my gratitude and appreciation for their friendship. Dr. SENHAJI KAOUTAR, CHAKIB CHATRI, MOHAMED AZEROUAL and HOMRANI NABIL for unwavering in their personal and professional support during my PhD journey.

Finally, most importantly, none of this could have happened without my family. I would like to dedicate a special thanks to my parents AHMED EL KARKRI and HAFIDA EL HOMRANI and my sister KAOUTAR EL KARKRI for supporting me spiritually throughout writing this thesis and my life in general. This dissertation stands as a testament to your unconditional love and encouragement ...

Contents

Declaration of Authorship	i
Abstract	iii
Acknowledgements	iv
List of Figures	viii
List of Tables	xi
Introduction	1
1 Résumé des travaux de recherche	6
1.1 Exigences du code de réseau électrique (LVRT et HVRT)	6
1.1.1 Stratégie LVRT utilisant des méthodes active et passive pour les défauts de réseau symétriques	7
1.1.1.1 Méthode active	7
1.1.1.2 Méthode passive	11
1.1.2 Stratégie HVRT pour les défauts de réseau symétriques	13
1.1.2.1 Contrôle de DVR	13
1.1.2.2 Contrôle du convertisseur coté machine	14
1.1.2.3 Contrôle de convertisseur coté réseau	16
1.1.3 Combinaison des méthodes HVRT et LVRT	17
1.1.4 Conclusion	18
1.1.5 Stratégie LVRT utilisant les Régulateurs Proportionnels Résonants pour les défauts de réseau symétriques	19
1.1.6 Conclusion	21
1.2 Diagnostic des défauts sur les capteurs du courant	22
1.2.1 Tolérance de défaut durant un capteur défectueux	22
1.2.2 Tolérance de défaut avec deux capteurs défectueux	24
1.2.2.1 Conclusion	26
1.3 Évaluation du crédit de capacité d'énergie éolienne: étude de cas du site nord-ouest du Maroc.	27
1.3.1 L'analyse du crédit de capacité	27
1.3.1.1 Modèle de production conventionnelle	29
1.3.1.2 Modèle de charge	29

1.3.1.3	Modèle probabiliste (Modèle de risque)	30
1.3.1.4	Conclusion	31
1.4	Conclusion général	32
2	LVRT and HVRT control strategies of Doubly-Fed Induction Generator	35
2.1	introduction	35
2.2	DFIG behaviour during grid faults	36
2.3	LVRT and HVRT Control Strategies	39
2.3.1	LVRT control strategy	39
2.3.1.1	Active method	40
2.3.1.2	Feasibility of the active method	43
2.3.1.3	Maximum amplitude of a voltage dip	43
2.3.1.4	Maximum duration of a voltage dip	45
2.3.1.5	The passive method	45
2.3.1.6	Series dynamic breaking resistor SDBR	47
2.3.2	HVRT control strategy	49
2.4	Combining HVRT and LVRT methods	53
2.5	Simulation & results	54
2.6	Conclusion	57
3	Improved Control of Grid-connected DFIG-based Wind Turbine using Proportional-Resonant Regulators during Unbalanced Grid	59
3.1	Introduction	59
3.2	DFIG Control	61
3.2.1	DFIG Control Strategy	63
3.2.2	Grid Side Converter Regulation using PR Control	66
3.3	Grid Code (Output Current Limitation)	69
3.4	Digital Real-Time Simulation of the Rotor Side Converter	70
3.5	Controller Hardware-in-the-Loop Simulation for the Grid Side Converter	72
3.6	Conclusion	77
4	Robust Current Sensors Fault detection and reconfiguration in DFIG-DC Drives.	80
4.1	Introduction	80
4.2	Current sensors fault diagnosis	82
4.2.1	Types of current sensor faults	82
4.2.2	Algorithm of sensor fault detection and localization	83
4.3	Fault-Tolerant Control	84
4.3.1	Fault tolerance with one sensor fault	84
4.3.2	One sensor Fault reconfiguration block	85
4.4	Experimental Results	87
4.4.1	Fault-tolerant for one sensor fault	88
4.4.2	Fault-tolerant for two sensor faults	91
4.5	Conclusion	92
5	Assessment of wind power capacity credit in Morocco: Outlook to 2020	93

5.1	Introduction	93
5.2	The reliability of production systems in the presence of wind	96
5.2.1	The CC analysis	97
5.2.2	Conventional production model	99
5.2.3	Load model	100
5.2.4	Probabilistic model (risk model)	101
5.3	Application to the TAZA wind farm	102
5.3.1	Wind production model for the TAZA Park	102
5.3.2	Capacity credit calculation	102
5.4	Generalization on the analysis of CC for wind capacity installed on the MNG by 2020	104
5.5	Conclusion	108
	Conclusion	110
	List of scientific contributions	112
	Bibliography	114

List of Figures

Figure 1 LVRT and HVRT requirments	3
Figure 1.1 La différence entre les flux stator et rotor pour 30% de creux de tension à t = 0,6s (a) sans contrôle et (b) avec contrôle de flux.	8
Figure 1.2 Le schéma de principe de contrôle.	9
Figure 1.3 Représentation de Fresnel de la tension statorique, pendant le défaut, avec SDBR.	12
Figure 1.4 Schéma de contrôle du DVR pendant les pics de tension du réseau.	14
Figure 1.5 Schéma de contrôle du convertisseur coté machine pendant les augmentations de tension du réseau.	15
Figure 1.6 Schéma de contrôle du convertisseur coté réseau pendant les augmentations de tension du réseau.	17
Figure 1.7 l'organigramme de la stratégie proposée basée sur la combinaison des méthodes HVRT et LVRT.	18
Figure 1.8 P-N SD block.	21
Figure 1.9 One sensor Fault reconfiguration block.	24
Figure 1.10 Principe de reconfiguration avec deux capteurs défectueux.	26
Figure 1.11 Modèle probabiliste pour l'analyse du CCE.	27
Figure 1.12 Algorithme de détermination du CCE.	28
Figure 1.13 le monotone de charge 2020.	30
 Figure 2.1 The difference between the stator and rotor fluxes for 30% of voltage dip at t = 0.6s (a) without control and (b) with control.	41
Figure 2.2 The control block diagram.	41
Figure 2.3 the reactive power for voltage dips a) 30% of voltage dips , b) 25% and c) 23%.	46
Figure 2.4 LVRT requirments	46
Figure 2.5 DFIG with SDBR	47
Figure 2.6 DFIG system with DVR.	49
Figure 2.7 Control diagram of DVR during grid voltage swells.	50
Figure 2.8 RSC control diagram during grid voltage swells.	52
Figure 2.9 GSC control diagram during grid voltage swells.	53
Figure 2.10 the flowchart of the proposed strategy based on the combination of HVRT and LVRT methods.	54
Figure 2.11 Grid voltage during tow voltage dips.	55
Figure 2.12 Simulation results of different electric quantities for the system with and without LVRT strategy.	56
Figure 2.13 Grid voltage during a voltage swell.	56

Figure 2.14 Simulation results of different electric quantities for the system with and without HVRT strategy.	57
Figure 2.15 Simulation results of different electric quantities for the system with and without HVRT strategy.	58
Figure 3.1 DFIG system connected to the utility grid.	61
Figure 3.2 The equivalent electrical circuit of the DFIG.	62
Figure 3.3 Park's and Clarke's transformation of the DFIG system.	63
Figure 3.4 MPPT power curve of the DFIG system.	65
Figure 3.5 The Schematic diagram of the rotor side converter control.	66
Figure 3.6 Schematic diagram of the grid side converter control.	68
Figure 3.7 P-N SD block.	68
Figure 3.8 (a) LVRT requirements according to IEC 61400-21 and (b) reactive power during voltage sag according to the Spanish grid code [19].	69
Figure 3.9 Organigram of the LVRT algorithm.	71
Figure 3.10 DRTS of the RSC control for (a): wind speed, (b) rotor speed, (c) rotor current, (d) electromagnetic torque.	72
Figure 3.11 The Grid-Side Power parameters.	73
Figure 3.12 Simulation results of the LVRT proposed strategy for symmetrical voltage sag of (0.1pu) under full nominal power.	74
Figure 3.13 Simulation results of the LVRT proposed strategy for symmetrical voltage sag of (0.1pu) under half nominal power.	75
Figure 3.14 Simulation results of the LVRT proposed strategy for symmetrical voltage sag of (0.3 pu) under full nominal power.	75
Figure 3.15 Simulation results of the LVRT proposed strategy for symmetrical voltage sag of (0.3 pu) under half nominal power.	76
Figure 3.16 Simulation results of the LVRT proposed strategy for asymmetrical voltage sag of (0.1 pu) under full nominal power.	77
Figure 3.17 Simulation results of the LVRT proposed strategy for asymmetrical voltage sag of (0.1pu) under half nominal power.	77
Figure 3.18 Simulation results of the LVRT proposed strategy for asymmetrical voltage sag of (0.5pu) under full nominal power.	78
Figure 3.19 Simulation results of the LVRT proposed strategy for asymmetrical voltage sag of (0.5pu) under half nominal power.	78
Figure 4.1 One sensor Fault reconfiguration block.	85
Figure 4.2 Flowchart of the proposed sensor fault diagnosis algorithm.	85
Figure 4.3 Two sensor fault reconfiguration principle.	88
Figure 4.4 Simulation results obtained in the case when a noise signal occurs in phase 'a' of the rotor current sensor.	89
Figure 4.5 Simulation results obtained in the case when the sensor in phase 'b' of the rotor current is completely out of order.	89
Figure 4.6 Simulation results obtained in the case when the sensor in phase 'c' of the rotor current is saturated.	90
Figure 4.7 Simulation results obtained in the case when a gain error occurs in phase 'a' of the stator current sensor.	90
Figure 4.8 Simulation results obtained in the case when an offset signal occurs in phase 'b' of the stator current sensor.	90

Figure 4.9 Simulation results obtained in the case when two sensor faults occur in phase 'a' and 'b' of the stator current.	92
Figure 4.10 Simulation results obtained in the case when two sensor faults occur in phase 'a' and 'b' of the rotor current.	92
Figure 5.1 Map of the average wind speed in Morocco (m/s) [74].	94
Figure 5.2 Evaluation model of the adequacy of the electricity production systems.	97
Figure 5.3 The probabilistic model for wind CC analysis.	98
Figure 5.4 CC determination algorithm.	99
Figure 5.5 The monotone of load in 2020.	101
Figure 5.6 Wind distribution in the TAZA park.	103
Figure 5.7 Safety ratio according to the injected wind capacity for 30 MW and 33 MW withdrawn.	104
Figure 5.8 Safety rate (LOLE) according to the injected wind capacity. . . .	107
Figure 5.9 The capacity credit and the wind capacity injected according to the removed conventional capacity.	108

List of Tables

Table 1.1	La compatibilité de la méthode active avec les codes réseau	11
Table 1.2	Puissance installée sur le réseau électrique national ([21].	29
Table 1.3	MNG reliability level.	31
Table 2.1	DFIG parameters	55
Table 3.1	DFIG system parameters.	72
Table 3.2	The Grid-Side Power parameters.	73
Table 3.3	The Grid-Side Power parameters.	73
Table 4.1	Types of a sensor faults.	83
Table 5.1	Power installed on the national power grid ([21].	100
Table 5.2	MNG reliability level.	102
Table 5.3	Reliability of the hybrid park (conventional + wind).	103
Table 5.4	The wind CC of the park of TAZA.	104
Table 5.5	The wind capacities planned to be installed in Morocco before 2020.	105
Table 5.6	The conventional capacity installed in Morocco by 2020.	106
Table 5.7	The LOLE (h/year), CC, and the IWC for each conventional capacity removed.	107

Nomenclature

DFIG Doubly Feed Induction Generator

DVR Dynamic Voltage Restorer

FRT Fault Ride Through

GSC Grid Side Converter

HVRT High Voltage Ride Through

LVRT Low Voltage Ride Through

P – NSC Positive and Negative Sequence

PR Proportional Resonant

RSC Rotor Side Converter

SDBR Serie Dynamic Braking Resistor

WT Wind turbine

Introduction

Scientific and technical interests of the thesis

The electrical power is an essential factor for the development and evolution of human societies, whether in terms of improving living conditions or the development of industrial activities. It has become an essential form of energy through its flexibility of use and the multiplicity of activities fields where it can play a more important role. The modes and associated means of production are going to undergo profound changes in the coming decades. Production methods based on the transformation of renewable energies (wind, solar, etc.) are expected to be used more and more in the context of sustainable development.

With the massive development of wind power, the technical prescriptions for connecting this technology will force the maintenance of its connection during incidents on the voltage of the electrical network. The challenge for the network manager is to be able to use all the generators to guarantee the stability of the electrical system and to maintain the balance between production and consumption at all times. Energy must be available immediately when the customer needs it. Indeed, the fact that voltage dips and interruptions can disrupt many devices connected to the network, they are the most common cause of energy quality problems. A drop in voltage or a cutoff of a few hundred milliseconds can have harmful consequences for several hours.

The national specifications and standards required wind turbines to remain connected during a voltage disturbance which normally imposed by the network. For example, during a grid fault or a sudden change in the grid frequency, a destabilization of the wind production system is observed and its internal protections disconnect it. However, with the development of wind energy, the interactions between wind turbines and the power grid must be taken into account. This is all the more true since, when the wind production turbines are disconnected from the grid, they can no longer be used by the grid operator to ensure the voltage and frequency stability of the grid in this fault situation, unlike conventional production systems. This is one of the major causes of the loss of stability in high wind turbine systems.

As wind power potential has amplified, so has the necessity for wind farms to become more dynamic in keeping the grid safety and power quality of the grid [1, 2]. This raised situation into the power-market drives us to serious questions about its capacity to provide ancillary services, such as the imbalance and loss compensation, thus the voltage-frequency regulation during grid fault. In this conditions, Grid Operators are getting to be plainly stricter with the utilization of wind power as far as their behavior compared to traditional power sources [1]. This limited utilization of wind power sources is executed through a continuous refreshing of their grid codes [3?]. where the technical conditions requested for wind power plants are stricter, or much more critical, than those for conventional energy sources [4]. The grid codes technical specifications are classified into two categories: (i) static and (ii) dynamic requirements. The static requirements talk about the steady-state behavior and the power quality at the connection point to the grid [5]. While the dynamic obligations concern the desired Wind turbine (WT) generator response during fault times. Usually, these requirements cover many subjects such as voltage operation range, control of power factor, frequency operation range, and fault ride through [6].

Moreover, since the Doubly Feed Induction Generator (DFIG) is the most commonly used machine in production units larger than 1MW, the value of *DFIG* based wind turbines is becoming more and more important as is appropriate for advanced features accomplishing grid integration [7]. DFIG grants some profits, such as reduced costs of power-inverter and output filter due to low power conversion ratings of rotor side and grid side (25%–30%) [8], However, wind turbines based on DFIG are so delicate to grid disturbances, especially to Voltage Dips and Voltage Swells [9].

Grid codes requirements mostly apply to wind farms connected to the transmission lines. These grid codes indicate that wind farms should keep the power system control, and assert wind farm behavior in case of irregular functioning states of the grid (in case of voltage dips and voltage swells). The several general requirements introduce *FRT* capability, active power control, frequency control, and power factor regulation abilities [10]. The typical grid codes principal requirements are given below:

- Frequency functioning area: Wind farms are obliged to operate continuously within usual grid frequency variations.

- Active power: Wind farms must have the capacity to control their active power in order to guarantee a stable operating and to prevent overloading of the grid and to diminish the effect of dynamic WT operation through extreme wind conditions.
- Reactive power: Wind farms should remain the reactive power stability and kept the power factor in the desired area.
- LVRT and HVRT: During grid voltage faults, WTs need to remain connected for a specific time before being allowed to disconnect.

These requirements are needed to guarantee that there is no generation loss for normally cleared faults. Disconnecting a WT rapidly could have a negative impact on the grid, particularly for big wind farms. Grid codes require that WTs must resist voltage variation at a specified rate of the nominal voltage and for a specified duration. Such constraints are known as LVRT (for voltage dips) and HVRT (for voltage swells). They are represented by a voltage (U) versus time (t) characteristic, indicating the minimum required protection of the wind power farms to the system voltage variations (Figure.1) [11].

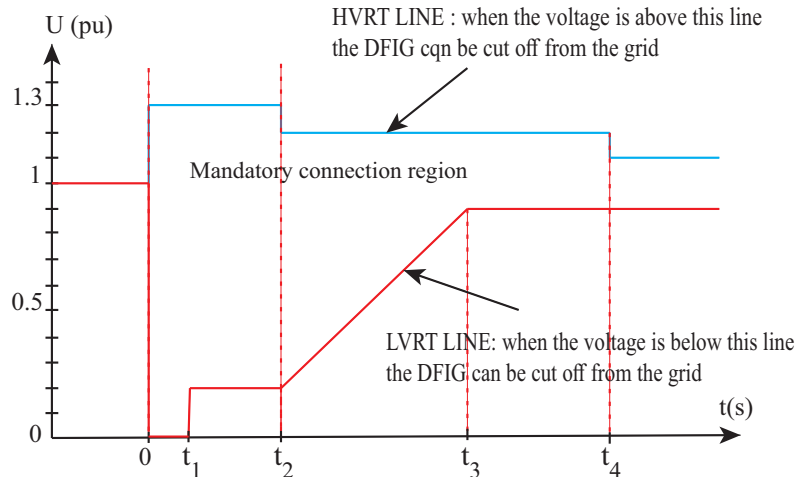


Figure. 1. LVRT and HVRT requirements

In this thesis two contributions are proposed and will be presented in the first and the second chapter for the fault ride through control strategies of Doubly-Fed Induction Generator,

Otherwise, since the DFIG control system is related to the sensor measurements, it is sure that the response of the system control can be influenced by sensor faults. Also,

most of the research literature focuses on power converters faults, especially open- and short- circuit faults, and the majority of available diagnosis methods are based on the current sensors [12, 13]. Thus, sensor faults can damage the power electronics components or even the entire system which can lead to losing the energy production unit. In fact, the development of sensor faults detection, isolation and reconfiguration are necessary to avoid the aforementioned effects and to ensure the safe operation of the energy production system. In order to improve the quality of the produced energy, a novel strategy is proposed for sensor fault diagnosis based just on the measured current will be presented on the third chapter.

In the same way, the long-term aspects cannot be decoupled from the analysis of the wind turbines's integration into the grid. Therefore, the profit potential of wind power is measured according to its capacity to replace conventional park of production (thermal, Coal . . .). Due to the intermittent nature of the wind, wind power cannot be guaranteed at all times. This will result in the need for additional capacity to be activated when the wind turbine is unavailable. This situation requires an assessment of the long-term wind profile and an estimate of the possible impact of the wind on the reliability of the system. The answers to these questions go through the study of the wind power capacity credit.

Thesis organization

The report for this thesis is organized as follows: The first chapter named "Résumé des travaux de recherche", presents a summary of all the thesis chapters.

After the first introductory chapter, the first contribution is presented, based on the developing of low- and high- voltage ride-through capability of the DFIG during symmetrical grid voltage faults. The proposed strategy for LVRT combines the active method to limit fault in current at low voltage dips and the passive method for severe voltage dips by adding hardware protections (series breaker resistor). The proposed solution for HVRT capability involves the use of a Dynamic Voltage Restorer (*DVR*) to maintain DFIG terminal voltage stable and to provide maximum support to help the grid voltage fast recovery by controlling power converters.

For the third chapter, the second contribution for LVRT is presented. This work explores an application of the Proportional Resonant (*PR*) regulators on the DFIG's Grid Side Converter (GSC), mainly in their capability for the compensation of reactive power, grid current limitation and the stabilization of active power during a grid fault. The work novelty can be observed in the LVRT proposed algorithm according to the IEC 61400-21 normative and the Spanish grid code, generating the Positive and Negative Sequence (P-N SC) of the grid currents with the implementation of the *PR* regulators on the DFIG's Grid Side Converter (GSC) to the $\alpha\beta$ components of the 3-phase inverter currents. This feature will have the capability for the compensation of reactive power and the grid current limitation during a grid fault according to the Spanish grid code.

The forth chapter, in order to increase the safe operation of the DFIG system a novel strategy is proposed for current sensor fault diagnosis based just on the measured current, the algorithm is valid for real-time implementation due to its moderate computational burden, and can deal with different sensor faults. When just one sensor fault is detected, the healthy sensors are used to compensate the faulty sensor, while, when two or all the sensors are faulty a non-linear observer proposed in [14] for a Wound Rotor Synchronous Machine (WRSM) is developed to be compatible with the studied system (DFIG-DC).

In the sixth chapter, a study on the long-term impact of wind power production is necessary, by introducing the concept of wind capacity credit, to predict for which level in terms of capacity and flexibility the wind power can replace conventional power plants.

Chapter 1

Résumé des travaux de recherche

Cette thèse de doctorat en électrotechnique se présente sous la forme de travaux de recherche, reliés entre eux par une même thématique. Cinq articles ont été publiés dans des revues indexées. Ces travaux bien que distincts dans la forme et dans le contenu démontrent une complémentarité au niveau de la thématique de recherche. En ce sens, Chacune de ces travaux forme une pièce du puzzle qui a été reconstruit autour du sujet "l'intégration des parcs éoliennes dans le réseau électrique". Afin de mieux comprendre l'articulation entre ces travaux, cette thèse est structurée en trois volets:

- Le premier volet aborde les problèmes de raccordement des parcs éoliens au réseau électrique, dans cette partie deux méthodes de contrôle sont appliquées pour la capacité éolienne LVRT ainsi qu'une méthode pour la capacité éolienne HVRT;
- Le deuxième volet présente une nouvelle stratégie de diagnostic de défaut et de commande en prenant au compte les pannes des capteurs de courant pour une machine DFIG;
- le troisième volet est une étude de l'impact de la production intermittente à long terme, afin de déterminer le crédit de capacité éolienne.

1.1 Exigences du code de réseau électrique (LVRT et HVRT)

Le premier volet traite les problèmes de raccordement des parcs éoliens au réseau électrique. La pénétration accrue de l'énergie éolienne et de l'installation des parcs

éolienne concentrée, la déconnexion des aérogénérateurs en raison des conditions de creux de tension ou des surtensions peuvent provoquer de graves problèmes sur la stabilité du système d'alimentation [15]. Après le passage de défaut de réseau, les conditions de surtension peuvent être induites s'il n'y a pas de contrôle automatique rapide de la puissance réactive, ensuite les éoliennes seront déclenchées en raison des conditions de surtension et surintensité. Dans de nombreux codes réseau les parcs éoliennes nécessitent de rester connectés au réseau durant les conditions de chute de tension et de surtension, appelées exigence LVRT (Low Voltage Ride Through) et HVRT (High Voltage Ride Through) [15].

Ainsi, l'objet de cette étude est de contribuer à la recherche d'une solution fiable qui permet aux éoliennes à base de DFIG de résister à des chutes de tension et des surtensions, en utilisant des solutions qui sont plus simples que celles présentées dans la littérature. Dans cette thèse, deux stratégies sont proposées pour la capacité LVRT et une pour la capacité HVRT.

1.1.1 Stratégie LVRT utilisant des méthodes active et passive pour les défauts de réseau symétriques

Deux méthodes de contrôle sont appliquées pour la capacité éolienne LVRT, en fonction du niveau de chute de tension. La première méthode (méthode active) est basée sur le contrôle du flux afin de limiter la surintensité du rotor, cette méthode n'est valable que pour de faibles profondeurs de creux de tension. Alors que la deuxième méthode (méthode passive) nécessite des protections matérielles telles que les résistances série (SDBR) pour minimiser les effets de creux de tension importants.

1.1.1.1 Méthode active

L'objectif principal du contrôle en cas de défaut réseau est de limiter le courant de défaut. Le procédé est simple à mettre en œuvre, basé sur le contrôle du flux rotorique ϕ_r lorsqu'un creux de tension est détecté. Le principe est de contrôler le flux rotorique lors des creux de tension du réseau pour suivre le flux statorique ϕ_s . Ainsi, la surintensité du rotor peut être définitivement réduite

l'expression du courant rotorique est exprimée comme suit:

$$i_r = \frac{1}{L_s L_r - M^2} (-M\phi_s + L_s \phi_r) \quad (1.1)$$

avec $\frac{M}{L_s} \simeq 1$

$$i_r = \frac{M}{L_s L_r - M^2} (\phi_r - \phi_s) \quad (1.2)$$

Avec: i_r et i_s sont les courant rotorique et statorique; ϕ_r et ϕ_s les flux rotorique et statorique; L_r , L_s et M sont respectivement les inductances rotorique, statorique et mutuel.

L'équation 1.2 montre que le courant du rotor dépend de la différence entre la liaison de flux rotorique et statorique. Lorsque des défauts de réseau se produisent, le flux rotorique ne peut pas suivre correctement le flux statorique et la différence entre Φ_s et Φ_r devient très importante, ce qui entraînera une surintensité dans les enroulements du rotor. Par conséquent, afin de le réduire lors des creux de tension, le flux du rotor doit être contrôlé pour suivre le flux du stator. La figure 1.1.(a) et la figure 1.1.(b) montrent la différence entre les flux statorique et rotorique pour 30% de creux de tension à $t = 0,6s$ avec et sans contrôle du flux rotorique.

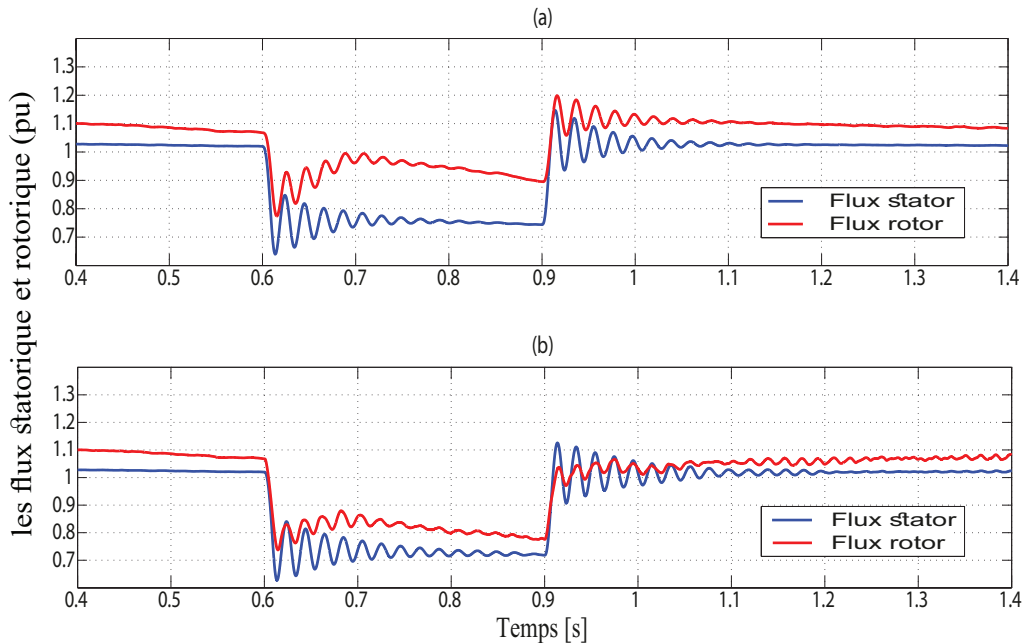


Figure. 1.1. La différence entre les flux statorique et rotorique pour 30% de creux de tension à $t = 0,6s$ (a) sans contrôle et (b) avec contrôle de flux.

La figure 1.2 montre le schéma de principe de commande, est constitué de trois parties. Le flux rotorique et statorique sur l'axe d-q sont estimés en fonction des courants du rotor et du stator dans le premier bloc appelé 'Flux linkage detection'. Ensuite, la référence du flux rotorique est calculée en fonction du flux statorique estimé. Enfin, dans le bloc de commande 'Rotor flux linkage control', les tensions de rotor d'axe d-q et les tensions de rotor sont établies.

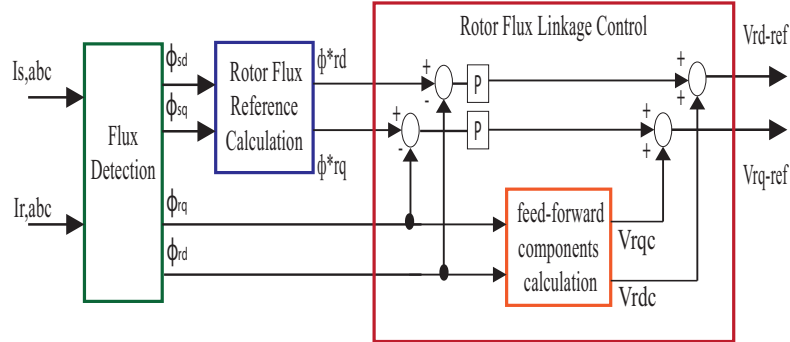


Figure. 1.2. Le schéma de principe de contrôle.

Le rôle du bloc de référence 'Rotor flux reference calculation block' est de déterminer les références du flux rotorique qui peut être calculée par l'équation suivant:

$$\phi_r^* = k_T \phi_s \quad (1.3)$$

Où $0 < k_T < 1$ est le gain de suivi. En substituant l'équation 1.3 à l'équation 1.2, le courant du rotor peut être exprimé par l'équation:

$$i_r \simeq \frac{L_s(k_T - 1)}{L_s L_s - M^2} \phi_s \quad (1.4)$$

A partir des équations 1.3 et 1.4, le courant du rotor peut être contrôlé pour être plus petit avec un k_T plus grand. Nous pouvons calculer la valeur minimale de k_T comme suit; lorsqu'un défaut de réseau se produit, le flux statorique augmente. En d'autres termes, la valeur initiale du flux statorique est la plus grande pendant les creux de tension, et son amplitude peut être donnée approximativement par $\phi_s(0) = \frac{V_s}{\omega_s}$. le courant du rotor pendant la chute de tension du réseau ne dépassera pas le courant maximum autorisé.

Donc k_T devrait satisfaire la condition exprimée par l'équation suivant:

$$\left| \frac{L_s(k_T - 1)}{L_s L_s - M^2} \phi_s(0) \right| \leq |I_{r,\max}| \quad (1.5)$$

Où $I_{r,\max}$ est le courant rotorique. Alors l'expression de la valeur minimale de k_T peut être exprimée comme suit:

$$k_{T,\min} \simeq 1 - I_{r,\max} \frac{\omega_s(L_s L_s - M^2)}{V_s L_s} \quad (1.6)$$

Un contrôleur proportionnel (P) est utilisé pour générer un signal à partir de la soustraction des références de flux du rotor de l'axe d-q et le flux du rotor de l'axe dq [3]. Ensuite, les références de tensions du rotor de l'axe d-q sont obtenues en ajoutant la sortie de la boucle de commande aux tensions du rotor de l'axe d-q (équations 1.7 et 1.8). Dans le calcul des composants par anticipation, les tensions du rotor de l'axe dq sont calculées selon le flux rotor de l'axe dq (équations 1.9 et 1.10).

L'intérêt d'utiliser le contrôleur P au lieu du contrôleur PI, est de maintenir le flux du rotorique proche du flux du statorique au lieu de la maintenir avec précision [3].

$$V_{rd-ref} = k_P(\phi_{rd}^* - \phi_{rd}) + V_{rdc} \quad (1.7)$$

$$V_{rq-ref} = k_P(\phi_{rq}^* - \phi_{rq}) + V_{rqc} \quad (1.8)$$

Où k_P est le gain du contrôleur proportionnel, V_{rdc} et V_{rqc} , définis comme:

$$V_{rdc} = \frac{R_r M}{L_s L_r - L_s^2} \phi_{sd} + \omega_{sr} \phi_{qd} \quad (1.9)$$

$$V_{rqc} = \frac{R_r M}{L_s L_r - L_s^2} \phi_{sq} + \omega_{sr} \phi_{rd} \quad (1.10)$$

La méthode active est limitée contre les fortes creux de tension. Le choix des convertisseurs de puissance utilisés dans le système peut contribuer à cette limitation.

Table. 1.1. La compatibilité de la méthode active avec les codes réseau

Niveau de chute de tension	Durée	Grid codes
30%	0.3s	—
25%	1s	Spain – Danemark-UK
23%	1.5s	Spain – Danemark-UK-Allemand
<23%	>1.5s	Spain – Danemark-UK-Allemand

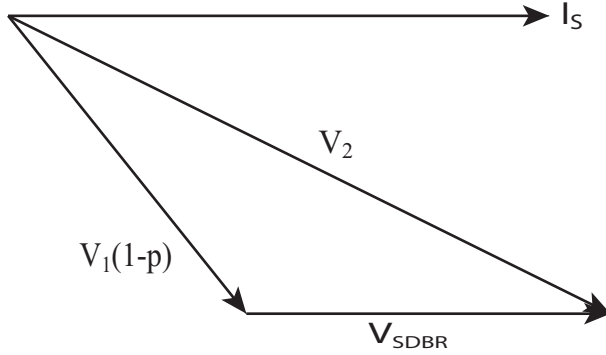
En fait, la modification de la conception des convertisseurs de puissance peut affecter le coût du système, ce qui n'est pas souhaitable. Par conséquent, l'utilisation de la méthode active contre les chutes de tension n'est pas recommandée. Le problème lors d'un défaut est que la puissance réactive doit rester dans les limites imposées par le code réseau. Ainsi, seulement 0,3pu de puissance réactive pourrait être tolérée. Donc, une chute de tension causée par un défaut de réseau doit être étudiée. C'est un fait connu qu'un creux de tension est caractérisé par deux paramètres: l'amplitude et la durée. L'amplitude maximale est théoriquement démontrée qu'elle peut rester valable pour les creux de tension inférieurs à $0,3 = 30\%$., Tandis que la durée du creux maximal est obtenue par simulation. La démonstration théorique et la simulation sont présentées au chapitre 2.

Le tableau 1.1 illustre les extrêmes de fonctionnement de la stratégie active, aux niveaux d'amplitude et de durée des creux de tension pour vérifier sa compatibilité avec des codes de réseau existants [16].

1.1.1.2 Méthode passive

L'approche passive est une méthode basée sur l'ajout des résistances connectées en série avec des enroulements de stator. Cette approche présente plusieurs avantages lors de défauts réseau tels que l'augmentation de la tension du stator figure 1.3 et la réduction des courants du stator et du rotor, l'atténuation du couple électrique et les fluctuations de puissance active. Une étude de conception SDBR et son impact sur le comportement du système lors d'un défaut de réseau est nécessaire. Les valeurs extrêmes du SDBR peuvent être définies par deux conditions.

1. La première valeur extrême du SDBR est calculée pour éviter la perte de contrôle du convertisseur coté rotor. Ainsi, la valeur minimale de résistance qui doit pouvoir protéger le convertisseur coté rotor contre la surtension du rotor pendant une



V_{SDBR} : la tension aux bornes de la résistance

p: degré de chute de tension

V_2 : tension du stator pendant la chute de tension

Figure. 1.3. Représentation de Fresnel de la tension statorique, pendant le défaut, avec SDBR.

chute de tension totale doit être calculée. l'équation 1.11 exprime le cas où la valeur de la tension du rotor pendant 100% du creux de tension ne doit pas dépasser la tension maximale du convertisseur coté rotor.

$$e_{r0,max}^r \leq V_{RSC,max} \quad (1.11)$$

2. La deuxième valeur extrême du SDBR est utilisée pour la protection des enroulements du stator contre les surtensions lors des défauts de réseau. Par conséquent, cette protection est fournie par la valeur maximale de la résistance. Cette valeur de résistance doit pouvoir ne pas dépasser la tension maximale du stator en cas de défaut du réseau. L'équation 1.12 indique la condition dans laquelle la valeur de tension maximale SDBR s'ajoutant à la tension du réseau ne doit pas dépasser la tension maximale du stator.

$$V_{SDBR,max} + V_1(1 - p) \leq V_{Smax} \quad (1.12)$$

Les valeurs extrêmes du SDBR calculées selon les conditions mentionnées précédemment ont été données par l'équation 1.13:

$$0.05pu \leq R_{SDBR} \leq 1.25pu \quad (1.13)$$

1.1.2 Stratégie HVRT pour les défauts de réseau symétriques

La deuxième stratégie proposée pour l'exigence HVRT, est réalisée par l'ajout d'un nouveau convertisseur côté réseau (Dynamic Voltage Restorer : DVR), qui supprime la composante continue transitoire du flux dans le stator. La surtension et la surintensité de la Machine Asynchrone à Double Alimentation peuvent être éliminées et aussi les fluctuations du couple électromagnétique peuvent être supprimées. De plus, en contrôlant le convertisseur côté machine et le convertisseur côté réseau, cette stratégie peut contrôler la puissance réactive transitoire pour soutenir le réseau pendant le défaut.

1.1.2.1 Contrôle de DVR

Le but du DVR pendant les pics de tension est de maintenir la stabilité de la tension sur le point de connexion avec le réseau, ainsi, en le contrôlant pour maintenir l'état avant défaut de la tension du réseau comme:

$$V'_g = V_g \quad (1.14)$$

Où: V_g est la tension du réseau pendant le fonctionnement normal;

V'_g est la tension du réseau pendant les augmentations de tension;

Pendant le fonctionnement normal, V_g est orienté suivant le d-axix, par le contrôle DVR, la tension au point de connexion peut être contrôlée pour garder le même état avant les augmentations de tension.

le vecteur de tension du réseau pendant un défaut réseau peut être exprimé comme suit:

$$\begin{cases} V_g = u_{gd} = V'_{gd} \\ 0 = u_{gq} = V'_{gq} \end{cases} \quad (1.15)$$

Où: u_{gd} et u_{gq} sont les vecteurs de tension du stator pendant le fonctionnement normal;

V'_{gd} et V'_{gq} sont des tensions de réseau pendant le défaut;

V_g est l'amplitude de la tension du réseau en fonctionnement normal.

Ainsi les équations de tension du DVR sont exprimées comme suit:

$$\begin{cases} U_{gcd} = [Kp_1(\tau_{i1}s + 1)/(\tau_{i1}s)](V_g - V'_{gd}) \\ U_{gcq} = [Kp_1(\tau_{i1}s + 1)/(\tau_{i1}s)](0 - V'_{gq}) \end{cases} \quad (1.16)$$

Où: K_{p1} et τ_{i1} sont des paramètres du contrôleur PI;

U_{gcd} et U_{gcq} sont les sorties du contrôleur PI.

Selon l'équation 1.16, le bloc de contrôle du DVR pendant un défaut de réseau est montré sur la figure 1.4.

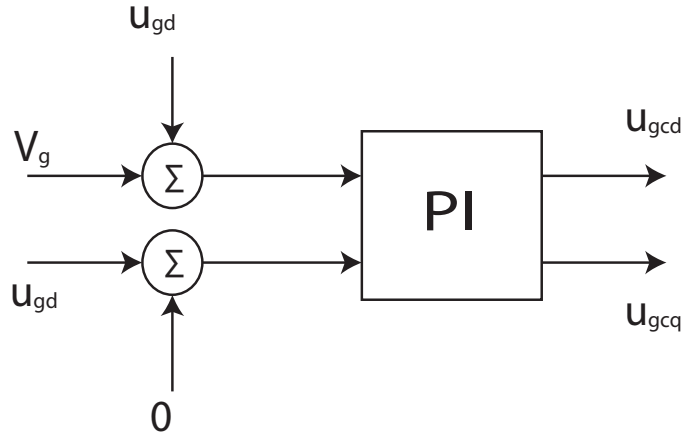


Figure. 1.4. Schéma de contrôle du DVR pendant les pics de tension du réseau.

1.1.2.2 Contrôle du convertisseur côté machine

Afin d'améliorer la capacité HVRT du système pendant les pics de tension, la stratégie de commande conventionnelle du convertisseur de puissance doit être modifiée pour éviter d'une part, les perturbations du courant du rotor et du stator et les oscillations de couple électromagnétiques. D'autre part, pour stabiliser la puissance réactive en contrôlant le convertisseur de puissance. Lors d'un défaut symétrique, la puissance active P_s et la puissance réactive Q_s du générateur peuvent s'écrire:

$$\begin{cases} P_s = V_{sq}i_{sq} = V_s i_{sq} \\ Q_s = V_{sq}i_{sd} = V_s i_{sd} \end{cases} \quad (1.17)$$

Où: V_{sd} V_{sq} sont les composants d-q du tension statorique;

i_{sd} i_{sq} sont les composants d-q du courant statorique.

D'après l'équation 1.17, afin de conserver le même état de puissance active, le vecteur de l'axe q du courant statorique doit rester stable; et afin de soutenir le réseau pendant les défauts en maximisant l'absorption de la puissance réactive, donc la composante de l'axe d du courant statorique doit prendre sa valeur maximale:

$$I_{sdmax} = \sqrt{I_{smax}^2 - I_{sq}^2} \quad (1.18)$$

Où: I_{smax} pour la valeur maximale du courant statorique.

les composantes de l'axe d-q du courant du rotor peuvent être exprimées:

$$\begin{cases} I_{rd} = \frac{\Phi_s}{L_m} - \frac{L_s}{L_m} i_{sdmax} \\ I_{rq} = -\frac{L_s}{L_m} i_{sq} \end{cases} \quad (1.19)$$

Ainsi, les équations pour le bloc de contrôle du convertisseur coté machine pendant les augmentations de tension sont exprimées par:

$$\begin{cases} V'_{rd} = \left[\frac{K_{p2}(\tau_{i2}s+1)}{\tau_{i2}s} \right] (I_{rd} - i_{rd}) \\ V'_{rq} = \left[\frac{K_{p2}(\tau_{i2}s+1)}{\tau_{i2}s} \right] (I_{rq} - i_{rq}) \end{cases} \quad (1.20)$$

Où:

V'_{rd} and V'_{rq} sont respectivement les composantes des axes d et q de la tension de sortie du contrôleur de boucle de courant;

K_{p2} and τ_{i2} sont des paramètres du contrôleur PI.

Le bloc de contrôle de convertisseur coté machine pendant les augmentations de tension est représenté sur la figure 1.5.

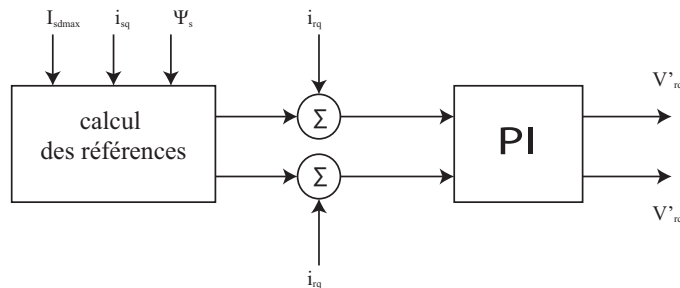


Figure. 1.5. Schéma de contrôle du convertisseur coté machine pendant les augmentations de tension du réseau.

1.1.2.3 Contrôle de convertisseur coté réseau

Lorsque l'amplitude de la tension du réseau augmente, la machine doit absorber la puissance réactive en fonction de l'amplitude du tension du réseau. Lorsque le convertisseur coté réseau utilise la méthode de contrôle vectoriel orienté; la tension de sortie est exprimée comme suit:

$$\begin{cases} U_g = -\omega_s L_g I_{gq} + V_{gd} \\ 0 = \omega_s L_g I_{gd} + V_{gq} \end{cases} \quad (1.21)$$

Où: U_g est l'amplitude du vecteur du tension de réseau;

L_g est l'inductance de ligne;

V_{gd} et V_{gq} sont respectivement des composantes d'axe d et d'axe q de la tension de sortie du convertisseur coté réseau;

I_{gd} et I_{gq} sont des composantes d'axe d et d'axe q du courant du convertisseur coté réseau.

Selon la théorie de la modulation vectorielle, en l'absence de condition de surmodulation, le rapport de modulation m doit satisfaire:

$$m = \left[\frac{\sqrt{V_{gd}^2 + V_{gq}^2}}{\frac{U_{dc}}{2}} \right] \leq 2/\sqrt{2} \quad (1.22)$$

d'après les équations 1.21 et 1.22 nous pouvons déduire:

$$U_{dc} \geq \sqrt{3[(V_g + \omega_s L_g I_{gq})^2 + (-\omega_s L_g I_{gd})^2]} \quad (1.23)$$

À partir de l'équation 1.23, le courant réactif minimum I_{gqmin} requis peut être exprimé comme:

$$I_{gqmin} = \frac{1}{\omega_s L_g} \left[\sqrt{\frac{U_{dc}^2}{3} - (-\omega_s L_g I_{gd})^2} - V_g \right] \quad (1.24)$$

Pendant la tension du réseau augmente; pour atteindre l'exigence HVRT, le GSC doit absorber au moins la puissance réactive minimale Q_{gmin} exprimée par:

$$Q_{g\min} = -I_{q\min} U_g \quad (1.25)$$

Ainsi, les équations pour le contrôle de la boucle de courant du convertisseur coté réseau sont:

$$\begin{cases} V'_{gd} = \left[\frac{K_{p3}(\tau_{i3}s+1)}{\tau_{i3}s} \right] (I_{gd} - i_{gd}) \\ V'_{gq} = \left[\frac{K_{p3}(\tau_{i3}s+1)}{\tau_{i3}s} \right] (I_{gq} - i_{gq}) \end{cases} \quad (1.26)$$

Le bloc de contrôle de convertisseur coté réseau pendant les défauts de réseau est montré dans la figure 1.6.

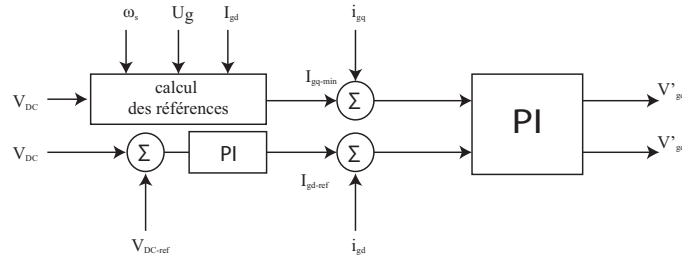


Figure. 1.6. Schéma de contrôle du convertisseur coté réseau pendant les augmentations de tension du réseau.

1.1.3 Combinaison des méthodes HVRT et LVRT

Pour assurer une bonne gestion de tous les types de défaut de réseau, nous proposons une stratégie de combinaison entre les stratégies LVRT et HVRT. La figure 1.7 montre l'algorithme de stratégie FRT proposé. En fonctionnement normal, la tension de réseau est mesurée en temps réel pour examiner les défauts de réseau et sa nature. Un défaut est testé en mesurant en temps réel la tension du réseau électrique. De plus, lors des creux de tension inférieur à 30%, la tension mesurée est comprise entre 0,7pu et 0,9pu, seule la méthode active est utilisée (Figure 1.7, option 1). Ainsi, dans cette plage, la méthode active est plus cohérente et la protection SDBR ne fonctionne pas. En revanche, pour des creux de tension élevés supérieurs à 30%, lorsque la tension mesurée dépassant 30%, seul la SDBR est utilisé avec le contrôle conventionnel (Figure 1.7, option 2). De plus, si les surtensions sont supérieure à 10%, la tension mesuré est supérieur à 1,1pu, la stratégie HVRT est activée (Figure 1.7, option 3) avec le contrôle proposé adaptant

l'amélioration de la sécurité et la stabilité du réseau sous le défaut. Finalement, au moment de la suppression du défaut, le système répond à un fonctionnement normal.

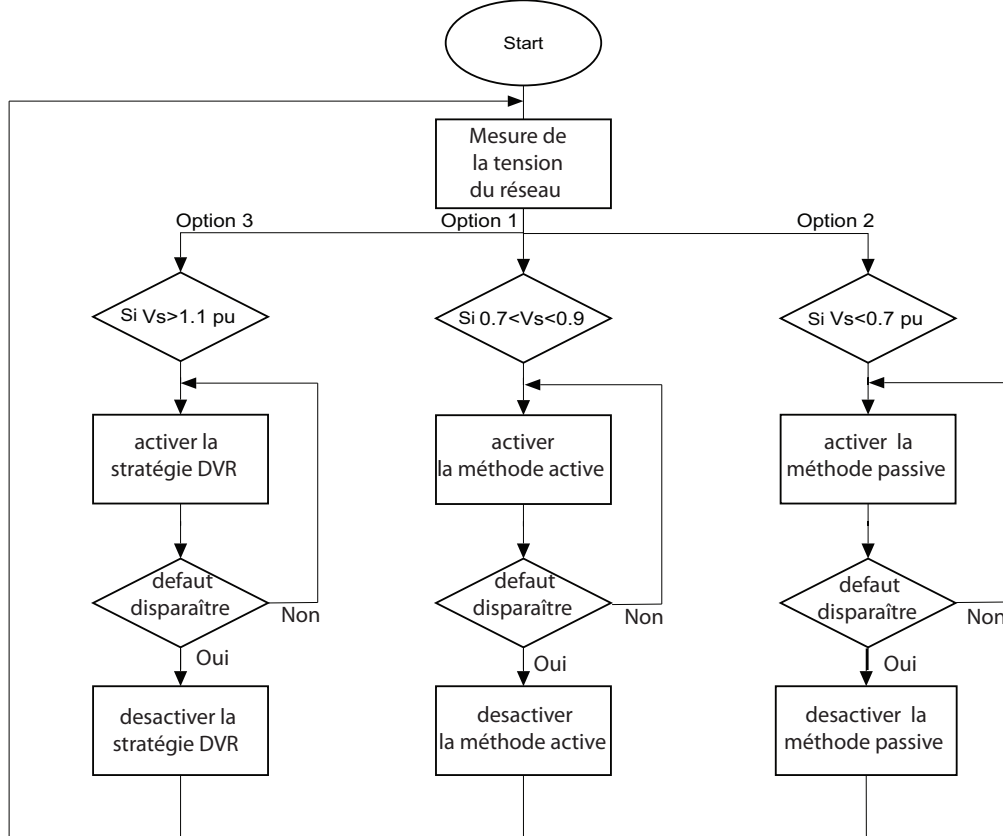


Figure. 1.7. l'organigramme de la stratégie proposée basée sur la combinaison des méthodes HVRT et LVRT.

1.1.4 Conclusion

Les capacités LVRT et HVRT des WT sont nécessaires avec l'intégration croissante de l'énergie éolienne et contribuent à l'intégration régulière au réseau. Cette stratégie a étudié la performance des méthodes passives et actives pour la capacité FRT de la machine. Par conséquent, la stratégie LVRT est basée sur la méthode active qui a utilisé un contrôleur P qui n'est valable que pour les creux de tension faibles inférieurs à 30%, également un SDBR couplé en série avec les enroulements du stator est utilisé pour la méthode passive. Par ailleurs, la stratégie HVRT proposée est basée sur l'ajout d'un DVR, qui assure l'équilibre du réseau en contrôlant la puissance réactive. Les résultats de la simulation ont permis d'indiquer le comportement de la méthode proposée lors de tout défaut de tension. En outre, les résultats de la simulation obtenus à l'aide

d'une machine (DFIG) de 1,5 MW connectée au réseau électrique, rapportent la grande performance des stratégies proposées pour améliorer la capacité FRT de la machine (DFIG).

les résultats sont présentés au chapitre 2.

Ce travail est publié dans deux journal indexé : [3] et [11]

1 - El Makrini, A., El Karkri, Y., Boukhriss, Y., El Markhi, H., & El Moussaoui, H. (2017). LVRT control strategy of DFIG based wind turbines combining passive and active protection. *Int. J. Renew. Energy Res*, 7, 1258-1269.

2 - El Karkri, Y., El Markhi, H., El Moussaoui, H., & Lamhamdi, T. (2018). LVRT and HVRT control strategies of Doubly-Fed Induction Generator. *Journal of Electrical Systems*, 14(4).

1.1.5 Stratégie LVRT utilisant les Régulateurs Proportionnels Résonants pour les défauts de réseau symétriques

Pour la troisième stratégie une nouvelle technique de protection du système éolien et de compensation de la puissance réactive lors de conditions anormales de réseau électrique selon le code de réseau espagnol est proposée. La conception de la commande est mise en œuvre sur les convertisseurs de puissance, et la régulation du courant du réseau est développée en utilisant des régulateurs proportionnels-résonnats dans un cadre de référence stationnaire biphasé ($\alpha - \beta$). Les performances de contrôle sont significativement validées en appliquant la simulation en temps réel pour le convertisseur côté rotor et 'Hardware-in-the-loop simulation' pour la partie expérimental de la commande du convertisseur côté réseau du générateur.

Le deuxième convertisseur de la machine (DFIG) est le convertisseur coté réseau qui contrôle l'équilibre de la puissance entre l'éolienne et le réseau électrique public. Le but du convertisseur coté réseau est de réguler la tension continue afin de générer la référence de puissance active $P_{g,ref}$ en utilisant un régulateur PI et également de réguler la puissance réactive injectée dans le réseau électrique. Ce dernier est obtenu en régulant correctement les composantes négative et positive des courants du réseau afin de faire face aux conditions de perturbation de la tension du réseau et aux oscillations de puissance fournies par le convertisseur coté rotor au circuit intermédiaire. Les composants

négative et positive du réseau électrique défectueux doivent être calculé à partir des tensions triphasées mesurées.

Les régulateurs de courant PR dans le référentiel stationnaire sont appliqués dans cette section. Ce type de régulateurs se compose généralement d'un régulateur P plus un filtre résonant accordé à la fréquence fondamentale afin d'atteindre une erreur d'état zéro lorsque des signaux sinusoïdaux sont contrôlés. Une étude détaillée du régulateur PR a été présentée dans [17] et donc, seule une brève explication est fournie dans cette partie. La fonction de transfert du contrôleur PR est exprimée par la relation suivant:

$$C_{PR}(s) = K_p + \frac{K_i s}{s^2 + 2\omega_c s + \omega_e^2} \quad (1.27)$$

où K_p est la constante proportionnelle, K_i est la constante intégrale du régulateur, ω_c est la pulsation de coupure et ω_e est la pulsation de résonance.

L'expression des références de courant de réseau dans le référentiel stationnaire $i_{g\alpha}^*$ et $i_{g\beta}^*$ sont écrites en fonction des composantes de courant active et réactive $i_{g\alpha,P}^*$ et $i_{g\beta,P}^*$ et $i_{g\alpha,Q}^*$ et $i_{g\beta,Q}^*$, respectivement [18]:

$$\begin{cases} i_{g\alpha}^* = i_{g\alpha,P}^* + i_{g\alpha,Q}^* \\ i_{g\beta}^* = i_{g\beta,P}^* + i_{g\beta,Q}^* \end{cases} \quad (1.28)$$

avec :

$$i_{g\alpha,P}^* = \frac{u_{g\alpha}^+ - u_{g\alpha}^-}{(u_{g\alpha}^{+2} + u_{g\beta}^{+2}) - (u_{g\alpha}^{-2} + u_{g\beta}^{-2})} P_{g,ref} \quad (1.29)$$

$$i_{g\alpha,Q}^* = \frac{u_{g\beta}^+ + u_{g\beta}^-}{(u_{g\alpha}^{+2} + u_{g\beta}^{+2}) - (u_{g\alpha}^{-2} + u_{g\beta}^{-2})} Q_{g,ref} \quad (1.30)$$

$$i_{g\beta,P}^* = \frac{u_{g\beta}^+ - u_{g\beta}^-}{(u_{g\alpha}^{+2} + u_{g\beta}^{+2}) - (u_{g\alpha}^{-2} + u_{g\beta}^{-2})} P_{g,ref} \quad (1.31)$$

$$i_{g\beta,Q}^* = -\frac{u_{g\alpha}^+ + u_{g\alpha}^-}{(u_{g\alpha}^{+2} + u_{g\beta}^{+2}) - (u_{g\alpha}^{-2} + u_{g\beta}^{-2})} Q_{g,ref} \quad (1.32)$$

La figure 1.8 décrit le principe de la commande du convertisseur coté réseau à l'aide des régulateurs PR, tandis que les P-N SC de la tension de réseau sont calculés à partir de la tension de réseau mesurée [19]. Les quatre composants de tension du réseau ($u_{g\alpha}^+$, $u_{g\alpha}^-$, $u_{g\beta}^+$ et $u_{g\beta}^-$) générés par le détecteur des composants P et N avec $P_{g,ref}$ et $Q_{g,ref}$ sont utilisés pour calculer les deux références de courants de réseau dans la référence stationnaire ($i_{g\alpha}^*$ et $i_{g\beta}^*$) avec le module de calcul des références courant. Les deux références de courants $i_{g\alpha}^*$ et $i_{g\beta}^*$ sont comparées aux signaux mesurés, et la différence est fournie aux régulateurs PR. Les sorties de ces régulateurs sont les signaux de tension de l'onduleur dans le cadre de référence stationnaire et ainsi, la transformation de Clarke inverse est appliquée à ces variables afin d'alimenter le bloc de modulation de largeur d'impulsion (PWM). Les sorties du PWM sont les signaux de commutation pour l'onduleur triphasé.

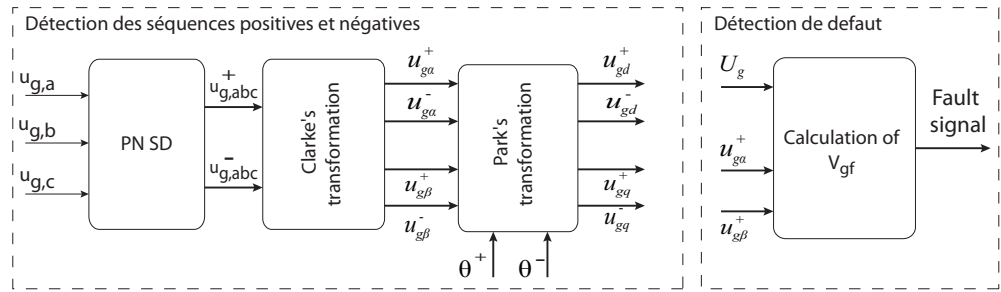


Figure. 1.8. P-N SD block.

1.1.6 Conclusion

Les algorithmes de contrôle proposés dans cet étude sont utilisés pour une machine (DFIG) connecté au réseau afin d'améliorer la qualité de l'énergie et de traiter les exigences LVRT conformément au code de réseau espagnol. La commande vectorielle utilisant la stratégie de commande orientée de flux statorique a été appliquée au convertisseur coté rotor, et les performances de cette commande ont été vérifiées à l'aide de simulations numériques en temps réel. De plus, le convertisseur coté réseau est commandé pour compenser la puissance réactive et réduire les oscillations de la puissance active pendant le fonctionnement déséquilibré du réseau. Pour cette raison, les régulateurs PR ont été proposés dans le référentiel stationnaire afin de contrôler les séquences négative et positive des courants de réseau. Les différents types de creux de tension du réseau ont été testés, et les expériences utilisant la simulation CHIL valident les algorithmes de contrôle proposés pour tous les tests, en limitant l'amplitude des courants du réseau, en

injectant la puissance réactive requise et en stabilisant la puissance active transférée au réseau.

les résultats sont présentés au chapitre 3.

Ce travail est publié dans un journal indexé : [20]

- EL KARKRI, Yassir, REY-BOUÉ, Alexis B., EL MOUSSAOUI, Hassan, et al. Improved Control of Grid-connected DFIG-based Wind Turbine using Proportional-Resonant Regulators during Unbalanced Grid. Energies, 2019, vol. 12, no 21, p. 4041.

1.2 Diagnostic des défauts sur les capteurs du courant

Cette partie présente une nouvelle stratégie de diagnostic de défaut et de commande tolérante aux pannes des capteurs de courant pour une machine asynchrone à double alimentation avec sortie DC basée sur une commande de couple prédictive. Généralement, les défaillances des capteurs de courant peuvent détériorer la fiabilité et les performances du système de commande et peuvent conduire au dysfonctionnement de la stratégie de commande prédictive car le flux rotor et stator ne peut pas être estimé correctement. Le diagnostic de défaut proposé peut traiter tous les types de défauts de capteur. De plus, un observateur non linéaire est adapté au système étudié afin d'assurer la continuité du bon fonctionnement lorsque deux ou tous les capteurs de courant sont défectueux. Une machine asynchrone à double alimentation de 4 kW avec système de sortie DC est mis en place pour l'expérience, la faisabilité et la robustesse de l'approche proposée sont obtenues en testant différents types de défauts de capteur sur le courant du stator et du rotor et dans différents cas du mode de fonctionnement.

1.2.1 Tolérance de défaut durant un capteur défectueux

Dans le schéma principal du système de contrôle, un nouveau bloc lié au diagnostic de défaut du capteur est ajouté. On suppose que le système fonctionne avec trois capteurs de courant dans les parties du stator et du rotor. Le défaut de courant du capteur peut être détecté à l'aide de l'équation d'équilibrage à 3 phases:

$$|i_a + i_b + i_c| > \xi \quad (1.33)$$

i_a , i_b et i_c sont le courant triphasé et ξ est la valeur seuil entre un fonctionnement normal et un fonctionnement défectueux.

Ces informations peuvent prouver l'apparition du défaut sans identifier la phase exacte où le défaut du capteur apparaît. Par conséquent, dans cette partie, un nouveau algorithme de diagnostic des défauts est proposé pour garantir la détection rapide et exacte du capteur défaillant. La méthode est simple à mettre en œuvre et repose sur le calcul de la différence entre la valeur actuelle et la valeur précédente du courant normalisé dans chaque phase:

$$\left\{ \begin{array}{l} \delta_a = \frac{1}{\sqrt{2}I_m} |i_a(k) - i_a(k-1)| \\ \delta_b = \frac{1}{\sqrt{2}I_m} |i_b(k) - i_b(k-1)| \\ \delta_c = \frac{1}{\sqrt{2}I_m} |i_c(k) - i_c(k-1)| \end{array} \right. \quad (1.34)$$

Lorsque le défaut du capteur se produit, il est facile de détecter le changement sur chaque phase en fonction des informations provenant des variables de diagnostic δ_a , δ_b et δ_c . Un changement anormal dans chaque phase peut être détecté en comparant chaque variable de diagnostic par rapport à un seuil qui dépend de la valeur du courant nominal: si la variable de diagnostic est inférieure au seuil choisi, alors aucun défaut n'est détecté et l'indice de défaut est toujours égal à zéro, sinon si l'une des variables de diagnostic devient supérieure au seuil choisi, l'indice de défaut passe à 1:

$$\left\{ \begin{array}{l} \text{if } (\delta_{(a,b,c)} \leq Thr) \text{ then } F_{a,b,c} = 0; \\ \text{elseif } (\delta_{(a,b,c)} > Thr) \text{ then } F_{a,b,c} = 1; \end{array} \right. \quad (1.35)$$

où Thr est le seuil choisi et F_i est l'indice de défaut. Dans cette étude, $Thr = 2/\sqrt{2}I_m$. L'algorithme de diagnostic de défaut proposé est valable pour tous les types de défaut de capteur à l'exception des valeurs inférieures pour "erreur de gain" lorsque le générateur fonctionne sur des valeurs de couple inférieures. En effet, pour assurer un fonctionnement sûr dans cette situation, le même algorithme est utilisé considérant une seule configuration des variables de diagnostic au lieu d'utiliser la valeur actuelle et précédente de chaque phase, le taux moyen de la différence entre le mesuré et le courant observé est appliqué:

$$\begin{cases} \Delta_a = \text{mean}(|i_a - \bar{i}_a|) \\ \Delta_b = \text{mean}(|i_b - \bar{i}_b|) \\ \Delta_c = \text{mean}(|i_c - \bar{i}_c|) \end{cases} \quad (1.36)$$

Dans le cas où un seul défaut de capteur est détecté et bien localisé, le bloc de reconfiguration de défaut reçoit les signaux d'index de défaut du bloc de diagnostic pour compenser le capteur de courant défectueux à l'aide des deux autres capteurs sains (loi de Kirchhoff) afin de générer les courants appliqués au système de contrôle DFIG-DC. Un principe de reconfiguration de défaut de capteur est représenté sur la figure 1.9

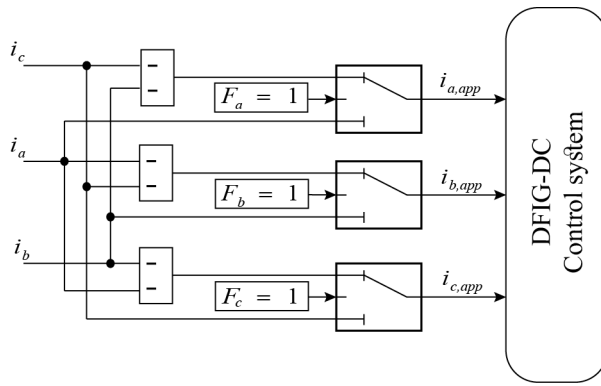


Figure. 1.9. One sensor Fault reconfiguration block.

1.2.2 Tolérance de défaut avec deux capteurs défectueux

lorsque deux capteurs sont défectueux en même temps, un observateur non linéaire est utilisé pour le rotor et les courants du stator, et les signaux d'indice de défaut générés par l'algorithme de diagnostic proposé sont utilisés pour passer des signaux de courant défectueux au courant observé.

Le modèle d'états de l'observateur utilisé peut être présenté comme suit:

$$\begin{cases} \dot{x} = A_x x + B_x u + G y \\ \dot{y} = A_y x + B_y u + H y \end{cases} \quad (1.37)$$

où x et y sont respectivement les variables mesurées et estimées, u est le vecteur de contrôle. Les matrices A_x , B_x , A_y , B_y et H sont définies pour chaque observateur. En appliquant l'observateur proposé dans [14] sur notre système, x et y sont remplacés par

le courant du stator et du rotor en fonction de l'observateur utilisé. Les observateurs utilisés sont présentés comme:

- l'observateur du courant rotorique

$$\begin{cases} \dot{\hat{i}}_s = A_s i_s + B_m u_r + B_s u_s + G_r \hat{i}_r + K_r \xi_s \\ \dot{\hat{i}}_r = A_{rs} i_s + B_r u_r + B_m u_s + H_r \hat{i}_r + N_r \xi_s \end{cases} \quad (1.38)$$

- l'observateur du courant statorique

$$\begin{cases} \dot{\hat{i}}_r = A_r i_r + B_r u_r + B_m u_s + G_s \hat{i}_s + K_s \xi_r \\ \dot{\hat{i}}_s = A_{sr} i_r + B_m u_r + B_s u_s + H_s \hat{i}_s + N_s \xi_r \end{cases} \quad (1.39)$$

Avec : $i_s = \begin{bmatrix} i_{ds} \\ i_{qs} \end{bmatrix}$ et $i_r = \begin{bmatrix} i_{\alpha r} \\ i_{\beta r} \end{bmatrix}$ sont les variables d'état,

$u_s = \begin{bmatrix} u_{ds} \\ u_{qs} \end{bmatrix}$ et $u_r = \begin{bmatrix} u_{\alpha r} \\ u_{\beta r} \end{bmatrix}$ sont les variables de contrôle,

$\xi_s = i_s - \hat{i}_s$ et $\xi_r = i_r - \hat{i}_r$ sont respectivement les erreurs entre les courants mesurés et estimés du stator et du rotor.

Afin d'assurer les conditions de convergence et la stabilité du système [14], N_r et N_s sont choisis égaux à la matrice de transposition de G_r et G_s respectivement, et K doit être défini positive:

$$\begin{cases} N_r = G_r^T \\ N_s = G_s^T \\ K > 0 \end{cases} \quad (1.40)$$

Lorsque le défaut du capteur apparaît en deux phases, un signal d'index à 2 défauts (2F) est généré par le bloc de diagnostic de défaut à deux capteurs et utilisé pour commuter le courant appliqué au système de commande de mesuré à observé. Le principe de reconfiguration des défauts de deux capteurs est représenté sur la figure 1.10.

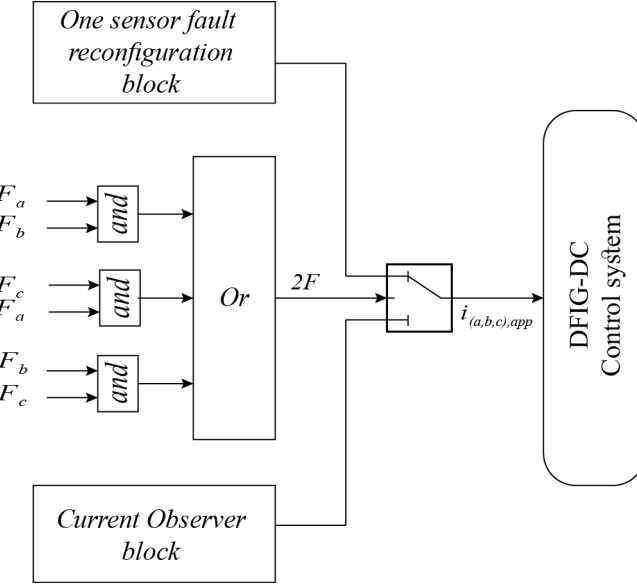


Figure. 1.10. Principe de reconfiguration avec deux capteurs défectueux.

1.2.2.1 Conclusion

Ce travail présente un diagnostic robuste et rapide et un algorithme tolérant aux pannes pour DFIG-DC. La commande de couple prédictive est appliquée au système de control. Le diagnostic de défaut a été proposé pour pouvoir détecter rapidement tous les types de défauts de capteurs, l'algorithme proposé est basé uniquement sur le courant mesuré, à une exception près lorsqu'un défaut d'erreur de gain plus faible apparaît, le courant observé est utilisé avec le courant mesuré dans l'ordre pour assurer le fonctionnement normal et sûr du système. En outre, la stratégie de tolérance aux pannes est conçue sur la base de l'indice de panne généré par l'algorithme de diagnostic; lorsqu'un seul capteur est défectueux, les capteurs sains sont utilisés pour récupérer le capteur défectueux, et lorsque plus d'un capteur est défectueux, les courants observés sont utilisés pour remplacer les signaux défectueux provenant de la mesure. De plus, la robustesse de l'algorithme proposé a été expérimentée par différents tests, qui confirment que le schéma proposé est indépendant des paramètres DFIG et du mode de fonctionnement, et que tous les défauts de capteur mentionnés peuvent être identifiés et tolérés avec précision.

les résultats sont présentés au chapitre 4.

1.3 Évaluation du crédit de capacité d'énergie éolienne: étude de cas du site nord-ouest du Maroc.

Dans cette partie, nous sommes intéressés à l'étude de l'impact de la production intermittente dans le long terme. Jusqu'à quel niveau, en terme de capacité et flexibilité, l'éolien peut-il remplacer les centrales actuelles conventionnelles ? Pour répondre à cette question, nous avons utilisé le concept de Crédit de Capacité de l'Eolien (CCE) qui peut être défini comme la part de la capacité éolienne installée et substituée à des moyens de production classique sans mettre en danger la sûreté de fonctionnement du réseau.

1.3.1 L'analyse du crédit de capacité

Dans notre étude, afin de déterminer le CCE, nous allons modéliser de façon probabiliste le système électrique. Le modèle probabiliste d'un système électrique doit permettre de décrire le comportement des variables incertaines du système et les corrélations entre ces incertitudes figure 1.11. Il ne s'agit pas simplement de modéliser le système par un jeu de paramètres d'entrées fixes, mais de caractériser, de quantifier l'incertitude liée à ces paramètres. Ainsi dans le modèle probabiliste du système électrique tel que nous le définissons, le jeu de paramètres d'entrée laisse place à un jeu de lois de probabilités, chacune caractérisant la variation d'un paramètre.

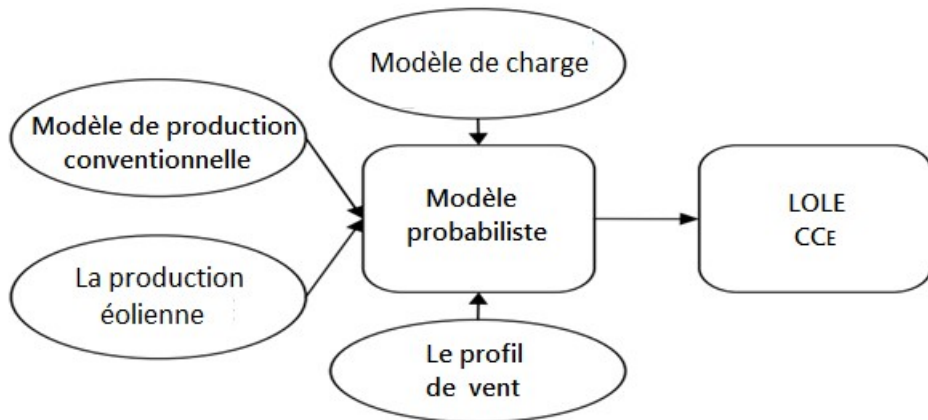


Figure. 1.11. Modèle probabiliste pour l'analyse du CCE.

L'algorithme de détermination CC du vent proposé est présenté sur la figure 1.12, reçoit en entrée les caractéristiques du système électrique:

Cet algorithme recevra en entrées les caractéristiques du système électrique à savoir :

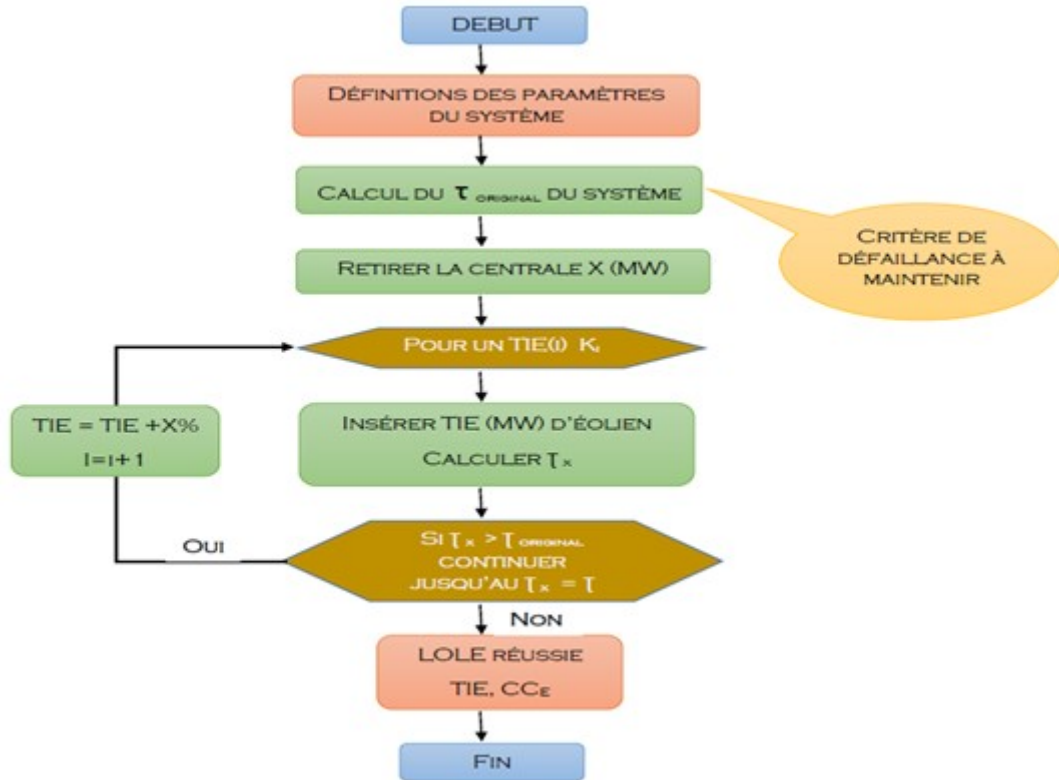


Figure. 1.12. Algorithme de détermination du CCE.

- Les unités de production conventionnelle et leurs taux de défaillance.
- Les données de consommation du système.
- Le profil de vent du site sur lequel seront installées les éoliennes.
- La courbe de puissance des éoliennes qui seront installées

Le CCE sera déterminé après une étude comparative de la fiabilité du système sans et avec la présence de la production d'énergie renouvelable. L'analyse du CCE est faite selon le critère de remplacement de la production thermique, ceci signifie qu'une unité A de capacité X MW sera retirée du système. L'objectif est d'estimer la capacité minimale d'éoliennes qui doit être installée en gardant le même niveau de fiabilité du système. L'explication sous forme paramétrique est la suivante : lorsqu'une capacité X MW est retirée du système, le taux de sûreté τ original "Loss of Load Expectation (LOLE)" est affecté. Le nouveau taux de sûreté τ_x permettra de satisfaire les exigences du système et de couvrir la demande. Nous cherchons donc, la capacité K_n qui peut être installée pour atteindre τ original.

Table. 1.2. Puissance installée sur le réseau électrique national ([21]).

Centrales	Puissance installée en MW	Forced Outage Rate
usines hydrauliques	1306	0,01
STEP	464	0,01
<i>Coal (y compris JLEC)</i>	4146	0,04
<i>fuel oil</i>	600	0,05
<i>Gas-turbine</i>	1230	0,02
<i>Combined cycle</i>	850	0,04
nuclear	2480	0,12
Total réseau national	11278	

En conséquence, le crédit de capacité peut donc, être calculé par l'expression suivante :

$$CC = X/K_n \times 100\% \quad (1.41)$$

1.3.1.1 Modèle de production conventionnelle

A la fin de 2016, le parc de production national du Maroc, avec une puissance installée de 11278 MW, est composé de centrales thermiques, hydrauliques, des interconnexions et aussi des productions locales de certains concessionnaires. Les détails du parc et les taux de défaillance sont donnés dans le tableau 1.2 :

la puissance installée s'est élevée à 12813 MW à la fin décembre 2017 et à 12983 à la fin de décembre 2018 contre 11278 MW en 2016, soit une augmentation de 15,11% due à la mise en service des 2 groupes charbon de Safi (2 x 660 MW), un groupe charbon de Jerada (350 MW) suivie du déclassement des groupes actuels de cette centrale (- 135 MW) en 2017, ainsi que la mise en service des centrales hydrauliques M'dez et El Menzel (170 MW) en 2018.

1.3.1.2 Modèle de charge

Le modèle de charge s'acquiert avec la construction de la monotone de consommation pour une période donnée correspondant à une année (8760 h ou 365 jours)(figure 1.13). Pour construire la monotone de consommation ou modèle cumulatif de charge, il faut disposer de l'information de consommation horaire ou journalière du système qu'il va falloir classer par ordre décroissant ensuite nous pourrons calculer le poids de chaque état de consommation. Cet arrangement nous permettra d'avoir la valeur.

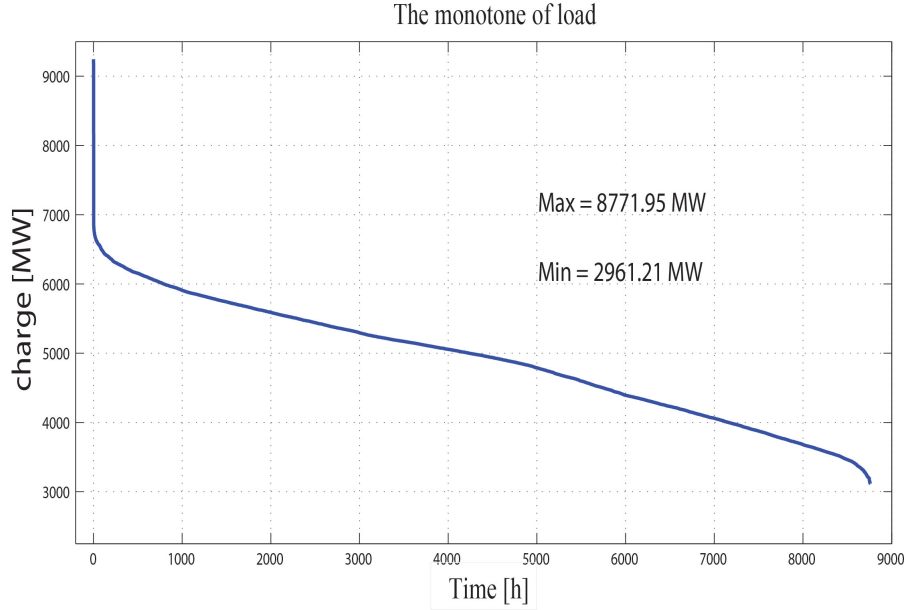


Figure. 1.13. le monotone de charge 2020.

A moyen terme, les prévisions de la demande traduisent principalement l’expression des besoins des clients industriels de l’ONE et des sociétés privées de distribution d’électricité des principales villes du pays. Ces prévisions portent également sur l’évaluation du marché de la Distribution ONE correspondant essentiellement aux zones rurales. Ainsi, le taux d’accroissement prévu pour 2010–2013, est de 6% environ. Pour le long terme, l’évolution de la consommation d’électricité résulte de la conjugaison de facteurs de natures très diverses : l’activité économique, la démographie, le comportement des utilisateurs, le progrès technique, le développement de nouveaux usages de l’électricité, les parts de marché entre énergies, les actions de maîtrise de l’énergie, etc.

Le scénario de base retenu s’appuyant principalement sur les réformes économiques, est axé sur une évolution du PIB de l’ordre de 5,82%, sur la période 2015-2020 [22]. Ce scénario dit de l’émergence, retenu comme scénario de référence pour l’élaboration du plan d’équipement de l’ONÉE, se traduit par une croissance de 6% à long terme.

1.3.1.3 Modèle probabiliste (Modèle de risque)

Une fois les modèles de production et de charge établis, une convolution de ces deux modèles est nécessaire pour l’établissement du modèle de risque qui permet de quantifier le risque du système. Cette méthode permet de déterminer les indices de sûreté de fonctionnement, c’est-à-dire le risque de perte de charge ”Loss Of Load” précédemment

cité. Nous travaillerons avec l'indice LOLE "Loss Of Load Expectation" qui est l'espérance mathématique du nombre d'heures de défaillance, c'est-à-dire, le nombre d'heures par an durant lesquelles la ressource de production disponible n'est pas suffisante pour couvrir l'ensemble de la demande.

Cet indice peut être représenté de la façon suivante :

$$LOLE = \sum_{i=1}^n P_i(C_i - L_i) \quad (1.42)$$

Avec :

- C_i = capacité disponible pour le jour/heure i
- L_i = Prévision de la consommation pour le jour/heure i
- $P_i(C_i - L_i)$ = Probabilité de la perte de charge "loss of load"e pour le jour i.

L'algorithme proposé a été programmé sous le logiciel MATLAB, afin de déterminer le niveau de fiabilité du parc national via l'indice LOLE, vu que ce dernier est l'indice le plus utilisé pour la détermination des capacités de production requises dans l'horizon du moyen et long terme. Cela permet d'évaluer le niveau de risque du système, en calculant l'indice de fiabilité LOLE, tel que présenté dans cette chapitre.

Le tableau suivant fait mention du résultat obtenu après simulation du programme.

Table. 1.3. MNG reliability level.

System	LOLE (simulated)
MNG	0.0413 (h/year)

1.3.1.4 Conclusion

La présente étude se concentre sur le calcul du crédit de capacité éolienne en intégrant le projet marocain de l'énergie éolienne (1000 MW en 2020). Après une introduction au Projet Éolien Intégré Marocain, un programme d'évaluation de crédit de capacité éolienne est mis en œuvre sur le logiciel Matlab comprenant l'ensemble des informations sur "la capacité installée, le nombre des centres, le taux de panne, les types d'unités

installées, la demande de pointe, etc.” Ce programme servira à calculer le taux de sécurité d'un système électrique ainsi que le crédit de capacité du réseau de production électrique du Maroc. Cette étude se construit en deux phases: la première phase examine l'impact du parc éolien TAZA d'une puissance installée de 150 MW, tandis que la seconde phase se concentre sur la généralisation de cette étude sur l'ensemble des parcs éoliens qui seront injectés sur le réseau marocain en 2020. Les résultats de l'étude aboutit à des conclusions en fonction de l'évaluation de l'impact de cette intégration d'énergie électrique basée sur la production éolienne.

les résultats sont présentés au chapitre 5.

Ce travail est publié dans un journal indexé : [23]

- EL KARKRI, Yassir, EL MAKRINI, Aboubakr, EL MARKHI, Hassane, et al. Assessment of wind power capacity credit in Morocco: Outlook to 2020. Wind Engineering, 2020, vol. 44, no 2, p. 196-207.

1.4 Conclusion général

Cette thèse présente trois thèmes pour améliorer l'intégration des éoliennes DFIG connectées au réseau. La première contribution porte sur les capacités LVRT et HVRT des éoliennes. Deux approches sont proposées dans ce contexte. Le premier a étudié les performances des méthodes passives et actives pour la capacité *FRT* du DFIG. Cependant, la stratégie LVRT est basée principalement sur la méthode active, qui utilisait un contrôleur P pour contrôler le flux du rotor, cette méthode n'est valable que pour les creux de basse tension inférieurs à 30 %; et pour les défauts de réseau plus profonds, un SDBR couplé en série avec les enroulements de stator utilisés pour la méthode passive. Par ailleurs, la stratégie HVRT proposée est basée sur l'ajout d'un *DVR*, qui assure l'équilibre de la tension du réseau en contrôlant la puissance réactive. Les résultats de la simulation ont permis d'indiquer le comportement de la méthode proposée lors de tout défaut de tension. De plus, les résultats de simulation obtenus à l'aide d'un DFIG de 1,5 MW connecté au réseau électrique présentent d'excellente performance des stratégies proposées pour améliorer la capacité FRT du DFIG (les résultats sont présentés au chapitre 2). La deuxième contribution de cette partie introduit un algorithme de contrôle pour améliorer la qualité de l'énergie face aux exigences LVRT selon

le code de réseau espagnol. La commande vectorielle utilisant la stratégie de commande orientée du flux statorique a été appliquée au RSC, et les performances de cette commande ont été vérifiées à l'aide du DRTS. De plus, le GSC est commandé pour compenser la puissance réactive et réduire les oscillations de puissance active pendant le fonctionnement déséquilibré du réseau. Pour cette raison, les régulateurs *PR* ont été proposés dans le référentiel stationnaire pour contrôler les séquences négatives et positives des courants de réseau. Les différents types de creux de tension du réseau ont été testés. Les expériences utilisant la simulation CHIL valident les algorithmes de contrôle proposés pour tous les tests en limitant l'amplitude des courants du réseau, en injectant la puissance réactive requise et en stabilisant la puissance active transférée dans le réseau (les résultats sont présentés au chapitre 3).

La deuxième partie de cette thèse présente un diagnostic robuste et rapide, ainsi qu'un algorithme tolérant aux pannes pour les variateurs DFIG-DC. La commande de couple prédictive est appliquée au système de commande. Le diagnostic de défaut a été proposé pour pouvoir détecter rapidement tous types de défauts de capteurs; l'algorithme proposé est basé uniquement sur le courant mesuré, à une exception près lorsqu'un défaut d'erreur de gain inférieur apparaît, le courant observé est utilisé avec le courant mesuré afin d'assurer le fonctionnement sûr et normal du système. En outre, la stratégie de tolérance aux pannes est conçue sur la base de l'indice de panne généré par l'algorithme de diagnostic. Lorsqu'un seul capteur est défectueux, les capteurs sains sont utilisés pour récupérer le capteur défectueux, et une fois plus d'un capteur est défectueux, les courants observés sont utilisés pour remplacer les signaux défectueux provenant de la mesure. De plus, la robustesse de l'algorithme proposé a été expérimentée par différents tests, qui confirment que le schéma proposé est indépendant des paramètres DFIG et du mode de fonctionnement, ainsi que tous les défauts de capteur mentionnés peuvent être identifiés et tolérés avec précision (les résultats sont présentés au chapitre 4).

La dernière partie de cette thèse considère l'intégration à long terme des éoliennes dans le réseau électrique marocain. L'étude de fiabilité réalisée dans cette partie a démontré que l'énergie éolienne peut contribuer à la sécurité du système et remplacer une partie de la capacité conventionnelle installée mesurée par le CC. Le CC est estimé

dans cet étude en se basant sur la probabilité de fiabilité du réseau national, qui se complique lorsque la dimension du système est importante. Pour cette raison, nous nous sommes appuyés sur la littérature existante a propos de la fiabilité et la sécurité de fonctionnement, ainsi que l'amélioration des modèles existants via l'introduction de différents critères paramétriques. On a également observé que le CC est réduit linéairement en fonction du taux d'injection de l'éolienne, celui-ci est effectivement dépendant des centrales conventionnelles considérées. Par conséquent, dans le cadre de l'intégration massive de l'énergie éolienne, une production conventionnelle devra être mise en place pour atténuer la détérioration des CC et préserver la fiabilité du système (les résultats sont présentés au chapitre 5).

Chapter 2

LVRT and HVRT control strategies of Doubly-Fed Induction Generator

2.1 introduction

In this first contribution, we propose a control strategy to develop the LVRT and HVRT capability of the DFIG during symmetrical grid voltage faults. The proposed strategy for LVRT combines the active method to limit fault in current at low voltage sags and the passive method for severe voltage sags by adding hardware protections like SBR. The proposed solution for HVRT capability involves the use of DVR to maintain DFIG terminal voltage stable and to provide maximum support to help the grid voltage fast recovery by controlling power converters.

Diverse studies discussed in the literature have addressed the LVRT and HVRT capability for DFIGs. These strategies can be classified into two principal categories:

- Active methods: using appropriate converter control.
- Passive methods: using an additional electronic equipment.

The conventional solution for FRT requirements is the use of the crowbar circuit [24]. Despite the fact that the crowbar circuit protection is a cost-effective strategy, capable

to secure the power converters of DFIG, its disadvantage is that the DFIG misses its controllability once the crowbar circuit is activated, due to the Rotor Side Converter (RSC) deactivating. In such condition, DFIG consumes reactive power from the grid because of grid voltage degradation. In the same context, a Stator Damping Resistor (SDR) composed of three resistors and three bypassing bidirectional switches coupled in series with the stator circuit is proposed in [25]. In normal states, these switches rest closed and the stator current will not circulate within the resistors. The new LVRT methods seem to be more effective than those using conventional crowbar circuit. In addition, using these approaches, it seems possible to enhance DFIG FRT capability as the main disadvantage of the crowbar is missing the DFIG control over grid faults [26]. Also, an Energy Storage System (ESS) proposed in [27] can help to stabilize the DC-voltage and mitigate the output power simultaneously, but it is very difficult to diminish the electromagnetic torque oscillations and rotor overcurrent. On the other hand, for passive methods, it has also been proposed combination of control strategies and the addition of electronic components [28]. A transient current control scheme is proposed for the RSC with crowbar protection in [29]. A different solution is proposed on [30] by utilizing a Parallel Grid Side Rectifier (PGSR) with a Series Grid Side Converter (SGSC). This converters combination allows unrestricted power processing and robust control of voltage changes.

Some researchers add an external power electronic device called a Dynamic Voltage Restorer (DVR), which is an electrical voltage converter connected to the grid in order to compensate voltage variation. Different DVR Shapes are proposed to protect the DFIG WT in [31], but the control of reactive power during grid faults is not considered. In [32] the authors proposed strategies to compensate the voltage swells using Static Synchronous Compensator (STATCOM) and DVR devices. However, these strategies need additional electrical devices which augment the system complexity.

2.2 DFIG behaviour during grid faults

Without any protection system, the grid system disturbances can lead to large fault currents in the stator windings. Because of the magnetic coupling between the stator windings and the rotor windings, each distress in the stator part is transmitted directly to the rotor circuit. However, the dimensioning of the power converter is relatively

small compared to the system, so it would not be possible to keep the controllability of the system for high rotor current. This means that the converter reaches quickly its limits, therefore, it loses the control of the generator during the grid fault. Also, in this conditions the Grid Side Converter (GSC) cannot transfer the power to the grid and therefore the extra energy charges the capacitor, then the DC-link voltage can increase rapidly and destroy the link capacitor.

To see the DFIG behaviour, the evolution of its magnitudes during the grid faults, and to be able to determine the causes and subsequently to propose solutions, we made a study on DFIG's dynamic response during the grid disturbances.

Stator and rotor voltage equations are expressed in a reference related to the stator and rotor respectively as:

$$\vec{v}_s^s = R_s \vec{i}_s^s + \frac{d\vec{\phi}_s^s}{dt} \quad (2.1)$$

$$\vec{v}_r^r = R_r \vec{i}_r^r + \frac{d\vec{\phi}_r^r}{dt} \quad (2.2)$$

Where v_s^s and v_r^r are the stator and rotor voltage, i_s^s and i_r^r are the stator and rotor current, R_s and R_r are the stator and rotor resistances and ϕ_s^s and ϕ_r^r are the stator and rotor flux linkages. The subscripts s and r indicate stator and rotor quantities, while the superscripts denote the use of stator and rotor reference frame. [33].

The stator and rotor flux linkages are expressed as:

$$\phi_s = L_s i_s + M i_r \quad (2.3)$$

$$\phi_r = L_r i_r + M i_s \quad (2.4)$$

Where L_s , L_r , L_m are the stator inductance, rotor inductance and mutual inductance, respectively. With equation (2.3) and equation (2.4), the rotor flux linkage is expressed as:

$$\phi_r = \frac{M}{L_s} \phi_s + \sigma L_r i_r \quad (2.5)$$

Where σ is the linkage coefficient $\sigma = 1 - \frac{M^2}{L_s L_r}$. Substituting equation (2.5) into the rotor voltage equation (2.2), the rotor voltage can be further expressed as:

$$\vec{v}_r^r = \vec{e}_r^r + (R_r + \sigma L_r \frac{d}{dt}) \vec{i}_r^r \quad (2.6)$$

$$\vec{e}_r^r = \frac{M}{L_s} \frac{d\vec{\phi}_s^r}{dt} \quad (2.7)$$

It can be seen that the rotor voltage can be decomposed into two items. The first item is the (EMF) induced by the stator flux linkage and defined as e_r^r , and then the second item which is the voltage drop caused by the rotor current in both the rotor resistance R_r and the rotor transient inductance L_r .

When a symmetrical fault occur at $t = t_0$, the stator voltage changes from V_1 to V_2 :

$$\vec{v}_s = \begin{cases} V_1 e^{j\omega_s t} & t < t_0 \\ V_2 e^{j\omega_s t} & t > t_0 \end{cases} \quad (2.8)$$

where V_1 and V_2 are respectively the stator voltages before and after the grid fault and ω_s is the synchronous speed. Neglecting R_s , the evolution of the stator flux linkage during the voltage dips obtained from equation (2.1) and equation (2.8) is:

$$\vec{\phi}_s = \begin{cases} \frac{V_1}{j\omega_s} e^{j\omega_s t} & t < t_0 \\ \frac{V_2}{j\omega_s} e^{j\omega_s t} & t > t_0 \end{cases} \quad (2.9)$$

Due to the fact that the flux is a state variable, it cannot undergo discontinuities. Thus, the flux cannot change instantaneously from the first value to the second one as calculated in equation (2.9). Instead, the flux changes progressively. As a first step, the situation in which the rotor is in an open circuit condition is analysed.

Using equations (2.5) and (2.1), the stator voltage becomes:

$$\vec{v}_s^s = \frac{R_s}{L_s} \vec{\phi}_s + \frac{d\vec{\phi}_s}{dt} \quad (2.10)$$

The expression of stator flux is calculated by solving the previous differential equation:

$$\vec{\phi}_s = \frac{V_2}{j\omega_s} e^{j\omega_s t} + \frac{V_2 - V_1}{j\omega_s} e^{-t/\tau_s} \quad (2.11)$$

Where τ_s is the time constant of the stator flux linkage. The first part of equation is the positive sequence component of the stator flux linkage, and the second item is the DC component, which decays with the time constant. Then according to equation (2.7), the EMF under symmetrical faults is by:

$$\vec{e}_r^f = \frac{M}{L_s} V_2 s e^{j\omega_s r t} - \frac{M}{L_s} (V_1 - V_2)(1-s) e^{-t/\tau_s} e^{-j\omega_r t} \quad (2.12)$$

Where s is the slip, the first item induces the positive stator flux linkage, and the second item represents the DC component of the stator flux linkage. It is observed straightforwardly from equation (2.12), that the initial amplitude of the EMF induced by the DC component is relatively large. Under a full voltage dip with $s = -0.2$, the initial amplitude of the EMF is much greater than the amplitude under normal condition which would be harmful to the DFIG converters.

2.3 LVRT and HVRT Control Strategies

The control strategies applied during grid faults can be divided into two main categories: LVRT control strategy for voltage sags and HVRT control strategy for voltage swells.

2.3.1 LVRT control strategy

Two control methods are applied for LVRT wind power capacity, depending on the voltage dips level. The first method (active method) is based on the flux control in order to limit rotor overcurrent, this method is valid only for small depths of voltage dips. While the second method (passive method) requires material protections such as the series resistors to minimize significant voltage dips effects.

2.3.1.1 Active method

The active method based on flux linkage tracking is designed for RSC to reduce the rotor over-current during grid faults. According to equations (2.3) and (2.4), the rotor current can be expressed as:

$$i_r = \frac{1}{L_s L_r - M^2} (-M\phi_s + L_s \phi_r) \quad (2.13)$$

Note that $\frac{M}{L_s} \simeq 1$ implying:

$$i_r = \frac{1}{L_s L_r - M^2} (\phi_r - \phi_s) \quad (2.14)$$

The equation (2.14) shows that the rotor current is determined by the difference between stator and rotor flux linkages. When grid faults happen, the DC and negative sequence components will appear in the stator flux linkage. In this case, without a control, the rotor flux linkage cannot follow the stator flux linkage properly and the difference between ϕ_r and ϕ_s tends to be large, which will finally cause over-current in rotor circuit. Therefore, in order to reduce it during grid faults, the rotor flux linkage should be controlled to track the stator flux linkage. Figure 2.1.a and figure 2.1.b show the difference between the stator and rotor fluxes for 30% of voltage dip at $t = 0.6s$ with and without control.

Figure 2.2 shows the control block diagram, which consists of three parts.

a) Flux linkage detection block

The flux linkage detection block is used to calculate the stator and rotor flux linkages depending on measured stator and rotor currents. In the synchronous $dq-axis$, the stator and rotor flux linkages are expressed as the equation (2.15).

$$\begin{cases} \phi_{sd} = L_S I_{sd} + M I_{dr} \\ \phi_{sq} = L_S I_{sq} + M I_{qr} \\ \phi_{rd} = L_r I_{rd} + M I_{ds} \\ \phi_{rq} = L_r I_{rq} + M I_{qs} \end{cases} \quad (2.15)$$

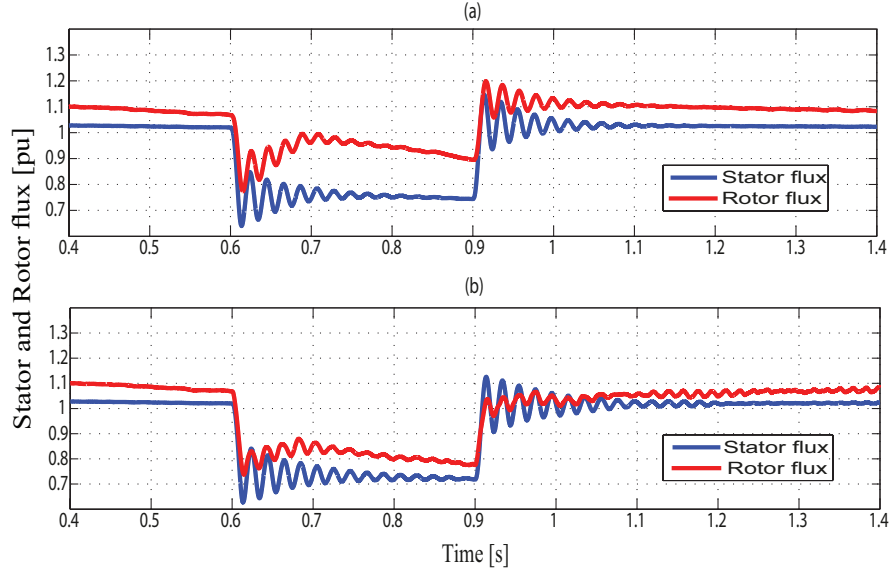


Figure. 2.1. The difference between the stator and rotor fluxes for 30% of voltage dip at $t = 0.6\text{s}$ (a) without control and (b) with control.

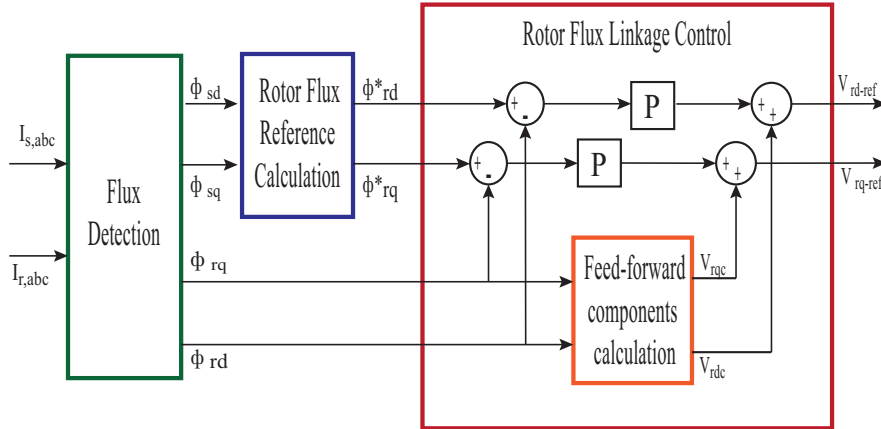


Figure. 2.2. The control block diagram.

b) Rotor flux linkage reference calculation block

The role of the rotor flux linkage reference calculation block is to calculate dq -axis rotor flux linkage references. The rotor flux linkage is based on the stator flux linkage. Then the rotor flux linkage reference ϕ_r^* can be calculated.

$$\phi_r^* = k_T \phi_s \quad (2.16)$$

Where $0 < k_T < 1$ is the tracking gain.

During symmetrical faults, the stator flux linkage has contained DC and negative terms as shown in the equation (2.11). Then, by substituting equation (2.16) into equation (2.14), the rotor current can be expressed by the equation (2.17).

$$i_r \simeq \frac{(k_T - 1)}{L_{ls} + L_{lr}} \phi_s \quad (2.17)$$

From equations (2.16) and (2.17), the rotor current can be reduced to be smaller with a larger k_T . The minimum value of k_T can be calculated as follows; When a grid voltage dip appears, the stator flux linkage will decrease. In other words, the initial stator flux linkage has the largest value during the voltage dips, and its amplitude can be approximately given by $\phi_s(0) \simeq \frac{V_s}{\omega_s}$ according to equation (2.9). If the rotor current is within the maximum current allowed when the stator flux linkage has the largest value, the rotor current during the whole voltage dip period will not exceed the maximum current allowed. So the tracking gain k_T should satisfy that:

$$\frac{(k_{T_{min}} - 1)}{L_{ls} + L_{lr}} \phi_s(0) \leq I_{r_{max}} \quad (2.18)$$

Where $I_{r_{min}}$ is the maximum rotor current. Then the minimal value of k_T can be expressed as:

$$k_{T_{min}} \simeq 1 - \frac{I_{r_{min}} \omega_s (L_{ls} + L_{lr})}{V_s} \quad (2.19)$$

c) Rotor flux linkage control block

A proportional regulator is used, so that the rotor flux follows the reference. basing on (2.3), (2.4) and (2.14) the expression of the rotor voltage can be written as:

$$\begin{cases} V_{rd} = \frac{R_r L_s}{L_s L_r - L_s^2} \Phi_{rd} - \frac{R_r M}{L_s L_r - L_s^2} \Phi_{sd} - \omega_{sr} \Phi_{rq} + \frac{d\Phi_{rd}}{dt} \\ V_{rq} = \frac{R_r L_s}{L_s L_r - L_s^2} \Phi_{rq} - \frac{R_r M}{L_s L_r - L_s^2} \Phi_{sq} - \omega_{sr} \Phi_{rd} + \frac{d\Phi_{rq}}{dt} \end{cases} \quad (2.20)$$

The proportional (P) controller generates signal from the differences between $dq-axis$ rotor flux linkages references (the rotor flux linkage reference calculation block output) and $dq-axis$ rotor flux linkages (the flux linkage detection block output). Then The $dq-axis$ rotor voltages references are obtained by subtracting the control loop output and $dq-axis$ rotor feed-forward voltages (Equations (2.21)and (2.22)). In the feed-forward components calculation, $dq-axis$ rotor voltages are calculated according to $dq-axis$ rotor flux linkages (Equations (2.23)and (2.24)).

The interest by using the P controller instead of PI controller, is to keep the rotor flux linkage close to the stator flux linkage instead of maintaining it accurately.

$$V_{rd-ref} = k_P(\phi_{rd}^* - \phi_{rd}) + V_{rdc} \quad (2.21)$$

$$V_{rq-ref} = k_P(\phi_{rq}^* - \phi_{rq}) + V_{rqc} \quad (2.22)$$

Where k_P is the gain of the P controller, V_{rdc} and V_{rqc} are feed-forward components defined as:

$$V_{rdc} = \frac{R_r M}{L_s L_r - L_s^2} \phi_{sd} + \omega_{sr} \phi_{qd} \quad (2.23)$$

$$V_{rqc} = \frac{R_r M}{L_s L_r - L_s^2} \phi_{sq} + \omega_{sr} \phi_{rd} \quad (2.24)$$

2.3.1.2 Feasibility of the active method

The active method is limited for deep voltage dips. The choice of power converters used in the system can contribute to this limitation. In fact, changing power converters design can affect the cost of the system which is not desirable. Therefore, using active method for LVRT alone against voltage dips is not recommended.

The problem during a grid fault is that the stator reactive power must remain within the limits imposed by the grid code. Thus, only $0.3Pu$ of reactive power could be tolerated. So, a voltage dip caused by a grid fault has to be studied.

It is a known fact that a voltage dip is characterized by two parameters: the amplitude and the duration. The maximum amplitude is demonstrated theoretically, while the duration of the maximum dip is obtained by simulation.

2.3.1.3 Maximum amplitude of a voltage dip

To find the maximum amplitude of the voltage dip that the DFIG can handle with the active method of LVRT, a reactive power control has to be studied. Indeed the

variations in the reactive power during the appearance and disappearance of the fault must be limited to ensure a stable operation of the system. The amount of reactive power during the occurrence of the fault, must be below a limit value of $Q = 0.3Pu$. The reactive power is expressed by equation (2.25).

$$Q_s = 1.5v_s I_s \quad (2.25)$$

With:

$$I_s = \frac{1}{L_s L_r - M^2} (L_r \phi_s - M \phi_r) \quad (2.26)$$

Note that $\frac{M}{L_s} \approx 1$ it can be approximately expressed by equation (2.27)

$$I_s \approx \frac{M}{L_s L_r - M^2} (1 - k_t) \phi_s \quad (2.27)$$

Substituting equation (2.27) and equation (2.25), the reactive power becomes:

$$Q_s = 1.5 \frac{M}{L_s L_r - M^2} (1 - k_t) \phi_s v_s \quad (2.28)$$

Substituting equation (2.11) and equation (2.28), the reactive power becomes:

$$\overline{Q_s} = 1.5 \frac{M}{L_s L_r - M^2} (1 - k_t) \frac{pV_s}{j\omega_s} e^{j\omega_s t} + \frac{(p-1)V_s}{j\omega_s} e^{-t/\tau_s} \quad (2.29)$$

With: $V_2 = pV_s$

Assuming that the voltage dip occurs at $t = 0s$ and $k_t = 0.8$, equation (2.29) becomes:

$$Q_s(t = 0) = -1.5 \frac{M}{L_s L_r - M^2} (1 - k_t) \frac{1 - 2pV_s^2}{j\omega_s} \quad (2.30)$$

So the active method remains valid for voltage dips less than $0.3 = 30\%$.

$$Q_s(t = 0) < 0.3 \Rightarrow p > 0.6998 \approx 0.7 \quad (2.31)$$

Voltage dip level	Duration	Grid codes
30%	0.3s	—
25%	1s	Spain – Danemark-UK
23%	1.5s	Spain – Danemark-UK-Allemand
<23%	>1.5s	Spain – Danemark-UK-Allemand

Therefore the modified control strategy remains valid for voltage dips lower than 30%.

2.3.1.4 Maximum duration of a voltage dip

The figure 2.3 shows a maximum length of the voltage dips simulation results for a voltage dip of 30%, 25% and 23%. In figure 2.3.a, DFIG has been submitted to a 30% of voltage dip and to several voltage dips durations. This study aims to find a dip duration that the DFIG reactive power not exceed the tolerated value of $0.3Pu$ required from grid codes. For example, for a 30% of voltage dip and for dip duration equal to 0.4s, the reactive power exceeds $0.3Pu$ and the value measured is $0.4Pu$. However, a 30% of voltage dip and for dip duration equal to 0.3s, the reactive power keep an allowed value.

In figures 2.3.b and 2.3.c, the voltage dip is decreased to 25% and to 23%. The aim of this study is to see its effects on the reactive power value. Then, for 25% of voltage dip, the maximum duration is founded equal to 1s, and for voltage dips < 23%, it is shown that the maximum duration can exceed 1.5s. Thus, it is noticed that the maximum duration for a voltage dip changes depending on the nature of the grid fault. Therefore, for low voltage dips, the maximum dip duration of the grid fault is larger compared with high voltage dips.

The following table illustrates the operating extremes of the active strategy, at the amplitude and duration levels of voltage sags to verify its compatibility with existing grid codes represented in Figure 2.4.

2.3.1.5 The passive method

Figure 2.5 shows DFIG with SDBR and DC-Copper. Series dynamic breaking resistor is connected with DFIG stator. DC-Chopper is connected between GSC and DC-link.

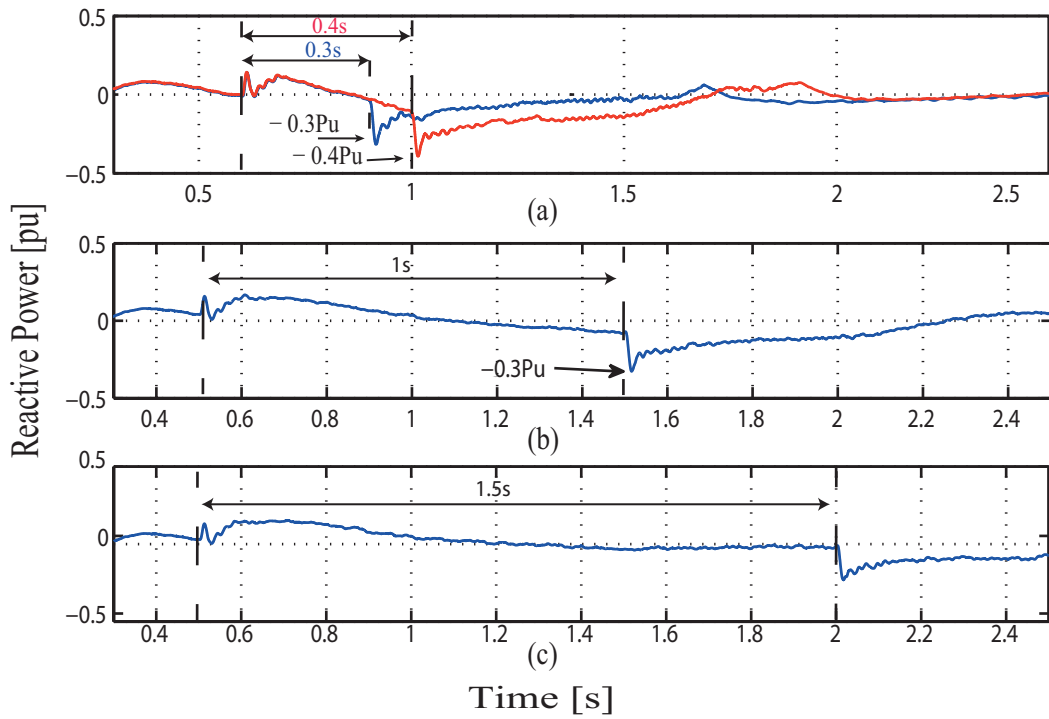


Figure. 2.3. the reactive power for voltage dips a) 30% of voltage dips , b) 25% and c) 23%.

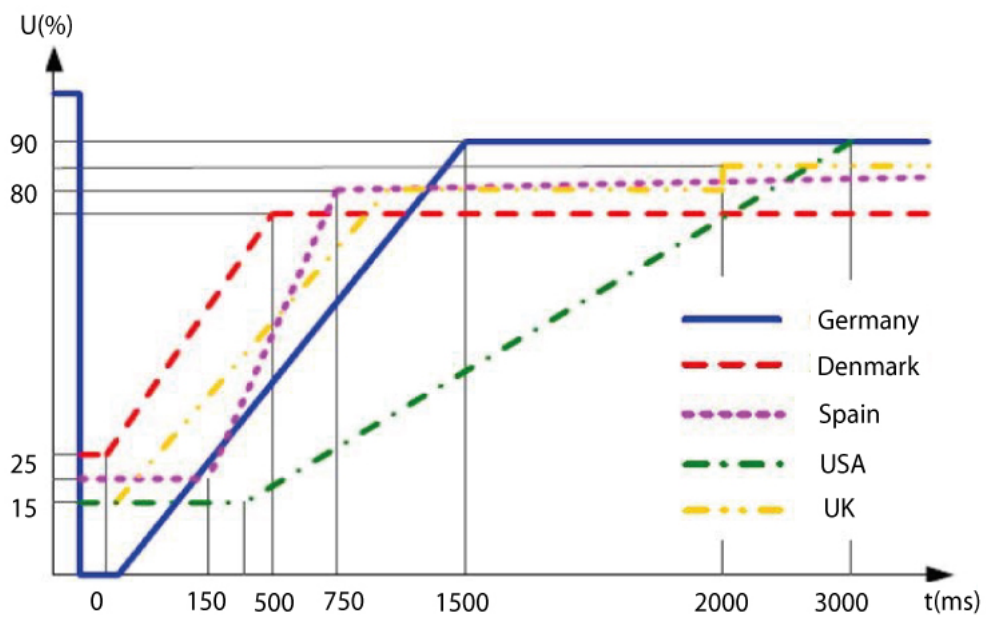


Figure. 2.4. LVRT requirements

2.3.1.6 Series dynamic breaking resistor SDBR

SDBR approach is a resistor bank connected in series with stator windings. This approach has several advantages during grid faults like increase the stator voltage, reduce the rotor current, mitigate the electrical torque and active power dips. Adding SDBR to the system, a design study of the SDBR and its impact on the system behavior during a grid fault is required. The extreme values of the SDBR can be defined by two conditions.

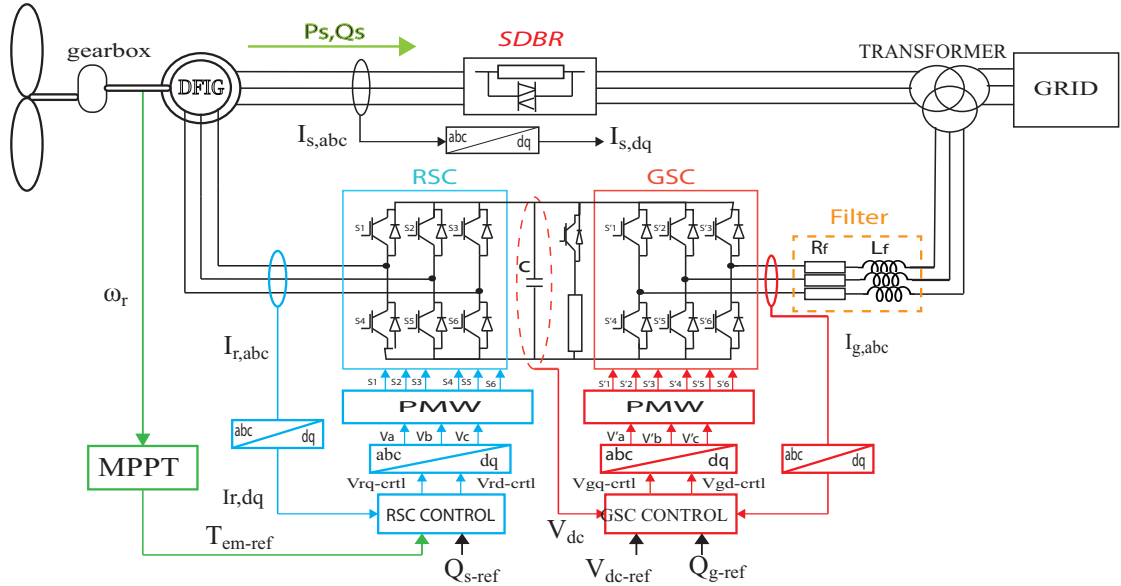


Figure. 2.5. DFIG with SDBR

1. The first extreme value of the SDBR is used to avoid the lost of control of the RSC. Thus, the minimum value of resistance that must be able to protect the RSC against rotor over-voltage during a full voltage dip has to be calculated. Equation (2.32) expresses the case where the value of rotor voltage during full 100% voltage dip should not exceed the maximum RSC converter voltage.

$$e_{r0,max}^r \leq V_{RSC,max} \quad (2.32)$$

2. The first extreme value of the SDBR is used for stator windings protection against over-voltage during the grid faults. Therefore, this protection is provided by the maximum value of the resistance. This resistance value must be able to not increase the voltage which cannot exceed the specified maximum stator voltage during grid faults. equation (2.33) represents the condition which the SDBR maximum voltage value adding to the grid voltage has to not exceed the maximum stator voltage.

$$V_{SDBR,max} + V_1(1 - p) \leq V_{Smax} \quad (2.33)$$

The extreme values of the SDBR calculated according to conditions mentioned previously (equations (2.32) and (2.33)) have been given by equation (2.34).

$$0.05pu \leq R_{SDBR} \leq 1.25pu \quad (2.34)$$

The passive method consists of inserting resistors in series with stator windings, as shown in Figure 2.5, to increase the stator voltage and subsequently reduce the DC component at flux level. This would reduce overvoltage at the rotor circuit and therefore avoid rotor current peaks.

In addition, the limitation of the rotor current can also reduce overvoltage at Vdc which could damage the power converter. The stator voltage during fault becomes the sum of the grid voltage and the voltage across the resistors.

The choice of the value of the dynamic resistance is important, a large resistance value will result in a large power dissipation, and lower voltages across the rotor. On the contrary, a low-value of the resistors cannot limit the fault current. The dimensioning of the resistance is determined according to two values:

- The resistors must be large enough to limit the rotor voltage to the maximum input voltage tolerated by the converter, thus avoiding its deterioration. Hence the following condition must be satisfied:

$$e_{r,max}^r \leq V_{RSC,max} \quad (2.35)$$

Since the RSC can only produce a voltage lower than the DC voltage, its maximum output value $V_{RSC,max}$ is calculated as follows:

$$V_{RSC,max} = \frac{V_{dc}}{2\sqrt{\frac{2}{3}}} \quad (2.36)$$

- The resistors must be small enough to prevent the stator voltage exceeding his maximum voltage value.

During the grid fault, the stator voltage can be expressed by the sum of grid voltage and the voltage across the resistors.

$$V_2 = V_1 (1 - p) + V_{SBR} \quad (2.37)$$

The voltage V_{SBR} is limited by the maximum stator voltage V_{Smax} , and we have:

$$V_{SBR,max} \leq V_{Smax} - V_1 (1 - p) \quad (2.38)$$

Replacing V_{SBR} by $V_{SBR} = R_{SBR} * I_s$, and we considered the worst case $p = 1$. We find:

$$\frac{1}{I_s} \left\{ (1 - g) V_1 - \frac{M}{L_s} \frac{V_{dc}}{2\sqrt{\frac{2}{3}}} \right\} \leq R_{SDBR} \leq \frac{V_{Smax}}{I_s} \quad (2.39)$$

2.3.2 HVRT control strategy

In this section, the capability of DFIG using DVR is proved for symmetrical grid voltage swells. When symmetrical grid fault occurs, the DVR control output voltage maintains the stability of the system to avoid the stator and rotor overcurrent and overvoltage. Thus, the power outputs of DFIG are concertedly controlled in order to keep the operation's safety and stability of the grid. The system with the DVR is represented in Figure 2.6.

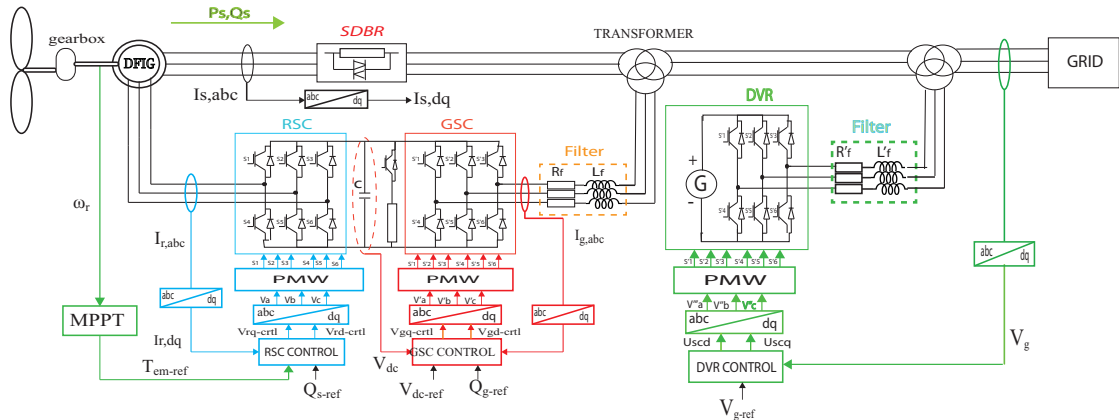


Figure. 2.6. DFIG system with DVR.

A) Dynamic Voltage Restorer control;

The goal of DVR control during voltage swells is to keep the voltage stability on the connection point with the grid, thus, by controlling it to keep the pre-fault state of grid voltage as:

$$V'_g = V_g \quad (2.40)$$

Where: V_g is the grid voltage during the normal operation; V'_g is the grid voltage during the voltage swells.

During normal operation, V_g is oriented along d-axis, by DVR control, the voltage at the connection point can be controlled to keep the same state before voltage swells. Grid voltage vector during a voltage swells can be expressed as:

$$\begin{cases} V_g = u_{gd} = V'_{gd} \\ 0 = u_{gq} = V'_{gq} \end{cases} \quad (2.41)$$

Where: u_{gd} and u_{gq} are stator voltage vector in d-q-axis reference frame during normal operation; V'_{gd} and V'_{gq} are grid voltages respectively d-axis and q-axis component during the fault; V_g is the amplitude of the grid voltage during normal operation, the voltage equations of DVR are expressed as:

$$\begin{cases} u_{gcd} = [Kp_1(\tau_{i1}s + 1)/(\tau_{i1}s)](V_g - V'_{gd}) \\ u_{gcq} = [Kp_1(\tau_{i1}s + 1)/(\tau_{i1}s)](0 - V'_{gq}) \end{cases} \quad (2.42)$$

Where: K_{p1} and τ_{i1} are the parameters of the PI controller. According to equation 2.42, the control block of DVR during grid fault is shown in Figure 2.7.

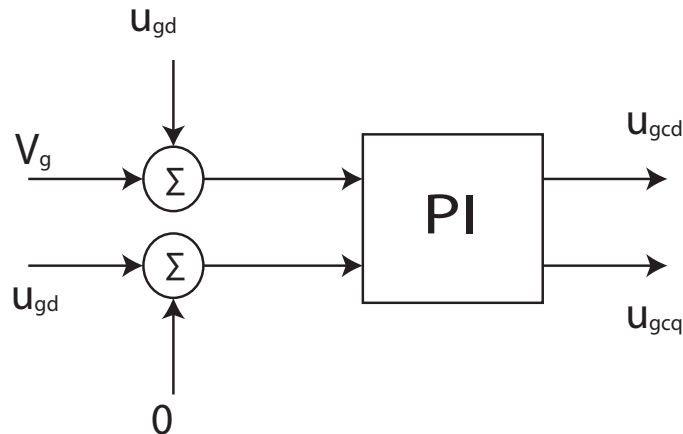


Figure. 2.7. Control diagram of DVR during grid voltage swells.

B) RSC control;

In order to improve the HVRT of the DFIG system during voltage swells, the conventional control strategy for power converter must be changed to avoid the rotor and stator current disturbs and electromagnetic torque oscillations. On the other hand, to stabilize reactive power by controlling power converter. During symmetrical grid voltage swells and by ignoring the stator resistance, the generator active power P_s and reactive power Q_s can be written as:

$$\begin{cases} P_s = V_{sq}i_{sq} = V_s i_{sq} \\ Q_s = V_{sq}i_{sd} = V_s i_{sd} \end{cases} \quad (2.43)$$

From equation 2.43, in order to keep the same state of active power, q-axis vector of stator current must remains stable, meanwhile, in order to support the grid during voltage swells by maximizing the absorption of reactive power, the d-axis component of stator current must take its maximum value:

$$I_{sdmax} = \sqrt{I_{smax}^2 - I_{sq}^2} \quad (2.44)$$

Where: I_{smax} for the stator maximum value. Combined stator flux equation and 2.44 during a voltage swell, the d-q-axis components of the rotor current can be expressed as:

$$\begin{cases} I_{rd} = \frac{\psi_s}{L_m} - \frac{L_s}{L_m} i_{sdmax} \\ I_{rq} = -\frac{L_s}{L_m} i_{sq} \end{cases} \quad (2.45)$$

Thus the equations for RSC control block during voltage swell are expressed by:

Where: V'_{rd} and V'_{rq} are respectively d and q-axis component of the RSC current loop controller output voltage; K_{p2} and τ_{i2} are parameters of the PI controller. The control block of RSC during voltage swell is represented in Figure 2.8.

$$\begin{cases} V'_{rd} = \left[\frac{K_{p2}(\tau_{i2}s+1)}{\tau_{i2}s} \right] (I_{rd} - i_{rd}) \\ V'_{rq} = \left[\frac{K_{p2}(\tau_{i2}s+1)}{\tau_{i2}s} \right] (I_{rq} - i_{rq}) \end{cases} \quad (2.46)$$

C) GSC control.

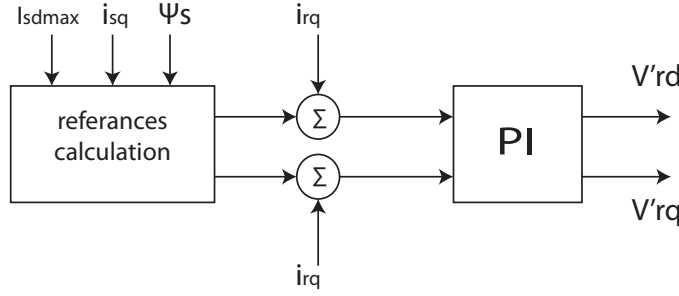


Figure. 2.8. RSC control diagram during grid voltage swells.

When symmetrical grid voltage swell happens, the GSC is still unchanged for the control of DC link voltage. But when the magnitude of the grid voltage increases, DFIG should absorb reactive power depending to the magnitude of grid voltage swell. When GSC using grid voltage oriented vector control method and ignoring the line resistance R_g , the GSC output voltage is expressed as follow:

$$\begin{cases} U_g = -\omega_s L_g I_{gq} + V_{gd} \\ 0 = \omega_s L_g I_{gd} + V_{gq} \end{cases} \quad (2.47)$$

Where: U_g is the amplitude of the grid voltage vector; L_g is the line inductance; V_{gd} and V_{gq} are respectively d-axis and q-axis components of the GSC output voltage; I_{gd} and I_{gq} are d-axis and q-axis components of the GSC current.

According to the vector modulation theory, at no over-modulation condition, the modulation ratio m shall meet:

$$m = \left[\frac{\sqrt{V_{gd}^2 + V_{gq}^2}}{\frac{V_{dc}}{2}} \right] \leq 2/\sqrt{2} \quad (2.48)$$

From equations 2.47 and 2.48 we can deduct:

$$V_{dc} \geq \sqrt{3[(V_g + \omega_s L_g I_{gq})^2 + (-\omega_s L_g I_{gd})^2]} \quad (2.49)$$

From equation 2.49, the minimum GSC reactive current I_{gqmin} required can be expressed as:

$$I_{gqmin} = \frac{1}{\omega_s L_g} \left[\sqrt{\frac{U_{dc}^2}{3} - (-\omega_s L_g I_{gd})^2} - U_g \right] \quad (2.50)$$

During the grid voltage swells, to achieve the HVRT requirement, GSC should absorb at least the minimum reactive power Q_{gmin} as:

$$Q_{gmin} = -I_{qmin} U_g \quad (2.51)$$

Thus the equations for current loop control of GSC are:

$$\begin{cases} V'_{gd} = \left[\frac{K_{p3}(\tau_{i3}s+1)}{\tau_{i3}s} \right] (I_{gd} - i_{gd}) \\ V'_{gq} = \left[\frac{K_{p3}(\tau_{i3}s+1)}{\tau_{i3}s} \right] (I_{gq} - i_{gq}) \end{cases} \quad (2.52)$$

The control block of GSC during grid fault is shown in figure 2.9.

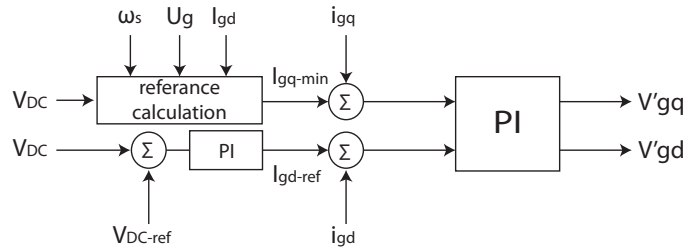


Figure. 2.9. GSC control diagram during grid voltage swells.

2.4 Combining HVRT and LVRT methods

To ensure a great management of any types of grid faults, we propose a combination strategy between LVRT and HVRT strategies. Figure 2.10 shows the algorithm of FRT strategy proposed. Through normal operation, grid voltage is measured in real time to look over grid faults and its nature. In the meanwhile, a grid fault is tested by measuring in real time the grid voltage. In addition, during voltage dips which passed 30%, the grid voltage measured is between 0,7pu and 0,9pu, only the active method is used (Figure 2.10, option 1). Thus, in this range, active method is more coherent, and SBR protection is not working. On the other hand, for high voltage dips higher than 30%, only the SBR is used with conventional control (Figure 2.10, option 2).

Moreover, if the depth of the voltage swell is higher than 10%, the grid voltage measured is higher than 1.1pu, the DVR strategy is activated (Figure 2.10, option 3) with the proposed control fitting the improvement of the safety and the stability of the grid

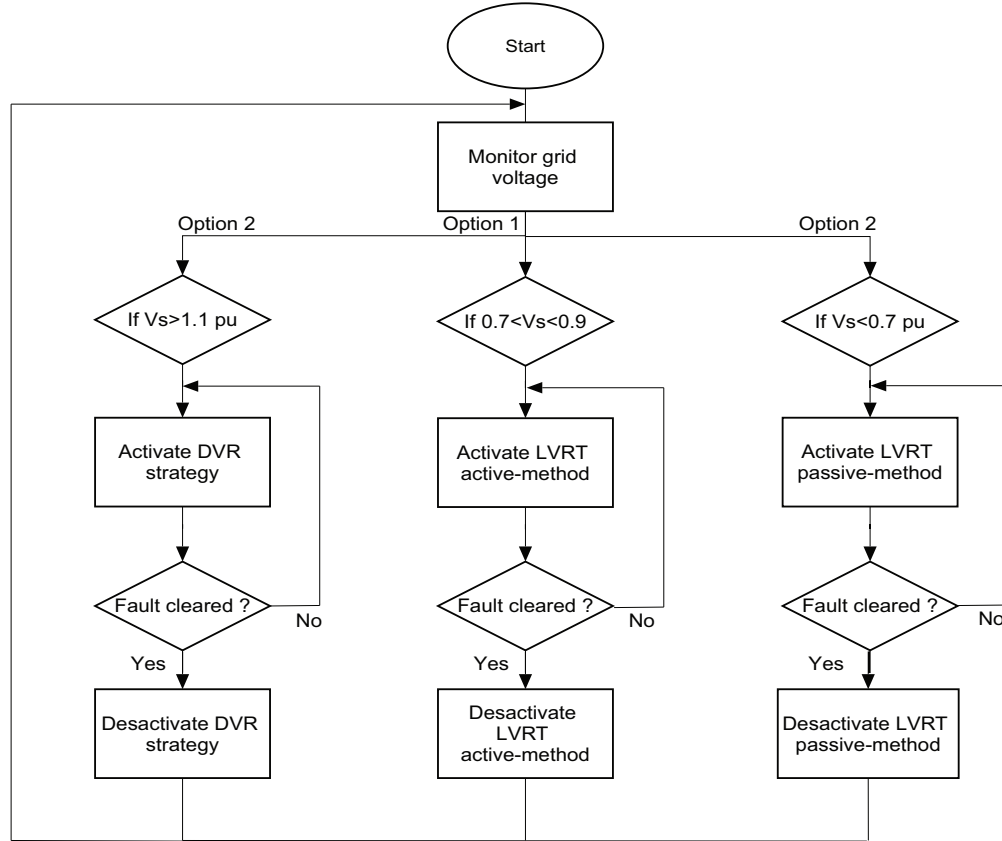


Figure. 2.10. the flowchart of the proposed strategy based on the combination of HVRT and LVRT methods.

under voltage swells. Finally, when the fault ends the system respond to a normal operation.

2.5 Simulation & results

The main results of the work were achieved by doing simulations with MATLAB-SIMULINK software and Simscape SimPowerSystems toolbox (DFIG parameters is given in table 2.1).

The DFIG FRT capability is simulated for two types of grid fault: (i) three-phase voltage sag in which the grid voltage down by $0.1pu$ (10% of its rated value) at $t=0.7s$ and lasts for 150ms, and to $0.75pu$ (75% of its rated value) at $t = 1.2s$ and lasts for 200ms as shown in figure 2.11. (ii) three-phase voltage swell in which the grid voltage increase to $1.3 pu$ at $t = 0.7s$ with a duration of 100ms as shown in Figure 2.13.

Table. 2.1. DFIG parameters

Stator (Star connection)	
Rated voltage V_{sn}	575V
The stator resistance R_s	0.023 pu
The stator inductance L_s	3.08 pu
Mutual inductance M_{sr}	2.9pu
Rotor (Star connection)	
Rated voltage V_{rn}	1975V
The rotor resistance R_r	0.016 pu
The rotor inductance L_r	3.06 pu
Mechanical quantities	
Number of pole pairs p	3
Moment of inertia J	0.685s
Coefficient of friction f	0.01pu

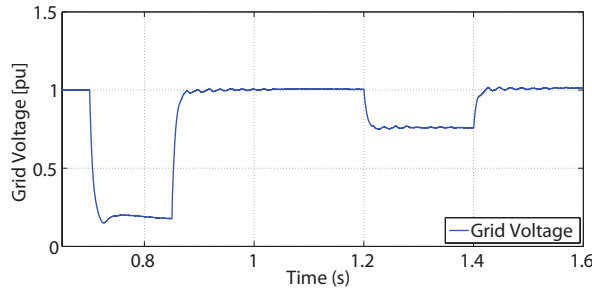
**Figure. 2.11.** Grid voltage during two voltage dips.

Figure 2.12 shows the simulation results of different electric quantities for the system with and without LVRT strategy. The first voltage sag of a grid fault had started at $t = 0.7s$, in figure 2.12.(a) through the first 90% voltage sag, the passive method is activated. It is shown that the active power of the system without LVRT technique reaches $0.1pu$ which exceeded the DFIG operation limit ($0.7pu$) also, the DFIG is ended. However, with the LVRT advanced method, the active power rest in the safe operation range ($0.7pu$ – $1.3pu$). When the voltage sag ends at $0.85s$, the DFIG starts and the active power leads $2.24pu$ for the system without LVRT technique. Nevertheless, the proposed LVRT method regards the range of normal operation and doesn't notice any active power peak. The next voltage sag is 25%, in this time the active method is operated and the passive method is deactivated. The present results report the efficiency of the proposed approach, it maintains the stability of the production.

In Figure 2.12.(b) relieve that the combined method considers grid requirements. In fact, the reactive power has to be maintained at least within $0.3pu$ and $0.4pu$. Moreover, the

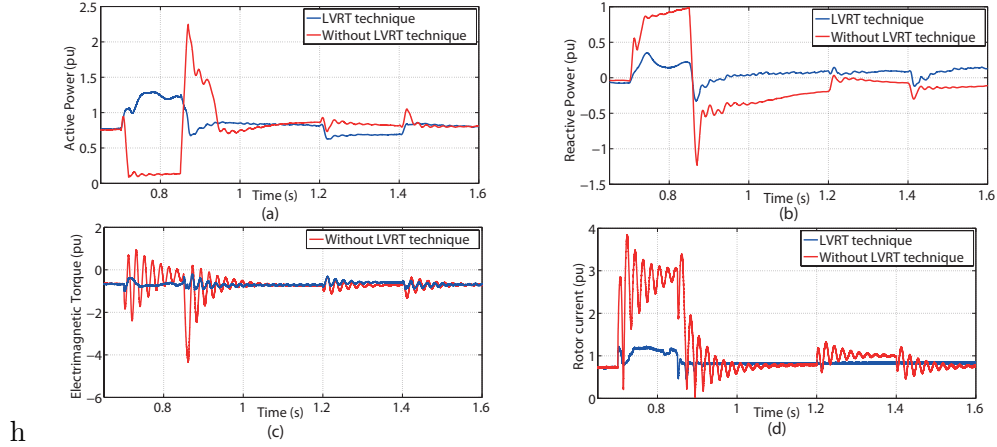


Figure. 2.12. Simulation results of different electric quantities for the system with and without LVRT strategy.

system without LVRT strategy exceeds the limit of the reactive power and can affect the grid.

Figure 2.12.(c) and Figure 2.12.(d) show the simulation results of the electromagnetic torque and the rotor current. It is shown that the system without LVRT strategy has serious oscillations in electromagnetic torque and rotor current, which is very limited near its nominal value by using the SBR. In addition, for a system without LVRT, rotor current passed the permissible value (2pu). Moreover, it is shown that when the fault is started, rotor current has dangerous peaks with strong oscillations, which have an important influence on the performance of the mechanical part of DFIG and the protection of the power converters. Actually, serious oscillations can destroy the machine and the power converter.

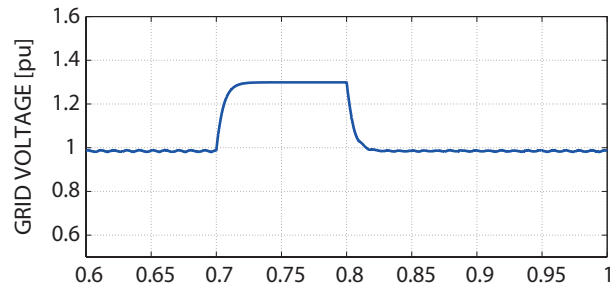


Figure. 2.13. Grid voltage during a voltage swell.

During the grid voltage swells, Figure 2.14.(a) show that the amplitude of the stator voltage was remarkably expanded with the grid voltage swells to 1.3pu , which will possibly be harmful to the stator insulation level, but with the proposed strategy, DVR compensates the change in grid voltage, as consequence, the stator voltage holds the

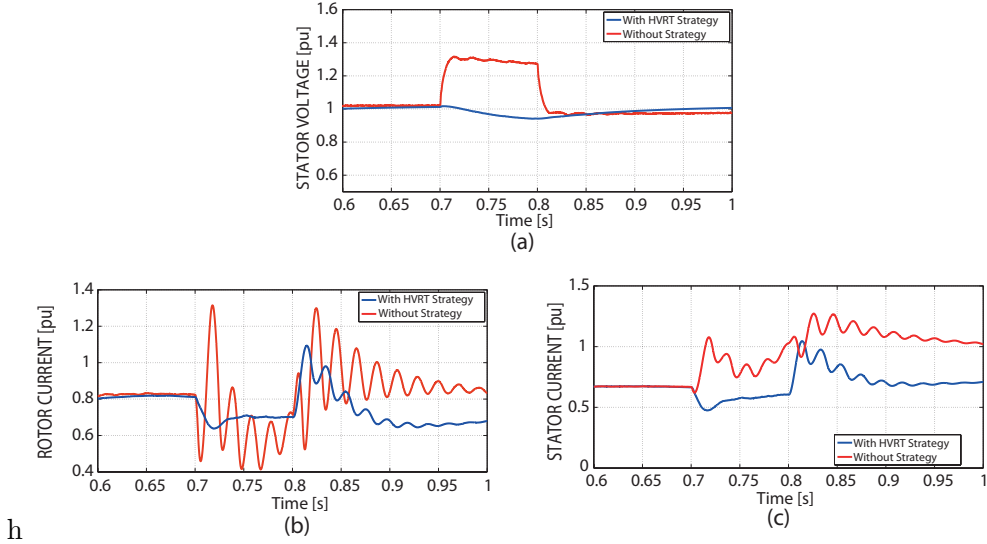


Figure. 2.14. Simulation results of different electric quantities for the system with and without HVRT strategy.

pre-fault state. Figure 2.14.(b) and Figure 2.14.(c) show that without DVR the rotor and stator over-currents contain a large transient DC component during voltage swells. Therefore, with the strategy proposed the transient DC component of stator flux could be effectively reduced.

According to Figures 2.15.(a),(b) and (c), the electromagnetic torque, active power and reactive power present significant fluctuations, which will have an impact on mechanical components of DFIG, at the same time significantly reduce grid power quality, but with the proposed strategy, the fluctuations in electromagnetic torque and power output was significantly amortized and, in fact, the impact on the WT will be reduced. In addition, the proposed strategy can support the grid power quality during the faulty operation. From Figure 2.15.(d)we remark that the DC-link voltage is almost substantial, by using the proposed strategy which remains the safety and the stability of the DC link.

2.6 Conclusion

The LVRT and HVRT capabilities of wind turbines are necessary with the increasing integration of wind energy and contribute to the regular grid integration. This part has investigated the performance of the passive and active methods for FRT capability of DFIG. Hence, The LVRT strategy is based on the active method which used a P controller that valid only for low voltage sags less than 30%, also an SDBR coupled in series

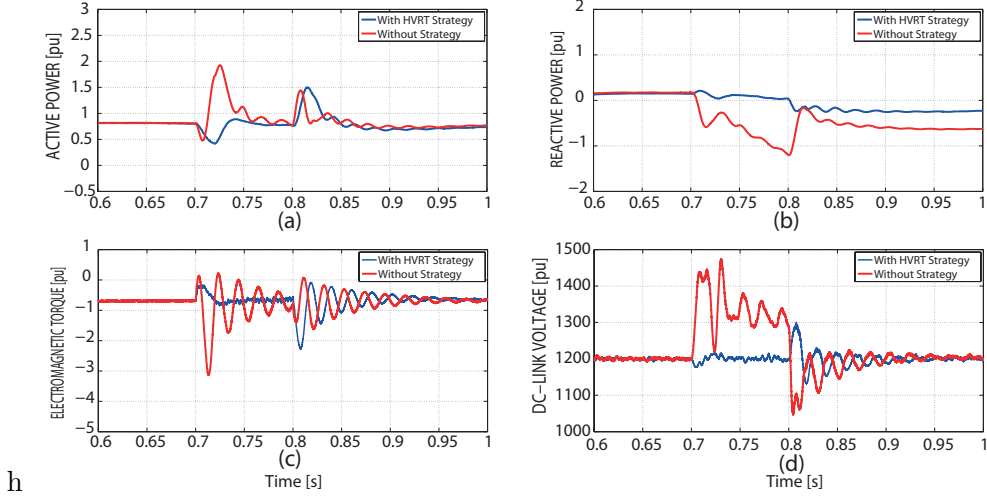


Figure. 2.15. Simulation results of different electric quantities for the system with and without HVRT strategy.

with the stator windings is used for the passive method. Besides, the proposed HVRT strategy is based on adding a DVR, which provides the balance of the grid voltage by controlling the reactive power. The simulation results have been allowed an indication of the proposed method behavior during any voltage faults. Furthermore, the results of the simulation obtained using a grid-connected 1.5MW DFIG demonstrate the great performance of the proposed strategies for improving the FRT capability of DFIG.

This work is published in two indexed journals: [3] et [11]

1 - El Makrini, A., El Karkri, Y., Boukhriss, Y., El Markhi, H., & El Moussaoui, H. (2017). LVRT control strategy of DFIG based wind turbines combining passive and active protection. *Int. J. Renew. Energy Res*, 7, 1258-1269.

2 - El Karkri, Y., El Markhi, H., El Moussaoui, H., & Lamhamdi, T. (2018). LVRT and HVRT control strategies of Doubly-Fed Induction Generator. *Journal of Electrical Systems*, 14(4).

Chapter 3

Improved Control of Grid-connected DFIG-based Wind Turbine using Proportional-Resonant Regulators during Unbalanced Grid

3.1 Introduction

In the same context of the previous chapter; in the functional command of the DFIG, the vector control with the orientation of stator voltage or stator flux has been commonly used [11]. By using this type of control strategy, the Proportional Integrator (PI) regulators are classically aiming to regulate the power transfer into the utility grid. However, when a voltage sag takes place, the PI controller seems to be overloaded rapidly. In addition, the system regularization is tough to realize. Therefore, the DFIG loses command ability. In order to manage the traditional vector control weakness, different approaches were proposed to improve strategies to reach the Low-Voltage Ride-Through (LVRT). According to the obtained results for the traditional DFIG vector controller [34–36],

the generator still operates within a specific range during a grid fault. Nevertheless, the acquisition of two state variables dynamic response, such as rotor voltage and rotor current, cannot be assured. This technique can only be used under symmetrical grid fault.

Some research papers have investigated the control and behaviour of grid-connected DFIG converters under the abnormal behaviour of the grid voltage. In [37, 38], two regulators were used for the current loop's control after the separation of the Positive and Negative Sequence Components (P-N SC) of the three-phase grid voltages, which can increase the delay and errors of the dynamic response and affect the system stability during this process. The same appears in [38] and [39], under unbalanced grid conditions, the main regulator was employed in the positive sequence synchronous reference frame and a secondary regulator employed in the negative sequence synchronous reference frame. In references [40, 41] a PI-R current regulator are applied in order to eliminate multiple harmonics in grid converter systems during grid voltage distortion but a non-linear transformations $abc \rightarrow dq$ is mandatory. The operation of DFIG under the abnormal operation of the utility grid was studied in [42, 43] and many possibilities for reducing oscillations at twice the fundamental frequency have been investigated. However, the Rotor Side Converter (RSC) was examined in this work and two current regulators were implemented for the P-N SC. Furthermore, because of the RSC limited control, it is so difficult to obtain a simultaneous rejection of power oscillations and so, an improved control method is used to deal with unbalanced grid voltages. Unlike the described techniques, this work proposes a new flexible current reference generation method that injects sinusoidal currents even under unbalanced grid faults using Clark's transformation, which converts a three-phase sinusoidal system (abc) into a two-phase sinusoidal system in orthogonal ($\alpha \beta$) axes and allows PR regulators to track and reject sinusoidal variables. The use of the stationary reference frame is possible with the proposed algorithm, in order to reduce the computational difficulty and avoid the application of the synchronous reference frame. Thus, the non-linear transformation ($abc \rightarrow dq$) used with PI-R regulators is changed by the linear ($abc \rightarrow \alpha\beta$) transformation using the Proportional-Resonant (PR) controllers [44, 45]. Moreover, as explained in Section 3, PR regulators can control the two sequences generated during grid voltage faults. This work explores an application of the PR regulators on the DFIG's Grid Side Converter (GSC), mainly in their capability for the compensation of reactive power, grid

current limitation and the stabilization of active power during asymmetrical grid faults.

The work novelty can be observed in the LVRT proposed algorithm according to the IEC 61400-21 [46] normative and the Spanish grid code, generating the P-N SC of the grid currents with the implementation of the PR regulators on the DFIG's Grid Side Converter (GSC) to the $\alpha\beta$ components of the 3-phase inverter currents. This feature will have the capability for the compensation of reactive power and the grid current limitation during a grid fault according to the Spanish grid code.

3.2 DFIG Control

The electrical part of DFIG consists of 3-phases stator windings which are connected to the 3-phases windings transformer, while the 3-phase machine's rotor windings are directly excited by two power converters RSC and GSC respectively, the grid side of the power converters delivers the rotor power into the grid via the 3-winding transformer. The schematic block of the DFIG connected to the utility grid is shown in Figure 3.1. The rotor voltages control makes it possible to manage the magnetic field inside the machine.

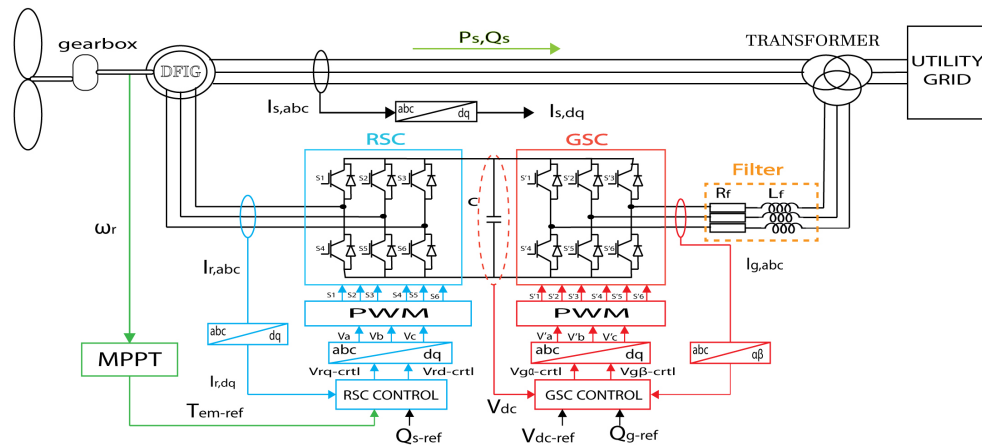


Figure. 3.1. DFIG system connected to the utility grid.

The equivalent electrical circuit of the rotor and the stator windings in an arbitrary reference frame is represented in Figure 2. According to this figure the stator and the rotor fluxes (ϕ) are expressed by equations 3.1 and 3.2:

$$\varphi_s = L_s i_s + M i_r \quad (3.1)$$

$$\varphi_r = L_r i_r + M i_s \quad (3.2)$$

where L_r and L_s are the rotor and stator inductance, and M is the mutual inductance. i_s and i_r are the stator and the rotor current. Also, the stator and the rotor voltage can be written according to Figure 3.2: .

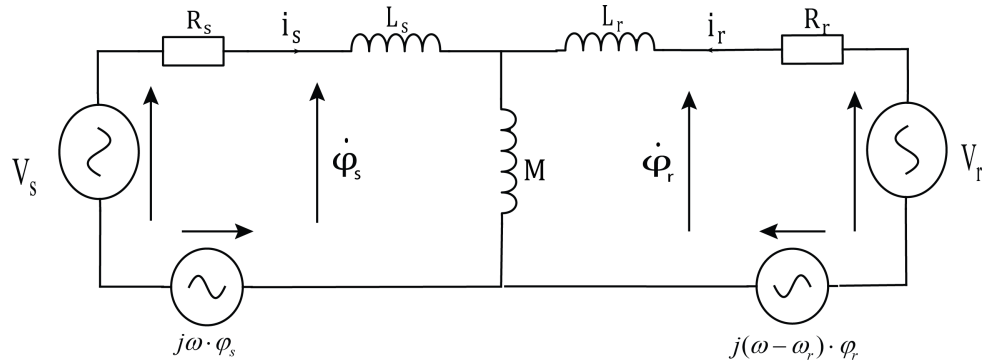


Figure. 3.2. The equivalent electrical circuit of the DFIG.

Based on equations (3.1) and (3.2), the rotor flux and the stator current can be written as:

$$\varphi_r = \frac{M}{L_s} \varphi_s + \sigma L_r i_r \quad (3.3)$$

$$i_s = \frac{1}{L_s} (\varphi_s - M i_r) \quad (3.4)$$

where σ is the leakage factor $\sigma = 1 - \frac{M^2}{L_r L_s}$

Then, the expression of the rotor voltage in the arbitrary rotating reference can be written as:

$$V_r = R_r i_r + \sigma L_r i_r \frac{di_r}{dt} + \frac{d\varphi_r}{dt} + j(\omega - \omega_r) \left(\frac{M}{L_s} \varphi_s + \sigma L_r i_r \right) \quad (3.5)$$

The purpose of a reference change is to make the machine equations easier to use. In this study, the Park's transformation (two d-q orthogonal axes in the rotating synchronous reference frame) is used for RSC control to apply the vector control technic and Clarke's Transformation (two $\alpha\beta$ orthogonal axes in the stationary reference frame) for GSC control. This model is obtained after the three-phase (A, B and C) virtual transformation into an equivalent two-phase machine as represented in Figure 3.2 [47].

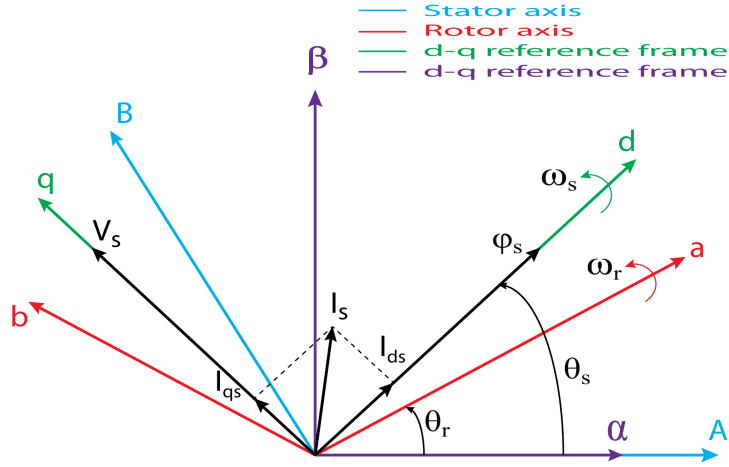


Figure. 3.3. Park's and Clarke's transformation of the DFIG system.

3.2.1 DFIG Control Strategy

After the Park's transformation application, and with a reference linked to the rotating field, the expressions of the stator and rotor voltages along the d-q axes are:

Stator voltage:

$$\begin{cases} V_{sd} = R_s i_{sd} + \frac{d\varphi_{sd}}{dt} - \omega_s \varphi_{sq} \\ V_{sq} = R_s i_{sq} + \frac{d\varphi_{sq}}{dt} + \omega_s \varphi_{sd} \end{cases} \quad (3.6)$$

Rotor voltage:

$$\begin{cases} V_{rd} = R_r i_{rd} + \frac{d\varphi_{rd}}{dt} - \omega_r \varphi_{rq} \\ V_{rq} = R_r i_{rq} + \frac{d\varphi_{rq}}{dt} + \omega_r \varphi_{rd} \end{cases} \quad (3.7)$$

where ω_s is Stator pulsation, and ω_r is the rotor pulsation. The matrix system of the flux can be written as:

Stator Flux:

$$\begin{cases} \varphi_{sd} = L_s i_{sd} + M i_{rd} \\ \varphi_{sq} = L_s i_{sq} + M i_{rq} \end{cases} \quad (3.8)$$

Rotor Flux:

$$\begin{cases} \varphi_{rd} = L_r i_{rd} + M i_{sd} \\ \varphi_{rq} = L_r i_{rq} + M i_{sq} \end{cases} \quad (3.9)$$

The expression of DFIG's electromagnetic torque as a function of the stator flux and rotor currents is written as follows:

$$T_{em} = \frac{M}{L_s} (\varphi_{sq} i_{rd} - \varphi_{sd} i_{rq}) \quad (3.10)$$

The transferred active- and reactive power from the DFIG (through the stator- and rotor windings) into the utility grid are written as follows [44]:

$$\begin{cases} P_s = V_{sd} i_{sd} + V_{sq} i_{sq} \\ Q_s = V_{sq} i_{sd} - V_{sd} i_{sq} \\ P_r = V_{rd} i_{rd} + V_{rq} i_{rq} \\ Q_r = V_{rq} i_{rd} - V_{rd} i_{rq} \end{cases} \quad (3.11)$$

In this work, we have oriented the stator flux along the d-axis to apply the vector control technique. The choice of this reference makes the generated electromagnetic torque proportional to the q-component of the rotor current i_{rq} and makes the reactive power proportional to the d-component of the rotor current i_{rd} . Thus, these stator powers can be controlled independently of each other. Two control blocks are implemented on the RSC; the maximum power extraction from the wind, and the vector control block using the PI regulators.

In the following, the Maximum Power Point Tracking MPPT is briefly explained [48]. The mechanical torque T_{em} , which is captured by the turbine, is given by:

$$T_m = 1/2\pi\rho R^2 v_w^3 C_p \quad (3.12)$$

where: ρ is the air density, C_p : the power coefficient, v_w : the wind velocity and R : the turbine radius. In order to pull out the utmost power by the wind turbine at different wind speeds, Figure 4 represents the trajectory of an MPPT curve, which can be expressed in term of the mechanical torque $T_{m,MPPT}$ by the following equation:

$$T_{m,MPPT} = K_{opt}\omega_m^2 \quad (3.13)$$

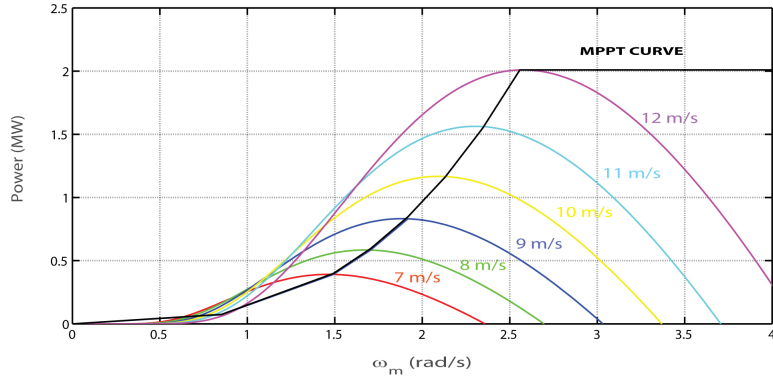


Figure. 3.4. MPPT power curve of the DFIG system.

By the orientation of the stator flux vector with d-axis and neglecting the per phase stator resistance [3], the d-component of the stator flux is written as:

$$\varphi_{sd} = \varphi_s \quad \text{and} \quad \frac{d\varphi_{sd}}{dt} = 0 \quad (3.14)$$

Therefore φ_{sd} considered constant (its derivative is zero) and equal to the modulus of the stator flux vector:

$$\begin{cases} \varphi_{sd} = \varphi_s \\ \varphi_{sq} = 0 \end{cases} \quad (3.15)$$

The stator voltage in equation 3.16 becomes:

$$\begin{cases} V_{sd} = 0 \\ V_{sq} = V_s = \omega_s \varphi_s \end{cases} \quad (3.16)$$

The electromagnetic torque in equation 3.8 is written as:

$$T_{em} = -\frac{M}{L_s} \varphi_{sd} i_{rq} \quad (3.17)$$

And the equation 3.8 of the stator fluxes according to equation 3.15 becomes:

$$\begin{cases} \varphi_{sd} = \varphi_s = L_s i_{sd} + M i_{rd} \\ \varphi_{sq} = 0 = L_s i_{sq} + M i_{rq} \end{cases} \quad (3.18)$$

Finally, reactive power and active power in equations 3.11 are written as follows:

$$\begin{cases} P_s = -\frac{M}{L_s} V_s i_{rq} \\ Q_s = -\frac{M}{L_s} V_s i_{rd} + V_s \frac{\varphi_s}{L_s} \end{cases} \quad (3.19)$$

The generator is used to convert the mechanical power into AC electrical power, and then RSC and GSC are used to control and convert that power to a grid connection. By using the GSC, the incoming AC electrical power is injected into the utility grid with its synchronized frequency and phase for power factor control. The configuration of the DFIG's RSC control blocks is shown in Figure 3.5.

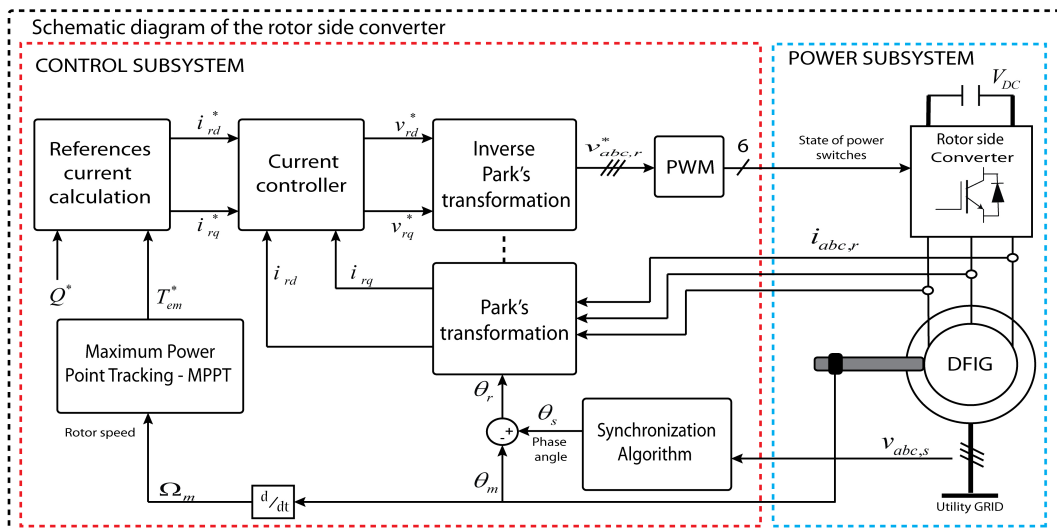


Figure. 3.5. The Schematic diagram of the rotor side converter control.

3.2.2 Grid Side Converter Regulation using PR Control

The second converter in DFIG is the GSC which controls the balance of power between the wind generator and the utility grid. The purpose of the GSC is to regulate the DC voltage in order to generate the active power reference $P_{g,ref}$ by using a PI regulator [49] and also to regulate the reactive power injected to the utility grid. The latter is achieved

by regulating properly the P-N SC of the grid currents in order to deal with the grid voltage disturbance conditions and the power oscillations furnished by the RSC to the DC-link. The P-N SC of the faulty utility grid must be calculated from the measured three-phase voltages.

The PR current regulators in the stationary reference frame are applied in this section [50]. This kind of regulators commonly consists of a P regulator plus a resonant filter tuned to the fundamental frequency in order to attain a zero state error when sinusoidal signals are controlled. A detailed study of the PR regulator was presented in [17] and so, only a short explanation is provided in this work. The transfer function of the PR controller is expressed as:

$$C_{PR}(s) = K_p + \frac{K_i s}{s^2 + 2\omega_c s + \omega_e^2} \quad (3.20)$$

where K_p is the proportional constant, K_i is the integral constant of the regulator, ω_c is the cutoff frequency and ω_e is the resonance frequency.

The expression of grid current references in the stationary reference frame $i_{g\alpha}^*$ and $i_{g\beta}^*$ are written according to the active and reactive current components $i_{g\alpha,P}^*$ and $i_{g\beta,P}^*$ and $i_{g\alpha,Q}^*$ and $i_{g\beta,Q}^*$, respectively [18]:

$$\begin{cases} i_{g\alpha}^* = i_{g\alpha,P}^* + i_{g\alpha,Q}^* \\ i_{g\beta}^* = i_{g\beta,P}^* + i_{g\beta,Q}^* \end{cases} \quad (3.21)$$

Where:

$$i_{g\alpha,P}^* = \frac{u_{g\alpha}^+ - u_{g\alpha}^-}{(u_{g\alpha}^{+2} + u_{g\beta}^{+2}) - (u_{g\alpha}^{-2} + u_{g\beta}^{-2})} P_{g,ref} \quad (3.22)$$

$$i_{g\alpha,Q}^* = \frac{u_{g\beta}^+ + u_{g\beta}^-}{(u_{g\alpha}^{+2} + u_{g\beta}^{+2}) - (u_{g\alpha}^{-2} + u_{g\beta}^{-2})} Q_{g,ref} \quad (3.23)$$

$$i_{g\beta,P}^* = \frac{u_{g\beta}^+ - u_{g\beta}^-}{(u_{g\alpha}^{+2} + u_{g\beta}^{+2}) - (u_{g\alpha}^{-2} + u_{g\beta}^{-2})} P_{g,ref} \quad (3.24)$$

$$i_{g\beta,Q}^* = -\frac{u_{g\alpha}^+ + u_{g\alpha}^-}{(u_{g\alpha}^{+2} + u_{g\beta}^{+2}) - (u_{g\alpha}^{-2} + u_{g\beta}^{-2})} Q_{g,ref} \quad (3.25)$$

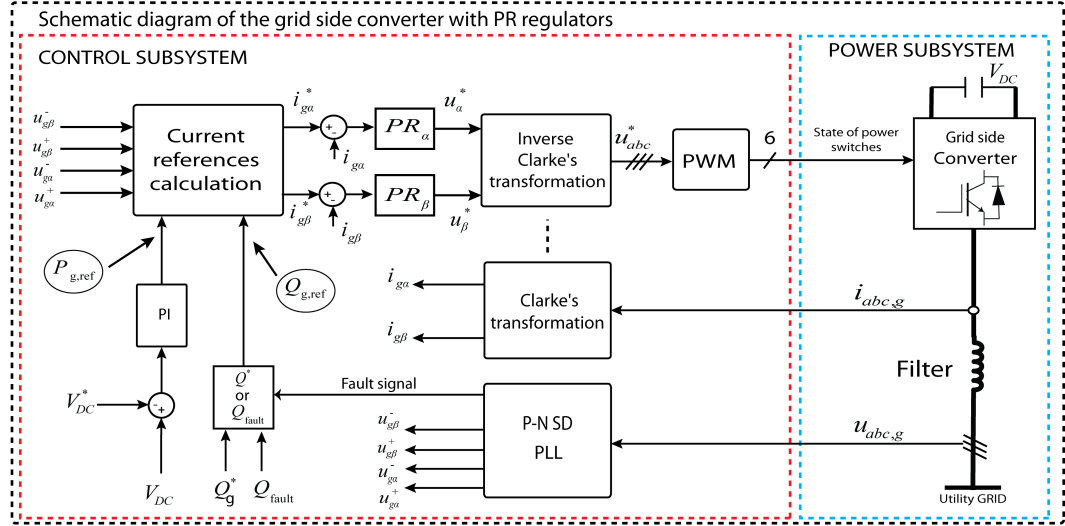


Figure. 3.6. Schematic diagram of the grid side converter control.

Figure 3.6 describes the GSC block diagram control using the PR regulators, meanwhile, the P-N SC of grid voltage are calculated from the measured grid voltage [19]. The four grid voltage components ($u_{g\alpha}^+$, $u_{g\alpha}^-$, $u_{g\beta}^+$ and $u_{g\beta}^-$) generated by the P-N SC detector together with $P_{g,ref}$ and $Q_{g,ref}$ are used to calculate the two grid currents references in the stationary reference frame ($i_{g\alpha}^*$ and $i_{g\beta}^*$) with the current references calculation module. The two currents references $i_{g\alpha}^*$ and $i_{g\beta}^*$ are compared to the measured signals, and the difference is supplied to the PR regulators. The outputs of these regulators are the inverter voltage signals in the stationary reference frame and so, the inverse Clarke's transformation is applied to these variables in order to feed the Pulse Width Modulation (PWM) block. The outputs of the PWM are the switching signals for the three-phase inverter.

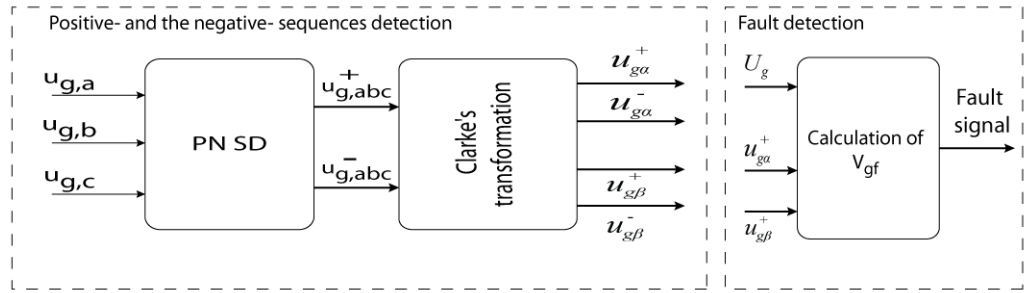


Figure. 3.7. P-N SD block.

The P-N SD block diagram is represented in Figure 3.7, the P-N SD block is used to generate the positive and the negative sequences of the grid voltage $u_{g,abc}^+$ and $u_{g,abc}^-$. After Clark's transformation, the positive sequences are used to calculate the voltage e sag in order to generate the fault signal basing on equation 3.26. The main outcomes

of this work are the generation of the P-N SC of the grid currents in an easy way by applying equations (3.21 - 3.25) in order to exert a constant active power control which will decrease the oscillations amplitude at twice the fundamental frequency in the DC bus voltage, protecting the link capacitor for its potential destruction.

3.3 Grid Code (Output Current Limitation)

The wind system must respect the LVRT requirement and must stay connected to the grid when severe faults occur, according to the grid code used. In addition, the grid code imposes the necessity to inject some reactive power for specific levels in the depth of the voltage dips [51] and to limit the amplitude of the currents to its nominal value in order to avoid the disconnection of the generator from the grid. Figure 3.8.(a) presents the LVRT requirements according to IEC 61400-21 [46], meanwhile, Figure 3.8.(b) presents the Spanish grid code requirements for the reactive power during grid fault [18].

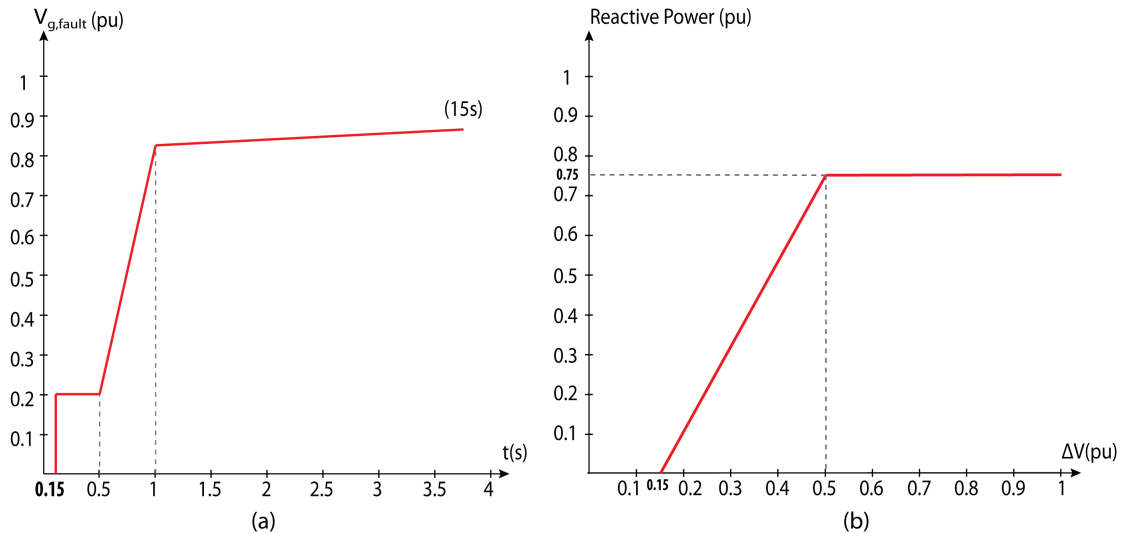


Figure 3.8. (a) LVRT requirements according to IEC 61400-21 and (b) reactive power during voltage sag according to the Spanish grid code [19].

As it was motioned in the previous section, the measured grid voltage is used to calculate the P-N SC, and the extracted positive sequence is used to detect the voltage sag by dividing it with the nominal value of the line-to-line utility grid voltage as expressed in the following equation [18]:

$$V_{g,fault} = \frac{\sqrt{u_{g\alpha}^+{}^2 + u_{g\beta}^+{}^2}}{U_g} \quad (3.26)$$

Where U_g is the line-to-line grid voltage and $V_{g,fault}$ is the normalization depth of the voltage sag. According to the Spanish grid code, a grid fault is defined by a voltage amplitude less than $0.85pu$. The organigram represented in Figure 9 describes the applied algorithm for LVRT capability and the reactive power required to inject it into the utility grid basing on the Spanish grid code. Once the voltage sag is less than $0.85pu$. The grid fault is detected. In this condition, if the grid fault is less than 0.2 for a duration $t > 0.15s$, or between 0.2 and 0.5 for more than $0.58s$, or between 0.5 and 0.85 for more than $0.27s$ then the DFIG system must be disconnected from the grid. Actually, reactive power injection becomes important, according to the depth of the grid voltage fault as given in equation 3.26:

$$\begin{cases} Q = 0 & \text{if } V_{g,fault} \geq 0.85 \\ Q = \frac{15}{7}S_{nom}(0.85 - V_{g,fault}) & \text{if } 0.5 \leq V_{g,fault} < 0.85 \\ Q = \frac{3}{4}S_{nom} & \text{if } V_{g,fault} < 0.5 \end{cases} \quad (3.27)$$

3.4 Digital Real-Time Simulation of the Rotor Side Converter

In this section, the DRTS of the planned RSC control is presented. The dSPACE DS5202 signal acquisition board together with the DS1006 processing board [52] are used for implementing the DRTS, these boards afford compatible libraries with MATLAB/Simulink software. Furthermore, dSPACE affords a monitoring software (ControlDesk) which communicates with the algorithm placed in the data acquisition board in real-time. The simulation model used in this study is made by a 2MW DFIG based wind turbine as considerate the most generators used for wind farms connected to the utility grid. Firstly, the RSC control of DFIG system with a fixed DC-link voltage ($VDC = 800V$) is simulated with the MATLAB/Simulink environment and secondly, the dSPACE blocks will be added to the system in order to run in the digital real-time simulator. The generator parameters are given in Table 3.1.

Figure 3.10 shows the real simulation results of the RSC control at a step-change in the wind turbine speed from $\omega_m = 7m/s$ to $\omega_m = 12m/s$ for a duration time of $t = 10s$ as represented in Figure 3.10.(a). According to Figure 3.10.(b), the RSC vector control

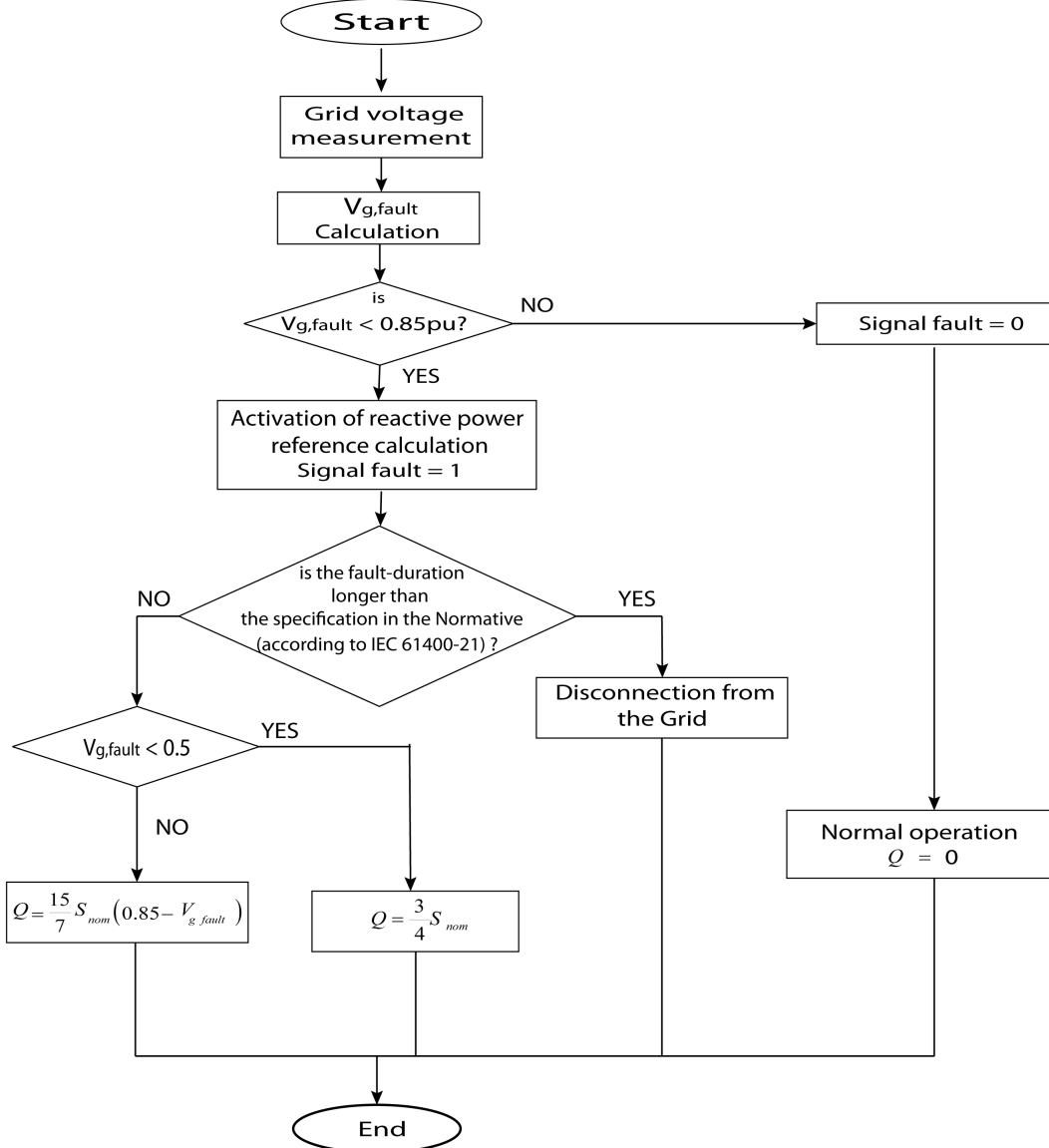
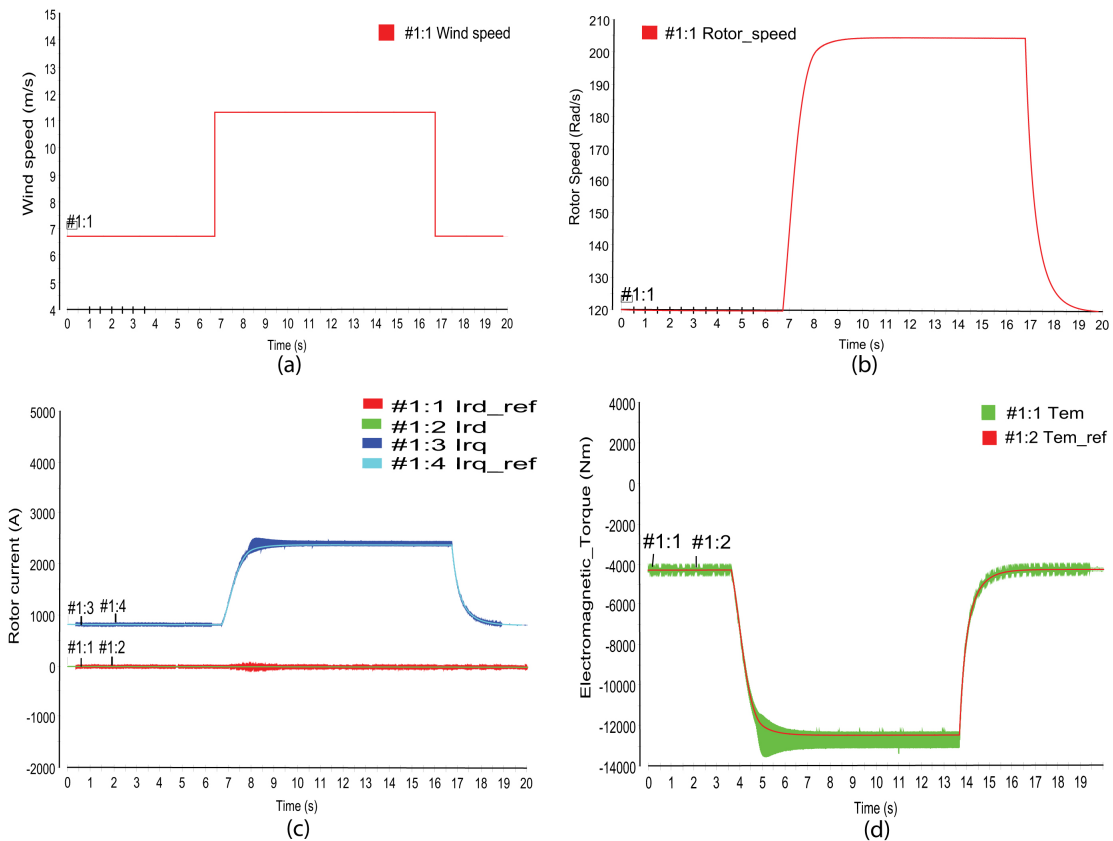


Figure. 3.9. Organigram of the LVRT algorithm.

guarantees the MPPT, the rotor mechanical speed changed with the wind speed variation and tracks his optimal value ω_m^* which ensure the MPPT capability. Moreover, the active current i_{rq} tracks the reference value i_{rq_ref} with quick dynamic performance and without overshoots as shown in Figure 3.10.(c), the active current value increase from $i_{rq_ref} = 900A$ to $i_{rq_ref} = 2500A$ at the step beginning and return to the normal value with good control performance. The reactive current i_{rd} , is well controloed and tracks the imposed reference value $i_{rd_ref} = 0$ in order to minimize power losses (see Figure 3.10.(c)). The same for the electromagnetic torque which tracks his reference value with a good dynamic performance as shown in Figure 3.10.(d).

Table. 3.1. DFIG system parameters.

DFIG system parameters	
Rated Power	2MW
Rated speed	1500tr/min
Frequency	50Hz
Grid voltage	400V line to line
DC Bus Voltage	800V
Stator resistance and inductance	0.0026Ω , 8.7e-02mH
Rotor resistance and inductance	0.0029Ω, 2.6mH
Mutual inductance	0.0025H
Proportional constant of PI current regulator	0.5771
Integral constant of PI current regulator	491.5995

**Figure. 3.10.** DRTS of the RSC control for (a): wind speed, (b) rotor speed, (c) rotor current, (d) electromagnetic torque.

3.5 Controller Hardware-in-the-Loop Simulation for the Grid Side Converter

In this section, some tests are realised to verify the GSC proposed algorithm effectiveness by applying the HIL Simulation [49, 53]. This method uses a DRTS with various Input/Output digital signals, Digital to Analogue Converters (DAC) and Analogue to

Digital Converter (ADC), in order to simulate the power system behaviour in real-time. The platform for this study is built with the TMS320F28379D microcontroller from Texas Instruments [54], and the PLECS RT Box1 (Plexim) HIL boards with several analogues and digital Input/Outputs [55] (see Figure 3.11). The file with the C-code was created and uploaded into both targets [49], and the voltages and currents measurements are recorded in the host PC in order to monitor them as described in Figure 3.11. Tables 3.2 and 3.3 presents the power parameters for the grid side and the control subsystem parameters, respectively.

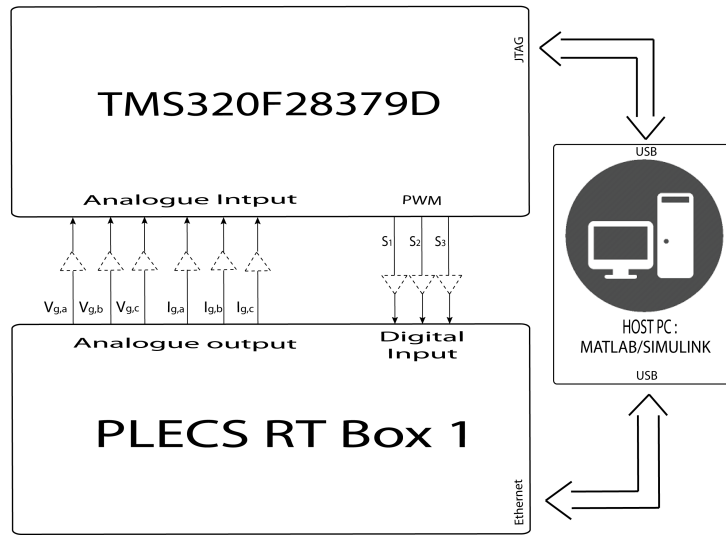


Figure. 3.11. The Grid-Side Power parameters.

Table. 3.2. The Grid-Side Power parameters.

Power parameters of the Grid-Side	
Nominal DC link voltage	VDC = 800V
Switching Frequency	fsw = 24 416Hz
Line Inductance	L = 0.15mH
AC system	Voltage amplitude VRST: 400V(rms) line-to-line Nominal frequency: 50Hz

Table. 3.3. The Grid-Side Power parameters.

Control subsystem parameters	
Constants of the PR current regulators in $\alpha\beta$ axes	$k_{p,I\alpha\beta} = 0.0011, k_{i,I\alpha\beta} = 0.1$
Resonant and cut-off frequencies	$w_o = 314.16rad/s, w_c = 1rad/s$
Constants of the PI voltage regulator	$k_{p,VDC} = 3977.5, k_{i,VDC} = 152110$
Sample time of the power and control subsystems	$T_s = 10.2392\mu s, T_{reg} = 40.957\mu s$

Four tests are assigned to deal with LVRT requirement at the three-phase output of the GSC in order to verify the strategy performance during different failure conditions.

Generally, grid codes force the wind system to still connect even when grid voltage faults happen and inject reactive power to the utility grid according to the voltage depth level, forcing a grid currents limitation to its nominal amplitude. Consequently, it will be two control modes for each test: the first mode is the control under normal conditions; meanwhile the second control mode is based on LVRT proposed strategy application, mainly activated when the grid voltage faults occur.

- Test 1: symmetrical voltage sag (0.1 pu), duration $t=0.11\text{s}$; full nominal power (Figure 3.12) and half nominal power (Figure 3.13).

Figures 3.12 and 3.13 present the GSC control strategy response to a three-phase voltage sag (0.1pu) using the PR regulators under full nominal power and half nominal power, respectively, in order to verify the limitation imposed to the output grid currents. During the faults, it seems that the three-phase grid currents do not exceed the nominal value for both cases, injecting a reactive power of 50 kVAr and zero active power into the grid according to the grid code. Thus, the system control behaviour with PR regulators dealing with the capability to inject the reactive power according to the grid code previously presented and with the limitation of three-phases grid current. Also, after the fault disappearance, the normal operation of the GSC controller is attained and the reactive power is zero for unity power factor operation.

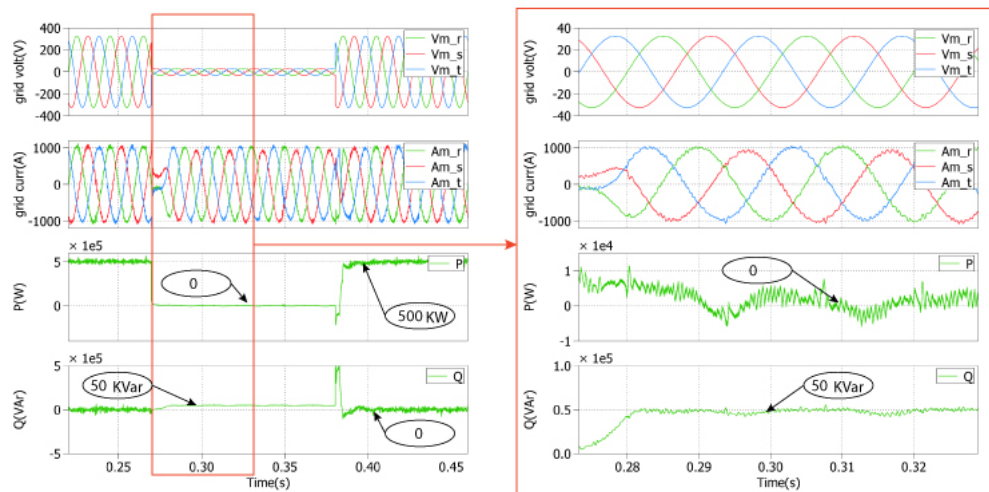


Figure. 3.12. Simulation results of the LVRT proposed strategy for symmetrical voltage sag of (0.1pu) under full nominal power.

- Test 2: symmetrical voltage deep (0.3pu), duration $t=0.11\text{s}$; full nominal power (Figure 3.14) and half nominal power (Figure 3.15).

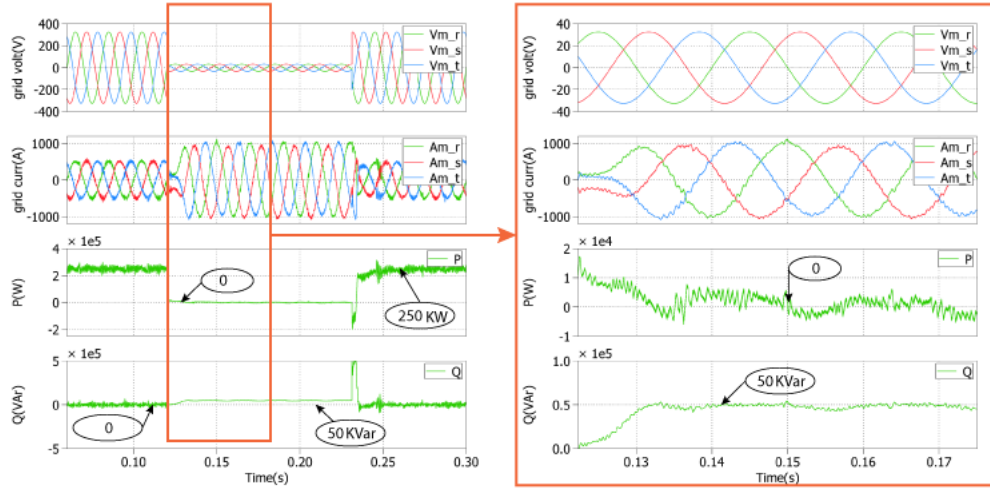


Figure. 3.13. Simulation results of the LVRT proposed strategy for symmetrical voltage sag of (0.1pu) under half nominal power.

In order to verify the capability of the proposed strategy during a deeper voltage dip, a voltage sag of 0.3pu for the same duration $t=0.11s$ is applied. Figures 3.14 and 3.15 represent the GSC control strategy response to symmetrical three-phase grid fault of 0.3pu for the proportional-resonant regulators under full nominal power and half nominal power respectively, in order to verify the current limitation. During the faults, there is no overcurrent on the three-phase output grid currents not exceeding its nominal value for both cases. Meanwhile, the active power decrease to 0 and the reactive power increases to 150kVAr. Thus, the used strategies behaviour deals with LVRT capability and injects reactive power according to the grid code. Also, when the grid fault ends, the normal operation of the GSC controller is achieved and the reactive power is zero.

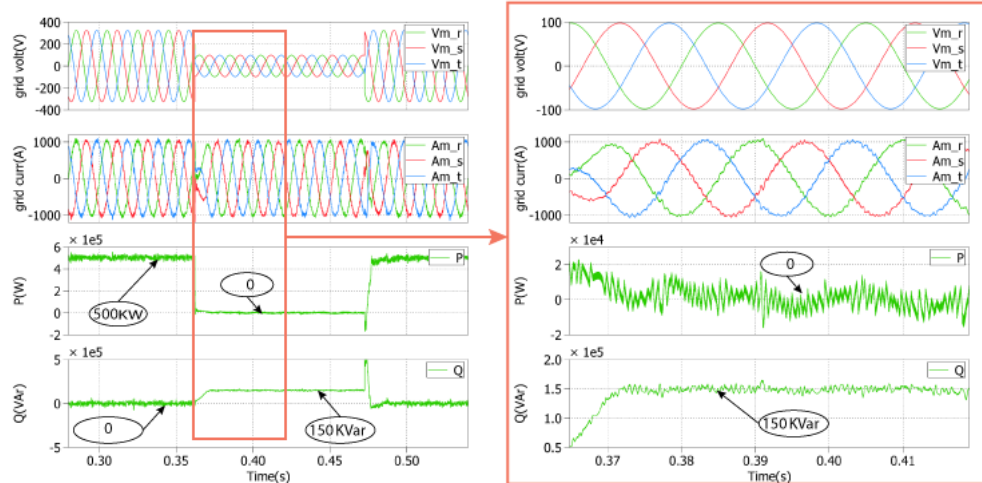


Figure. 3.14. Simulation results of the LVRT proposed strategy for symmetrical voltage sag of (0.3 pu) under full nominal power.

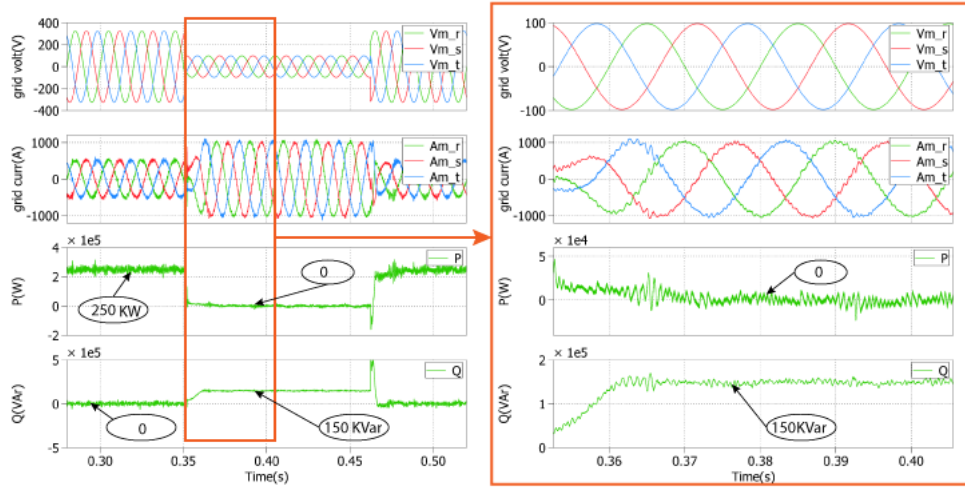


Figure. 3.15. Simulation results of the LVRT proposed strategy for symmetrical voltage sag of (0.3 pu) under half nominal power.

- Test 3: asymmetrical voltage sag (one phase) (0.1 pu), duration $t=0.25s$; full nominal power (Figure 3.16) and half nominal power (Figure 3.17).

In order to verify the proportional-resonant controller capability under unbalanced grid fault, in this case, a deep voltage sag for a duration of $t=0.27s$ in phase 3 is applied under full nominal power (Figure 3.16) and half nominal power (Figure 3.17). As shown in the Figures the three-phase grid currents do not exceed its nominal value for both cases, meanwhile, a specific quantity of active and reactive powers is injected into the utility grid. The oscillating nature of the reactive power during the unbalanced grid faults at twice the nominal frequency is due to the proper control of the negative sequence of the grid currents delivered to the grid, which also produces a constant active power control. However, the grid currents are unbalanced under this assumption. Finally, the system attains its normal operation when the unbalanced fault ends.

- Test 4: asymmetrical voltage sag (one phase) (0.5pu), duration $t=0.25s$; Full nominal power (Figure 3.18) and half nominal power (Figure 3.19).

In Figures 3.18 and 3.19, one phase voltage test in this case with the same duration of the previous test considering different level of the grid voltage fault (0.5pu), the grid currents didn't exceed its nominal amplitude value for both cases. Furthermore, because of the slight value of the voltage drop compared to the previous tests, a higher active power is injected to the grid. Again, the reactive power oscillations during the unbalanced grid faults, for constant active power control, is due to the control of the negative sequence

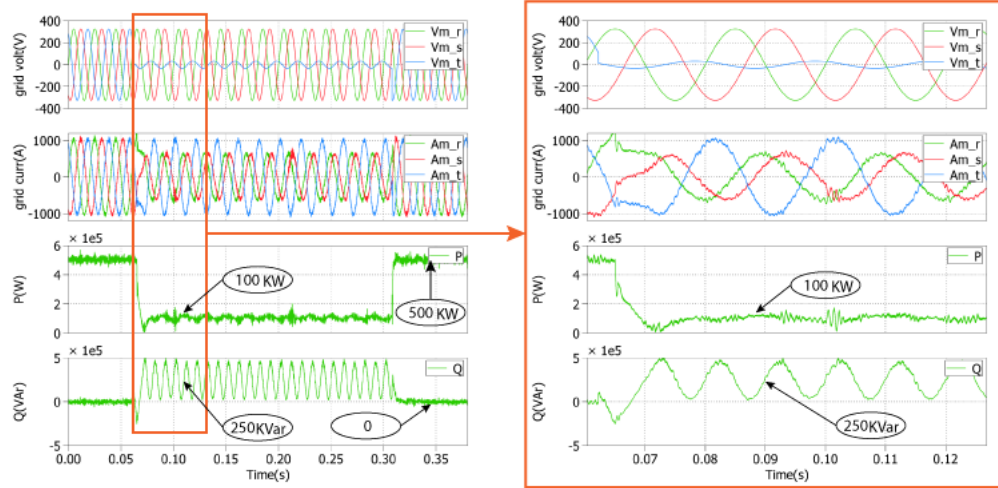


Figure. 3.16. Simulation results of the LVRT proposed strategy for asymmetrical voltage sag of (0.1 pu) under full nominal power.

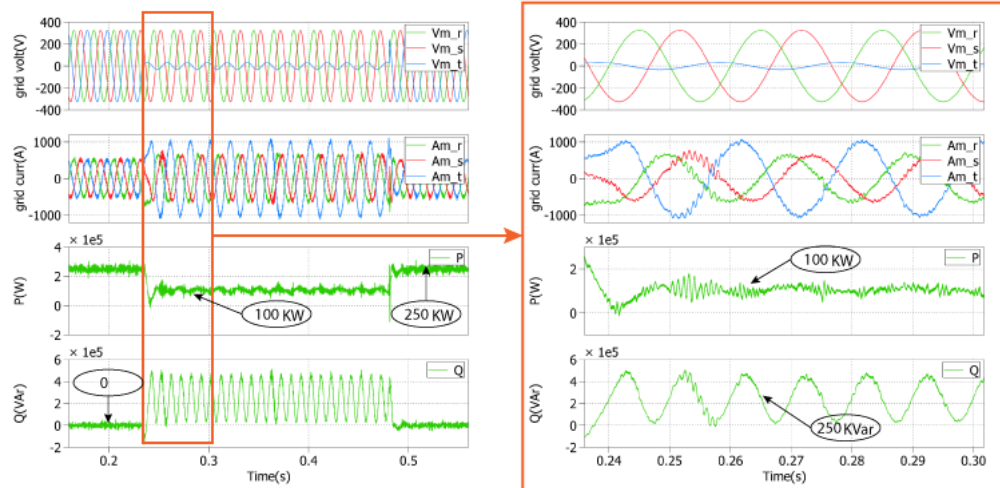


Figure. 3.17. Simulation results of the LVRT proposed strategy for asymmetrical voltage sag of (0.1pu) under half nominal power.

of the grid currents delivered to the grid; the system attains its normal operation when the unbalanced fault ends.

Finally, the GSC control strategy behaviour is dealing with the capability to inject the reactive power into the utility grid following the Spanish grid code previously presented and with the limitation of the three-phase grid currents amplitude is validated.

3.6 Conclusion

The proposed control algorithms in this work are used for a grid-connected DFIG

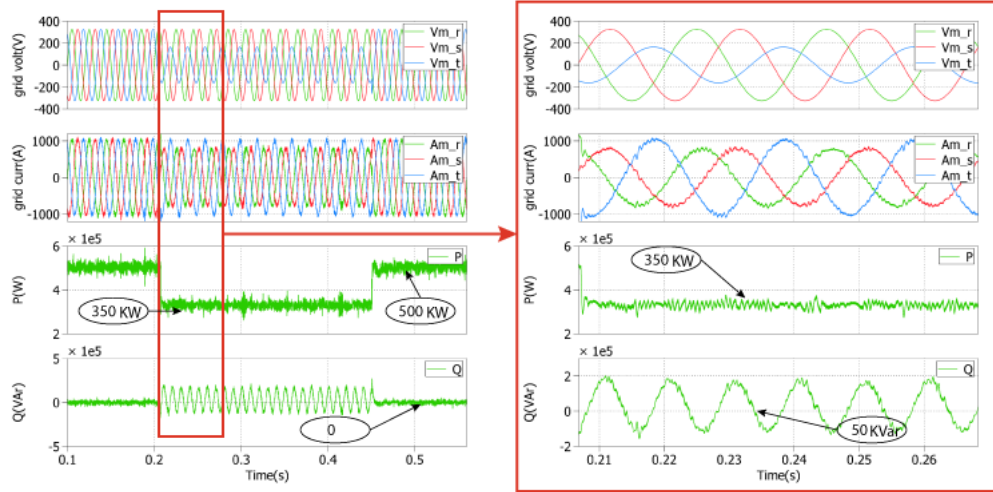


Figure. 3.18. Simulation results of the LVRT proposed strategy for asymmetrical voltage sag of (0.5pu) under full nominal power.

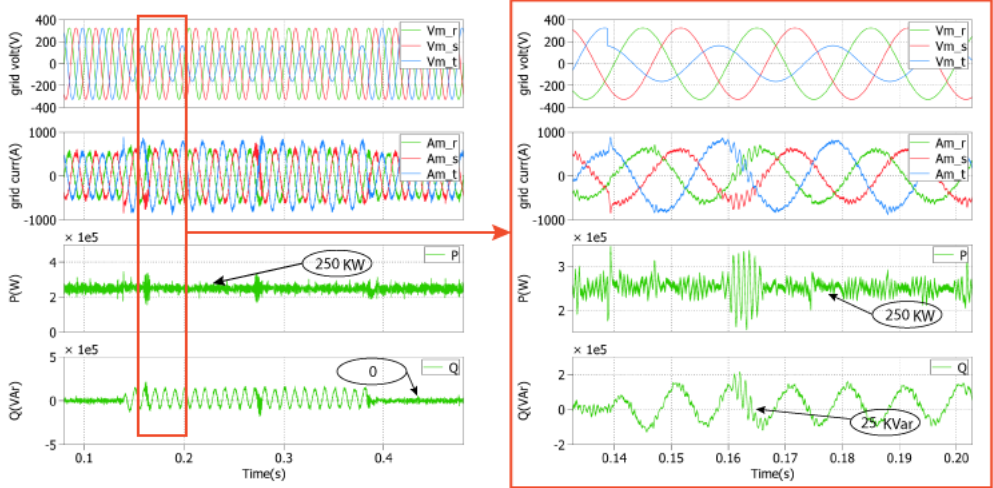


Figure. 3.19. Simulation results of the LVRT proposed strategy for asymmetrical voltage sag of (0.5pu) under half nominal power.

to improve the quality of power and to deal with LVRT requirements according to the Spanish grid code. The vector control using the stator-flux-oriented control strategy has been applied to the RSC, and the performance of this control has been verified using DRTS. Moreover, the GSC is controlled to compensate the reactive power and reduce the active power oscillations during the unbalanced grid operation. For this reason, the PR regulators have been proposed in the stationary reference frame in order to control the negative- and positive- sequences of the grid currents. The different types of grid voltage sags have been tested, and the experiments using CHIL simulation validate the proposed control algorithms for all tests, by limiting the amplitude of the grid currents,

injecting the required reactive power and stabilizing the active power transferred into the grid.

This work is published in an indexed journals: [20]

- EL KARKRI, Yassir, REY-BOUÉ, Alexis B., EL MOUSSAOUI, Hassan, et al. Improved Control of Grid-connected DFIG-based Wind Turbine using Proportional-Resonant Regulators during Unbalanced Grid. Energies, 2019, vol. 12, no 21, p. 4041.

Chapter 4

Robust Current Sensors Fault detection and reconfiguration in DFIG-DC Drives.

4.1 Introduction

The Doubly Fed Induction Generator with DC output (DFIG-DC) systems connected to microgrids are being widely studied in the current years, and they are considered as an assuring solution for the wind energy system integration [56, 57]. The principal advantages of DFIG-DC systems in microgrids are the efficiency improvement and the lower conversion stages used for production and storage units integration [58]. DFIG-DC consists of a wound rotor induction machine connected to a voltage source inverter (VSI) and a diode rectifier in the stator side, both (VSI and rectifier) connected to the DC-power system [59]. The power converter controls the rotor current in order to adjust the machine power, and the diode rectifier is the main responsible for power transfer through the stator. DFIG is usually used in the wind power conversion system, with the intention of decreasing power electronics cost while enabling high-performance control and avoiding machine instability when running with DC voltage and variable speed.

Since the DFIG control system is related to the sensor measurements, it is sure that the response of the system control can be influenced by sensor faults. Also, most of the research literature focuses on power converters faults, especially open- and short- circuit

faults, and the majority of available diagnosis methods are based on the current sensors [12, 13]. Thus, sensor faults can damage the power electronics components or even the entire system which can lead to losing the energy production unit. In fact, the development of sensor faults detection, isolation and reconfiguration are necessary to avoid the aforementioned effects and to ensure the safe operation of the energy production system. Therefore, current sensor fault diagnosis algorithms merit proper consideration from the research community all over the world.

Sensor faults diagnosis algorithms have been reviewed in the literature [16]. Shahram Karimi et al. [60] proposed a predictive model for sensor faults detection in the grid side converter of a DFIG in case of just one sensor fault. In [61] a bank of observers are performed for a DFIG in order to provide residuals for fault detection, and the system control based on vector control switched from closed- into open-loop to isolate the faulty sensors from the drive. Also, an extended Kalman filter is proposed by Gilbert Hock et al [62] for a Permanent Magnet Synchronous Generator (PMSG) but the algorithm performance declines at lower speeds and it's affected by the variation of system parameters. In [63] a low computational algorithm is proposed based just on the measured current to deal with the one sensor- and open circuit-fault diagnosis. In [64] Chakraborty and Verma propose a vector rotator to switch to the right signal from the eight estimated current in the $\alpha - \beta$ reference frame, but it is not possible to keep the safe operation when the two sensors used are faulty. Panayiotis M. Papadopoulos et al. [65] use analytical redundancy relations for each phase to design the detection and the isolation algorithm for sensor fault, while an adaptive estimation algorithm is used for fault accommodation. In [66] Yong Yu et al. propose three observers, one for each phase, the fault-tolerant control is applied to the Voltage Source Inverter (VSI) based-induction motor drives in which the results show just the algorithm performance for just one type of sensor faults and without presenting the system response. Meanwhile, in [67] Chunya Wu et al. propose three algorithms to deal with three types of sensor faults (signal loss, gain variation and zero offset), and the proposed algorithm is applied to a PMSG with field-oriented control which can deal with one- and two-sensor faults. In [68], the authors discussed and proposed fault diagnosis and tolerance strategies for electrical faults in dual three-phase PMSG, a step-method is designed to diagnose sensor faults and a current estimation based on vector space decomposition is performed to achieve fault-tolerant control. Kaishun Xiahou et al. [69, 70] used a Kalman filter for fault

detection and isolation in both the stator and rotor current sensors for DFIG systems, using stator current loop vector control instead of the conventional rotor current loop vector control strategy. In [71] and [72] a simple algorithm is used for fault-tolerant when just one sensor is faulty and just three types of fault are treated.

In this work, a novel strategy is proposed for sensor fault diagnosis based just on the measured current, the algorithm is valid for real-time implementation due to its moderate computational burden, and can deal with different sensor faults. When just one sensor fault is detected, the healthy sensors are used to compensate the faulty sensor, while, when two or all the sensors are faulty a non-linear observer proposed in [14] for a Wound Rotor Synchronous Machine (WRSM) is developed to be compatible with the studied system (DFIG-DC).

4.2 Current sensors fault diagnosis

The faulty conditions in a power generation system can be caused by different kinds of faults that can affect different components of the drive. In this work, current sensor faults are considered. The focus is on the fault detection, isolation and reconfiguration of the faulty rotor- and stator-current sensors in the DFIG-DC system. Generally, the control structure of the studied system needs current sensors located on the three phases of the rotor and stator sides. So, the performance of the controlled system is essentially dependent on the sensors that should operate correctly. In this section, a new and simple diagnosis strategy is proposed for the detection and localization of different types of sensor faults.

4.2.1 Types of current sensor faults

Sensor faults are one of the major failure sources on the controlled electrical drives and their effect can totally damage the electrical production unit, and since the studied system is based on DFIG-DC which is very sensitive to these types of faults, a fault-tolerant control is mandatory to manage with all possible types of sensor faults. In this work, five types of current sensor faults are considered in both stator and rotor windings of the DFIG-DC system: noise, out of order Broken sensor, saturation, gain error and offset. The five current sensor faults considered are listed in Table 4.1 [73].

Table. 4.1. Types of a sensor faults.

Fault types	Measured Current	Notes
Without Fault	$I \sin(\omega t)$	I : the current amplitude, ω : current frequency
Noise	$I \sin(\omega t) + n(t)$	$n(t)$: noise signal
<i>Out of order Sensor</i>	0	
<i>Saturation</i>	I_{sat}	I_{sat} : saturation value
<i>Gain error</i>	$(1 - \varepsilon)I \sin(\omega t)$	ε : gain error level
<i>Offset</i>	I_{offset}	I_{offset} : Offset value.

4.2.2 Algorithm of sensor fault detection and localization

In the main scheme of the control system, a new block related to the sensor fault diagnosis is added. It is assumed that the system works with three current sensors in the stator and rotor parts. The sensor current fault can be detected using the 3-phases balance equation :

$$|i_a + i_b + i_c| > \xi \quad (4.1)$$

i_a , i_b and i_c are the three phases current and ξ is the threshold value between normal and faulty operation. This information can prove fault apparition without identifying the exact phase where the sensor fault appears. Therefore, in this work, a new fault diagnosis algorithm is proposed to guarantee the fast and exact detection of the faulty sensor. The method is easy to implement and is based on the calculation of the difference between the present and the previous value of the normalized current in each phase:

$$\left\{ \begin{array}{l} \delta_a = \frac{1}{\sqrt{2}I_m} |i_a(k) - i_a(k-1)| \\ \delta_b = \frac{1}{\sqrt{2}I_m} |i_b(k) - i_b(k-1)| \\ \delta_c = \frac{1}{\sqrt{2}I_m} |i_c(k) - i_c(k-1)| \end{array} \right. \quad (4.2)$$

Where I_m being the rated current When the sensor fault happens, it is easy to detect the change on each phase based on the information coming from the Diagnosis Variables δ_a , δ_b and δ_c . An abnormal change in each phase can be detected by comparing each diagnosis variable by a threshold which depends to the rated current value: if the diagnosis variable is lower than the chosen threshold, then no fault is detected and the fault

index still equals to zero, else if one of the diagnosis variables becomes higher than the chosen threshold, the fault index changes to 1:

$$\begin{cases} \text{if } (\delta_{(a,b,c)} \leq Thr) \text{ then } F_{a,b,c} = 0; \\ \text{elseif } (\delta_{(a,b,c)} > Thr) \text{ then } F_{a,b,c} = 1; \end{cases} \quad (4.3)$$

where Thr is the chosen threshold, and F_i is the fault index. In this study, $Thr = 2/\sqrt{2}I_m$. The proposed fault diagnosis algorithm is valid for all types of sensor fault except for the lower values of gain error when the generator operates on lower values of torque. In fact, to ensure the safe operation for this situation, the same algorithm is used with just one configuration on the diagnosis variables instead of using the present and the previous value of each phase, and the mean rate of the difference between the measured and the observed current is applied:

$$\begin{cases} \Delta_a = \text{mean}(|i_a - \hat{i}_a|) \\ \Delta_b = \text{mean}(|i_b - \hat{i}_b|) \\ \Delta_c = \text{mean}(|i_c - \hat{i}_c|) \end{cases} \quad (4.4)$$

This algorithm works well and can detect the sensor fault for the previously mentioned case but in the other cases, it remains slow due to the use of a moving average ‘mean’.

4.3 Fault-Tolerant Control

In this section, the fault-tolerant control for one sensor fault is explained using the two healthy sensors. In addition, when two sensors are faulty at the same time, a nonlinear observer is used for the rotor and the stator currents, and the fault index signals generated by the proposed diagnosis algorithm are used to switch from faulty current signals to the observed current.

4.3.1 Fault tolerance with one sensor fault

In the case when just one sensor fault is detected and well localized, the fault reconfiguration block receives the fault index signals from the diagnosis block to compensate the

faulty current sensor using the two other healthy sensors (Kirchhoff's current law) in order to generate the currents applied to the DFIG-DC control system $i_{a,app}$, $i_{b,app}$ and $i_{c,app}$. One sensor fault reconfiguration principle is represented in Fig.4.1.

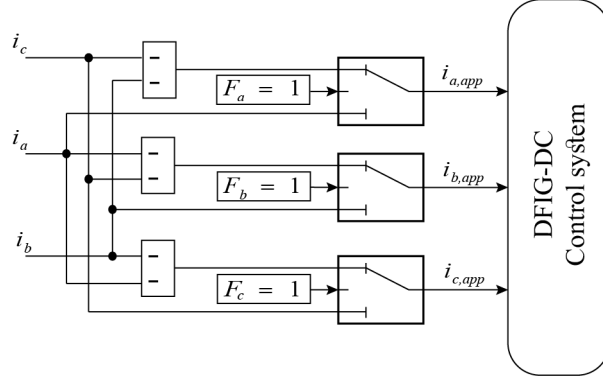


Figure. 4.1. One sensor Fault reconfiguration block.

Fig.4.2 presents the flowchart of the proposed diagnosis algorithm.

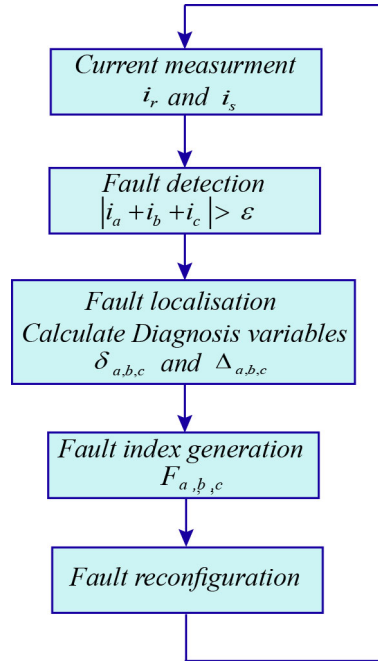


Figure. 4.2. Flowchart of the proposed sensor fault diagnosis algorithm.

4.3.2 One sensor Fault reconfiguration block

This part deals with the current observation and two sensor fault detection and isolation. In this case, the three current must be reconstructed, and a non-linear observer which proposed in [14] for WRSM is applied to our system.

The DFIG model in the rotor reference frame is given by:

$$\begin{bmatrix} \dot{i}_{ds} \\ \dot{i}_{qs} \\ \dot{i}_{\alpha r} \\ \dot{i}_{\beta r} \end{bmatrix} = \begin{bmatrix} \frac{L_r R_s}{\sigma} & \frac{L_r L_s \omega_r}{-\sigma} & \frac{L_m R_r}{-\sigma} & \frac{L_m L_r \omega_r}{-\sigma} \\ \frac{L_r L_s \omega_r}{\sigma} & \frac{L_r R_s}{\sigma} & \frac{L_m L_r \omega_r}{\sigma} & \frac{L_m L_r}{-\sigma} \\ \frac{L_m R_s}{-\sigma} & \frac{L_m L_s \omega_r}{\sigma} & \frac{L_s R_r}{\sigma} & \frac{L_m^2 \omega_r}{\sigma} \\ \frac{L_m L_s \omega_r}{-\sigma} & \frac{L_m R_s}{-\sigma} & \frac{L_s^2 \omega_r}{-\sigma} & \frac{L_s R_r}{\sigma} \end{bmatrix} \begin{bmatrix} i_{ds} \\ i_{qs} \\ i_{\alpha r} \\ i_{\beta r} \end{bmatrix} + \begin{bmatrix} \frac{L_r}{-\sigma} & 0 & \frac{L_m}{\sigma} & 0 \\ 0 & \frac{L_r}{-\sigma} & 0 & \frac{L_m}{\sigma} \\ \frac{L_m}{\sigma} & 0 & \frac{L_s}{-\sigma} & 0 \\ 0 & \frac{L_m}{\sigma} & 0 & \frac{L_s}{-\sigma} \end{bmatrix} \quad (4.5)$$

where L_m , L_s and L_r are mutual, stator and rotor inductance, ω_r is the rotor electric angular speed, and $\sigma = 1/(L_m^2 - L_s L_r)$. As mentioned before, the stator and rotor currents have to be estimated. Thus, two observers are applied, one to estimate the rotor currents using the measured stator current, and the second to estimate the stator current basing on the measured rotor currents. The state-space model of the used observer can be presented as follows:

$$\begin{cases} \dot{x} = A_x x + B_x u + Gy \\ \dot{y} = A_y x + B_y u + Hy \end{cases} \quad (4.6)$$

where x and y are the measured and the estimated variables respectively, u is the control vector. Matrix A_x , A_y , B_x , B_y , G and H are defined for each current observer. By applying the proposed Observer in [14] on the system presented by equation (5), x and y are replaced by the stator and rotor current depend on the used observer. The used Observers are presented as:

- Rotor current Observer

$$\begin{cases} \dot{\hat{i}}_s = A_s i_s + B_m u_r + B_s u_s + G_r \hat{i}_r + K_r \xi_s \\ \dot{\hat{i}}_r = A_{rs} i_s + B_r u_r + B_m u_s + H_r \hat{i}_r + N_r \xi_s \end{cases} \quad (4.7)$$

- Stator current Observer

$$\begin{cases} \dot{\hat{i}}_r = A_r i_r + B_r u_r + B_m u_s + G_s \hat{i}_s + K_s \xi_r \\ \dot{\hat{i}}_s = A_{sr} i_r + B_m u_r + B_s u_s + H_s \hat{i}_s + N_s \xi_r \end{cases} \quad (4.8)$$

with : $i_s = \begin{bmatrix} i_{ds} \\ i_{qs} \end{bmatrix}$ and $i_r = \begin{bmatrix} i_{\alpha r} \\ i_{\beta r} \end{bmatrix}$ are the state variables, //

$u_s = \begin{bmatrix} u_{ds} \\ u_{qs} \end{bmatrix}$ and $u_r = \begin{bmatrix} u_{\alpha r} \\ u_{\beta r} \end{bmatrix}$ are the control variables,

$\xi_s = i_s - \hat{i}_s$ and $\xi_r = i_r - \hat{i}_r$ are the errors between the measured and the estimated stator and rotor currents respectively. The system matrices are defined as follow:

$$A_s = H_s = \begin{bmatrix} \frac{L_r R_s}{\sigma} & \frac{L_r L_s \omega_r}{-\sigma} \\ \frac{L_r L_s \omega_r}{\sigma} & \frac{L_r R_s}{\sigma} \end{bmatrix}, A_r = H_r = \begin{bmatrix} \frac{L_s R_r}{\sigma} & \frac{L_m^2 \omega_r}{\sigma} \\ \frac{L_m^2 \omega_r}{-\sigma} & \frac{L_s R_r}{\sigma} \end{bmatrix}, B_r = \begin{bmatrix} \frac{L_s}{-\sigma} & 0 \\ 0 & \frac{L_s}{-\sigma} \end{bmatrix};$$

$$B_s = \begin{bmatrix} \frac{L_r}{-\sigma} & 0 \\ 0 & \frac{L_r}{-\sigma} \end{bmatrix}; B_m = \begin{bmatrix} \frac{L_m}{\sigma} & 0 \\ 0 & \frac{L_m}{\sigma} \end{bmatrix}; A_{sr} = G_r = \begin{bmatrix} \frac{L_m R_s}{-\sigma} & \frac{L_m L_s \omega_r}{\sigma} \\ \frac{L_m L_s \omega_r}{-\sigma} & \frac{L_m R_s}{-\sigma} \end{bmatrix}; A_{rs} =$$

$$G_s = \begin{bmatrix} \frac{L_m R_r}{-\sigma} & \frac{L_m L_r \omega_r}{-\sigma} \\ \frac{L_m L_r \omega_r}{\sigma} & \frac{L_m L_r}{-\sigma} \end{bmatrix}$$

In order to ensure the convergence conditions and the system stability [14], N_r and N_s are chosen to be equal to the transpose matrix of G_r and G_s respectively, and K has to be positive definite:

$$\begin{cases} N_r = G_r^T \\ N_s = G_s^T \\ K > 0 \end{cases} \quad (4.9)$$

When the sensor fault appears in two phases, a 2-fault index (2F) signal is generated by the two sensor fault diagnosis block and used to switch the current applied to the control system from measured to observed. Two sensors fault reconfiguration principle is represented in Fig.4.3.

4.4 Experimental Results

In this study, the system used is based on a 4 kW GFIG-DC. Two autotransformers are used, one is connected between the three-phase stator windings and the rectifier in order to adapt the stator voltage with the rotor voltage, the second one is used to feed the DC-bus through a three-phase diode bridge. The generated power is dissipated through a DC-load which is dimensioned to be able to dissipate all the active power generated

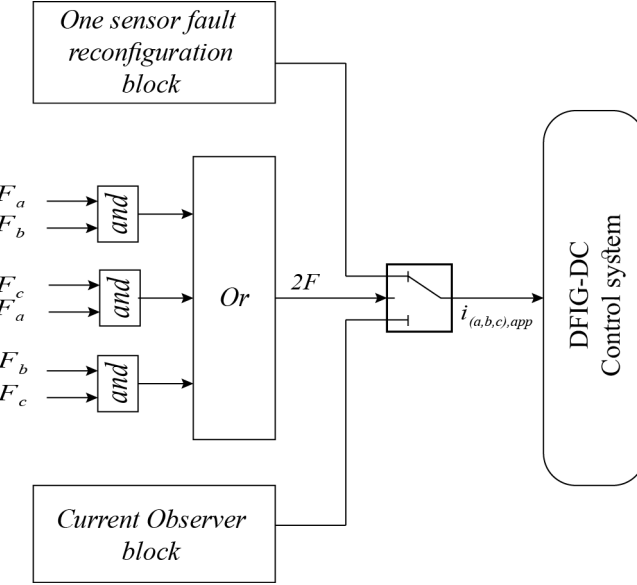


Figure. 4.3. Two sensor fault reconfiguration principle.

by the system. The rotor windings are supplied by a two-level voltage inverter which is fed by the DC-bus. In fact, an additional inductance must be connected between the three-phase rotor windings and the voltage inverter in order to protect the rotor winding insulation system. The DFIG is driven by a 7.5 kW induction motor which has the ability to be controlled by torque or speed regulation. In addition, an encoder with 2048 ppr is coupled with the induction motor to measure the rotor position. The control system implementation is performed using the dSPACE 1103 controller board and the Control Desk digital platform, with 90 μ s as the system sampling time.

Several experimental tests are performed to evaluate the performance of the proposed algorithm for fault detection and reconfiguration at stator and rotor current sensor for different operating conditions and different types of sensor faults.

4.4.1 Fault-tolerant for one sensor fault

In this part, five experiment tests are realized to verify the performance of the proposed algorithm for sensor fault diagnosis and fault-tolerant for the defined sensor's fault in both the stator and rotor current. with a rotor speed of 1350 tr/min and a reference torque of -12.5 N.m.

In Fig.4.4, a noise signal is applied to the first phase (phase a) of the measured rotor current at $t=0.5$ s, it can be seen that the diagnosis variable for phase (a) exceed the

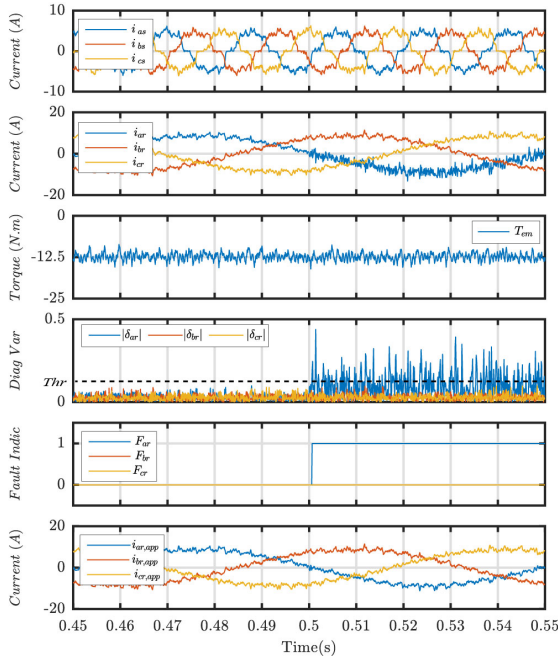


Figure. 4.4. Simulation results obtained in the case when a noise signal occurs in phase ‘a’ of the rotor current sensor.

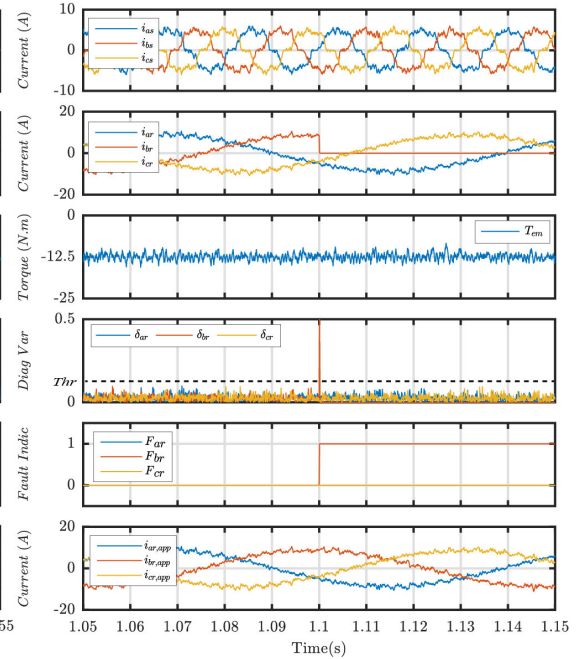


Figure. 4.5. Simulation results obtained in the case when the sensor in phase ‘b’ of the rotor current is completely out of order.

fixed threshold Thr , and as a result, the fault index for phase (a) ‘ F_{ar} ’ turns from 0 into 1 indicating that the fault is well detected and localized. Thus, the current in this phase can be replaced by the difference between the other two healthy phases (phase (a) and (b)). It seems clear that the new rotor current applied to the control system is well reformed, and the electromagnetic torque still at the same state before the fault appearance. In fact, due to the fast response of the proposed fault diagnosis, the fault can’t affect the measured stator current which is still unchanged during the faulty period. Fig.4.5 and Fig.4.6 show the same performance for the proposed algorithm when the rotor current sensor in phase (b) is totally out of order at $t=1.1$ s as represented in Fig.4.5, and during the saturation $I_{sat} = 6A$ in phase (c) at $t=1.7$ s as represented in Fig.4.6.

Fig.4.7 shows the system response when an offset of 3A appears in the second phase of the stator current (phase (b)) at $t=1.1$ s. The sensor fault is well detected and localized, the same performance is achieved when stator current sensor fault appears, the fault index for phase (b) ‘ F_{bs} ’ turns from 0 into 1 and the system recovered the normal operation quickly. Generally, the diagnosis time (time between fault appearance and detection) can take a max of 8Ts for all mentioned types of sensor faults.

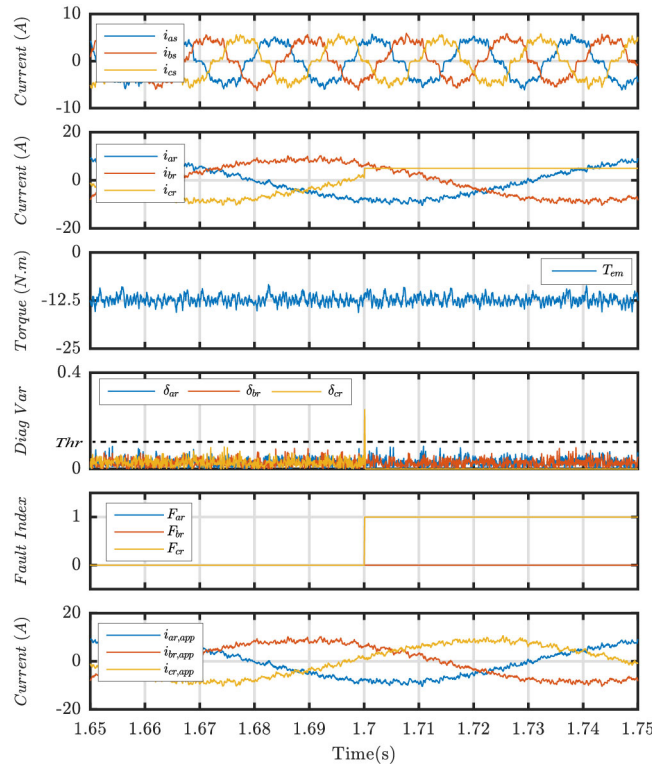


Figure. 4.6. Simulation results obtained in the case when the sensor in phase ‘c’ of the rotor current is saturated.

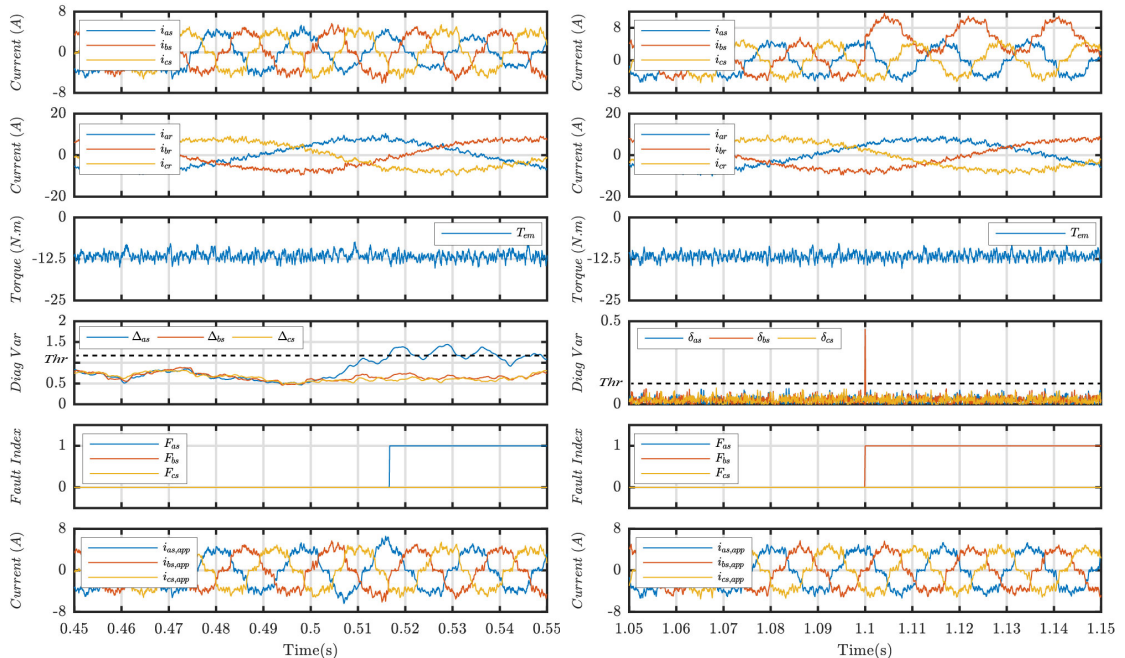


Figure. 4.7. Simulation results obtained in the case when a gain error occurs in phase ‘a’ of the stator current sensor.

Figure. 4.8. Simulation results obtained in the case when an offset signal occurs in phase ‘b’ of the stator current sensor.

In Fig.4.8, a gain-error of -30% appears in phase (a) of the stator current at $t=0.5$ s. In this case, the proposed algorithm cannot detect the small change on the current quickly, thus, the second mechanism is applied using the observed current. For weak sensor faults, fault detection operation can take more time compared with strong sensor faults, as represented in Fig. 8, the diagnosis variable can exceed the fixed threshold after 0.016 s. and as a result, the fault index for phase (a) ' F_{as} ' turns from 0 into 1 indicating that the fault is well detected and localized. The small disturbance that appears on the stator current between the fault appearance and fault detection cannot affect the system stability, the rotor current and the electromagnetic torque are still operating normally, and the first phase of stator current is well recovered after fault detection.

4.4.2 Fault-tolerant for two sensor faults

In this part, two experiment tests are realized to verify the performance of the proposed algorithm for sensor fault diagnosis and fault-tolerant when the system operates in synchronous speed 1520 tr/min (DC-current in rotor windings) and a reference torque of -12.5N.m .

Fig.4.9 shows the experimental results when two sensor faults appear at the same time in phases (a) and (b) of the stator current; a noise fault and zero signal (out of order sensor) are applied to phase (a) and (b) respectively at the same time $t=0.5$ s. It can be seen that the diagnosis variable for phase (a) and (b) δ_{as} and δ_{bs} can exceed the fixed threshold Thr , and as a result, the fault index for 2 sensor fault ' $2F_s$ ' turns from 0 into 1 indicating that the fault is well detected and localized. Thus, the stator current, in this case, can be replaced by the observed stator current.

In Fig.4.10, the same experiment is applied to the rotor current. It seems clear that the new rotor current coming from the observer and applied to the control system is well reformed, and the electromagnetic torque is still at the same state before the fault appearance. In fact, due to the fast response of the proposed fault diagnosis, the fault cannot affect the measured stator current which is still unchanged during the faulty period.

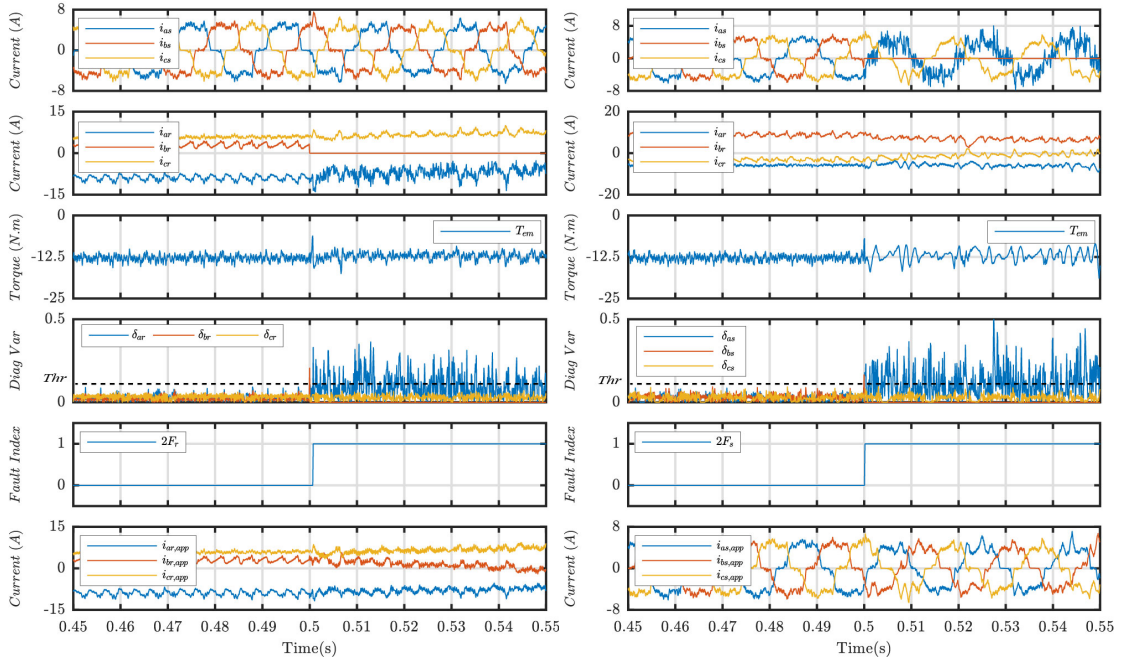


Figure. 4.9. Simulation results obtained in the case when two sensor faults occur in phase ‘a’ and ‘b’ of the stator current.

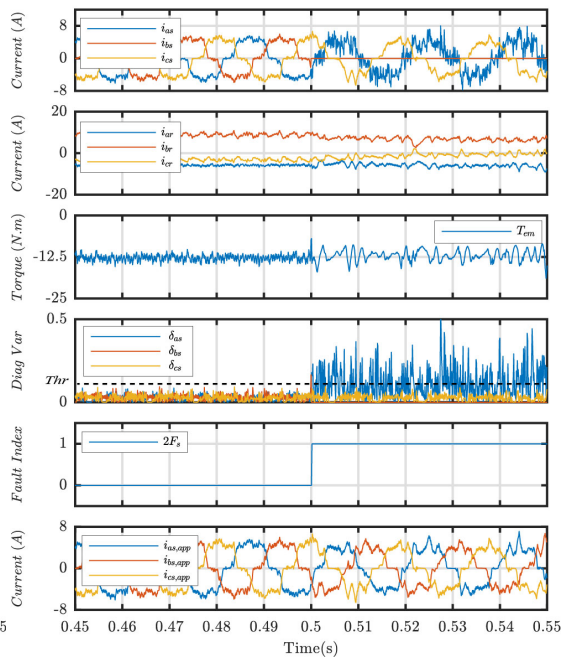


Figure. 4.10. Simulation results obtained in the case when two sensor faults occur in phase ‘a’ and ‘b’ of the rotor current.

4.5 Conclusion

This work introduces a robust and fast diagnosis and fault-tolerant algorithm for DFIG-DC drives. The predictive torque control is applied to the control system. The fault diagnosis has been proposed to be able to detect quickly all types of sensor faults, the proposed algorithm is based just on the measured current, with an exception when lower gain error fault appears, the observed current is used with the measured current in order to ensure the safe and normal system operation. Furthermore, the fault-tolerant strategy is devised based on the fault-index generated by the diagnosis algorithm; when just one sensor is faulty, the healthy sensors are used to recover the faulty one, and when more than one sensor is faulty, the observed currents are used to replace the faulty signals coming from the measurement. Moreover, the robustness of the proposed algorithm has been experimented by different tests, which confirm that the proposed scheme is independent of the DFIG parameters and the operation mode, and all the mentioned sensor faults can be identified and tolerated accurately.

This work is submitted in “IEEE TRANSACTIONS ON INDUSTRIAL ELECTRONICS”

Chapter 5

Assessment of wind power capacity credit in Morocco: Outlook to 2020

5.1 Introduction

As part of its energy strategy, Morocco undertakes a vast wind energy program, to support the development of renewable energy and energy efficiency in the country. As a result, a very ambitious program for the development of these renewable energies has recently been adopted by the Moroccan government. Also, Morocco has an important wind resource with regions exceeding 10 m/s for the average annual wind speed (Figure 5.1), in particular:

- The average annual speeds in towns of Essaouira, Tangier, and Tetouan are between 9.5 and 11 m/s.
- Tarfaya, Taza, and Dakhla are the towns with average annual speeds between 7.5 m/s and 9.5 m/s.

A first wind map of the country showed that the northern zone (Tangier to Tetouan) and the coastal strip from Tarfaya to Lagouira present exceptional sites with regular winds and average speeds sufficient to develop profitable projects. Thus, the Moroccan

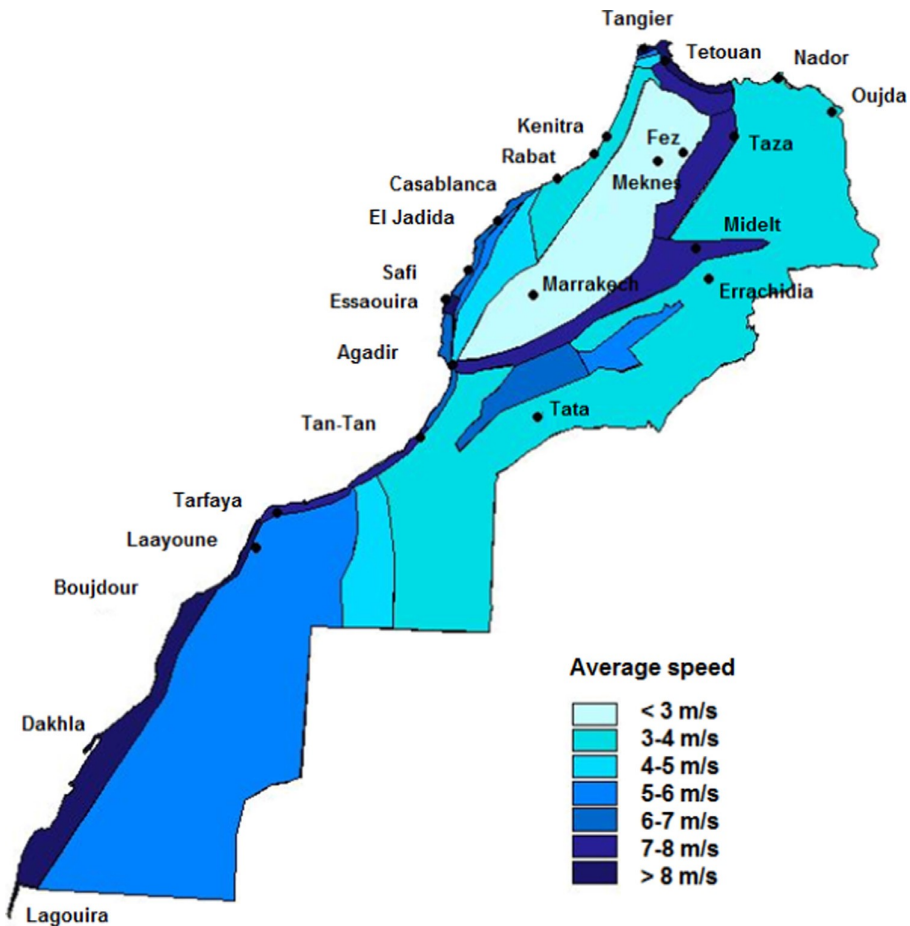


Figure. 5.1. Map of the average wind speed in Morocco (m/s) [74].

Integrated Wind Energy Project (IEP), spanning a period of 10 years for a total investment estimated at 31.5 billion Moroccan dirhams, will enable the country to increase the installed wind power capacity from 280 MW in 2010 to 2000 MW in 2020. The goal of Moroccan IEP is to install 1600 MW of new wind farms in 2020 as follows [74, 75]

- 600 MW under development: Tarfaya (300 MW), Akhfennir (200 MW), Bab El Oued (50 MW), and Haouma (50 MW);
- 1,000 MW planned on five new sites chosen for their great potential: Tangier 2 (150 MW), Koudia El Baida in Tetouan (300 MW), Taza (150 MW), Tiskrad in Laayoune (300 MW), and Boujdour (100 MW) [75, 76].

The objectives of the Moroccan IEP are not only to ensure customer satisfaction but also to protect the environment. They can be listed as follows:

- Increase the share of wind energy in the total power capacity to 14% in 2020;

- Achieve a production capacity of 2 GW from wind power and an annual production capacity of 6600 GWh, corresponding to 26% of the current electricity production [75, 76];
- Save 1.5 million tons of oil annually, and avoiding the emission of 5.6 million tons of CO₂ per year. This represents a no less committed to the fight against global warming [76–78].

With a large capacity of wind energy that will be injected into the national grid, a particular importance must be attached to the impact of this insertion on the safe operation of the electrical system. In addition and since we are interested in wind power, some constraints are worth mentioning [79]:

- The wind blows when it wants.
- The wind blows as it wants; it is difficult to predict its exact intensity.
- The wind blows where it wants and, unfortunately, it does not blow when we need a lot of electricity.

Therefore, the fact that electrical energy cannot be stored, the grid must be balanced to the nearest second [79, 80]. Thus, the large-scale integration of wind energy constitutes a major challenge for the electrical system because it is difficult to stop accurate predictions of energy production. The uncertain nature of wind generation could also have an impact on the safe operation of the system. The operation reliability is considered in this case as the ability of the system to cope with the multiple risks that could disrupt its operation.

In light of all this, a study on the long-term impact of wind power production is necessary. To which level, in terms of capacity and flexibility, can wind power replace conventional power plants? To answer this question, we will use the concept of wind capacity credit (CC). The wind CC measures the ability of wind plants to replace conventional production capacity in a given system [81, 82]. This definition may seem incomplete because it doesn't include the impact of wind generation on the system reliability. For this reason, we take the proposed definition by [83], which adding the influence of the intermittency of this energy on the system reliability. Thus, it is possible to define CC as the potential

of wind farms to replace conventional plants without endangering the system or degrading reliability. For CC calculation, two approaches are commonly used: chronological methods [81] and probabilistic methods [81–84]; the results show that the chronological approach can be very useful for the grid operator, while the probabilistic approach is especially useful for grid planning. The chronological methods provide information on the capacity of wind resources to cover peak demand, while the probabilistic methods provide information on the expected CC, obtained through statistical calculations. Therefore, the aim of this work is to analyze the impact of the wind farms in the safety of the electrical system in accordance with an injection scenario of high wind energy. First, we will study the reliability of Moroccan electrical grid in presence of TAZA wind farm with an installed power of 150 MW and after, we will generalize this study on all wind farms that will be injected to national grid in 2020. This work is structured as follows: In the second section, the production system reliability in the presence of wind energy is represented. In the third section, the CC calculation with the probabilistic model proposed is analyzed. In the fourth section, the calculation model of wind CC is applied to TAZA wind park. The fifth section presents a generalization on the analysis of CC for wind capacities installed on the national grid by 2020. Finally, the conclusion is summarized in the sixth section.

5.2 The reliability of production systems in the presence of wind

The goal of an electrical system is twofold. First, it consists in satisfying the demand at a reasonable cost and ensures with safety the continuity and the quality of service [85]. Moreover, the determination of a safety criterion is a regular part of the operational reliability studies, namely the reliability of the electrical grid. Therefore, reliability refers to the ability of a system to perform a required function; in the case of the electrical grid, the primary function is the supply of electricity from the power plants to the final consumer [86, 87]. Moreover, the ability of a system to meet the conditions established in the production system is quantified by various criteria called “reliability indices.” In the scientific literature, two methods are mainly mentioned (analytic approach and simulation approach). The analytical approach is the most used in the planning of the

electric grid because it has fewer computer constraints and it is faster during its running. Thus, analytic approach will be adopted for this study.

5.2.1 The CC analysis

The analytical approach that can be used to evaluate the adequacy of a particular production system is composed of three parts as shown in Figure 5.2. In addition, the combination of the production and load model through a risk model makes it possible to determine the safety degree of a particular system. Also, the determination of the risk model consists in calculating the reliability index for covering the total demand of the electrical system. Indeed, reliability calculations are based on the calculation of probabilistic indicators at the time of peak demand. These indicators indicate the level of loss of production to cover the demand [88–90]. Furthermore, the most failure criterion used for the production planning and future capacities for the electrical system is the LOLE (loss of load expectation) index [90]. It can be described as the expected number of hours of failure during which the peak demand can exceed the available generation capacity. This indicator also gives the number of hours during which the load loss can occur [91].

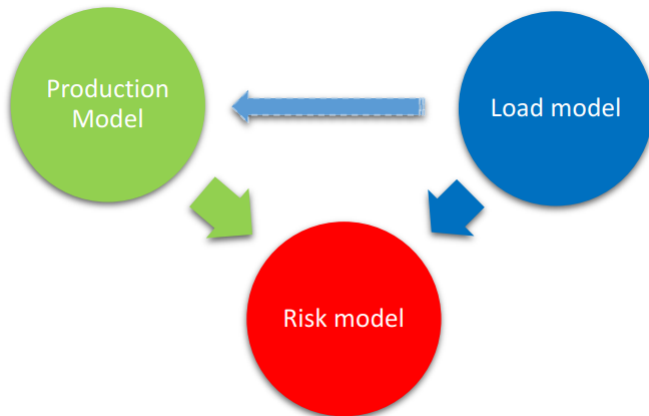


Figure. 5.2. Evaluation model of the adequacy of the electricity production systems.

In our study, in order to determine the wind CC we will model the electrical system in a probabilistic way. The probabilistic model of an electrical system must make it possible to describe the behavior of the uncertain variables of the system and the correlations between these uncertainties (Figure 5.3). Thus, the input parameters of the probabilistic model of the electrical system as we define it give way to a set of probability distributions, each probability characterizing the variation of a parameter [92].

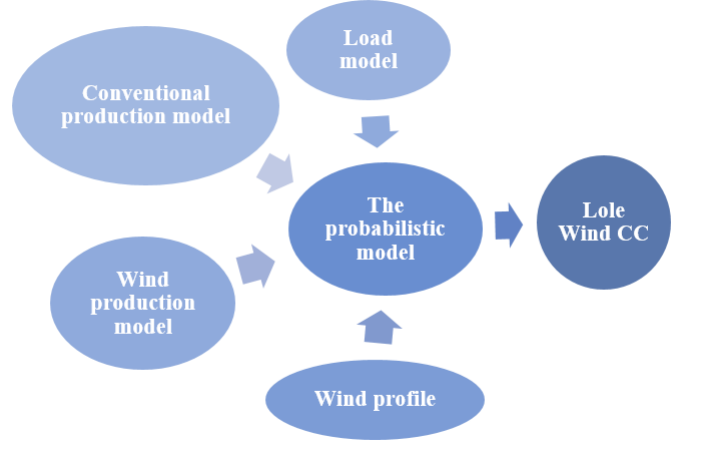


Figure. 5.3. The probabilistic model for wind CC analysis.

The proposed wind CC determination algorithm presented in Figure 5.3 receives as inputs the characteristics of the electrical system:

- The conventional production units and their default rates;
- The system consumption data;
- The wind profile of the site on which the wind turbines will be installed;
- The power curve of the wind turbines that will be installed.

The wind CC will be determined after a comparative study of the reliability of the system without and with the presence of wind energy production. The wind CC analysis is done according to the criterion of replacement of the conventional production; this means that a unit A of capacity X MW will be removed from the system. The objective is to estimate the minimum capacity of wind power to be installed by keeping the same level of reliability.

The explanation in parametric form is as follows: When an X MW capacity is removed from the system, the safety rates $\tau_{original}$ or the LOLE is affected. The new security rate τ_X will meet the requirements of the system and cover the demand. We are therefore looking for the wind capacity K_n which can be installed to reach $\tau_{original}$. Consequently, the credit of capacity can be calculated by the following expression:

$$CC = X/K_n \times 100\% \quad (5.1)$$

In order to automate this computation which is expensive, we will implement the algorithm proposed by [21] (Figure 5.4).

5.2.2 Conventional production model

The model of the production system is defined as the sets of power generation Units available in a production park. Each unit is characterized by its failure rate. The unavailability rate (forced outage rate (FOR)) is the probability that a unit will be unavailable at a given time.

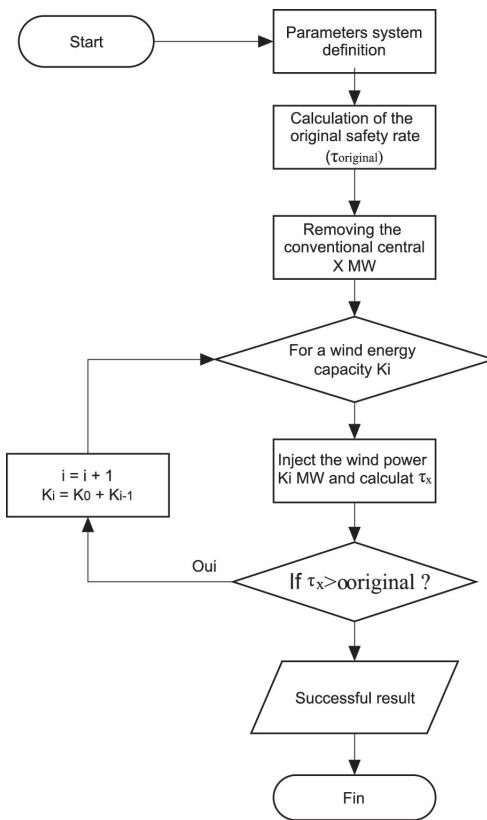


Figure. 5.4. CC determination algorithm.

At the end of 2016, Morocco's national production plant, with an installed capacity of 11,278 MW, is composed of thermal, hydraulic, interconnection plants, and also the local production of certain dealers. The details of the park and the FOR are given in Table 5.1. The installed capacity increased to 12,813 MW at the end of December 2017 and to 12,983 MW at the end of December 2018 against 11,278 MW in 2016, an increase of 15.11% due to the commissioning of the two coal groups of Safi ($2 \times 660\text{MW}$), Jerada coal group (350 MW) followed by the decommissioning of the existing power plant groups

(−135 MW) in 2017, and the commissioning of the M’dez and El Menzel hydropower plants (170 MW) in 2018 [75].

Table. 5.1. Power installed on the national power grid ([21]).

Power stations	Installed capacity (MW)	FOR
Hydraulic plants	1306	0.01
Pumped-storage	464	0.01
Coal	4146	0.04
Fuel oil	600	0.05
Gas-turbine	1230	0.02
Combined cycle	850	0.04
Diesel thermal	202	0.1
Nuclear	2480	0.12
Total national network	11,278	

5.2.3 Load model

The load model is acquired with the construction of the monotone consumption for a given period corresponding to 1 year (8760 h or 365 days; Figure 5.5). To construct the monotone of consumption or the cumulative model of load, it is necessary to have the information of the hourly or daily consumption of the system which we will have to classify in descending order, and then we can be able to calculate the weight of each state of consumption. In the medium term, demand forecasts mainly reflect the needs of industrial customers and private electricity distribution companies in the main cities of the country. These forecasts also cover the assessment of the distribution market in Morocco, which mainly corresponds to rural areas. Thus, the expected growth rate for 2010–2013 is about 6%. Moreover, the evolution of electricity consumption results from the combination of factors from different reasons: economic activity, demography, user behavior, technical progress, development of new uses of electricity, market shares between energy sources, energy control actions, and so on. The basic scenario, relying mainly on economic reforms, focuses on an evolution of 5.82% over the period 2015–2020. This emerging scenario, used as the reference scenario for the development of the Moroccan grid equipment plan, translates a 6% long-term growth [22].

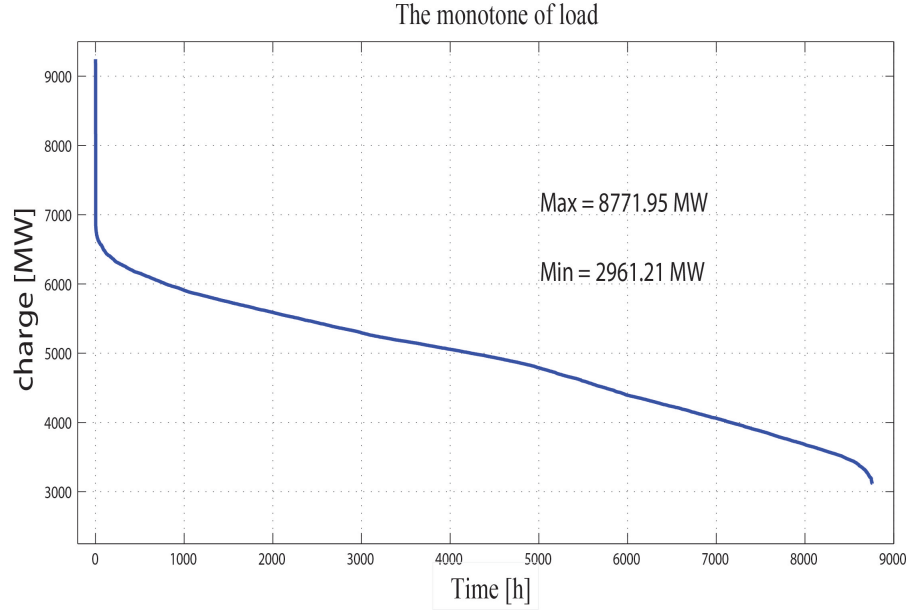


Figure. 5.5. The monotone of load in 2020.

5.2.4 Probabilistic model (risk model)

Once the production and load models are founded, a convolution of these two models is necessary for the risk model establishment that quantifies the risk of the system. This method leads to a possible determination of the reliability indices, which is the risk of loss of load mentioned above. In this study, we will work with the LOLE index, which is the mathematical expectation of failure hours (the number of hours per year during which the available production resource is not sufficient to cover the entire demand) [93]. This index can be represented as follows:

$$LOLE = \sum_{i=1}^n P_i(C_i - L_i) \quad (5.2)$$

where C_i denotes capacity available for day i , L_i denotes consumption forecast for day i , and P_i is the probability of loss of load for day i .

The LOLE is the most widely used index for determining the production capacities required in the medium- and longterm horizons. The reliability level of the national park is determined after the running the MATLAB program; this helps us to calculate the LOLE reliability index, as presented in this chapter. Table 5.2 shows the result obtained after program simulation on the Moroccan National Grid (MNG).

Table. 5.2. MNG reliability level.

System	LOLE (simulated)
MNG	0.0413 (h/year)

5.3 Application to the TAZA wind farm

5.3.1 Wind production model for the TAZA Park

First, it is necessary to create the unavailability table of the intermittent production. Then, the unavailability of the intermittent production model must be integrated into the unavailability table of the conventional production model. This subsequently allows the convolution between the production model and the cumulative load model to be made, and also to determine the risk level of the system. The safety studies in [94, 95] present an approach using a specific time series model called “Auto-regressive moving average” to predict a series of wind speed data in a particular region. This approach is difficult to implement if the access to a complete database of wind speed of a particular site is impossible. In our study, we choose to model the distribution of wind by the normal distribution getting as parameters the mean μ and the standard deviation σ at the site where the wind turbines are installed and the number Nb of wind samples that it is desired to simulate [83]. Also, it is necessary to inspect the power variation of each installed turbine, according to the wind speed [93].

In order to establish the model of wind generation, we will combine the data of the wind resource on the TAZA park with the wind turbines installed there. The distribution of wind at the TAZA site is represented in Figure 5.6.

For this probability distribution, we will consider wind speeds ranging from 0 to 10σ to account the extreme wind variables. The distribution is divided into Nb intervals, with each interval having a length of $10\sigma/Nb$. In our study, the wind resource data is the mean and the standard deviation. The Taza wind distribution requires a mean $\mu = 9m/s$ and standard deviation $\sigma = 2.79m/s$.

5.3.2 Capacity credit calculation

Based on the previous study, we are going to examine the impact of the TAZA park integration to the national electric grid. In addition, the new safety rate will be calculated

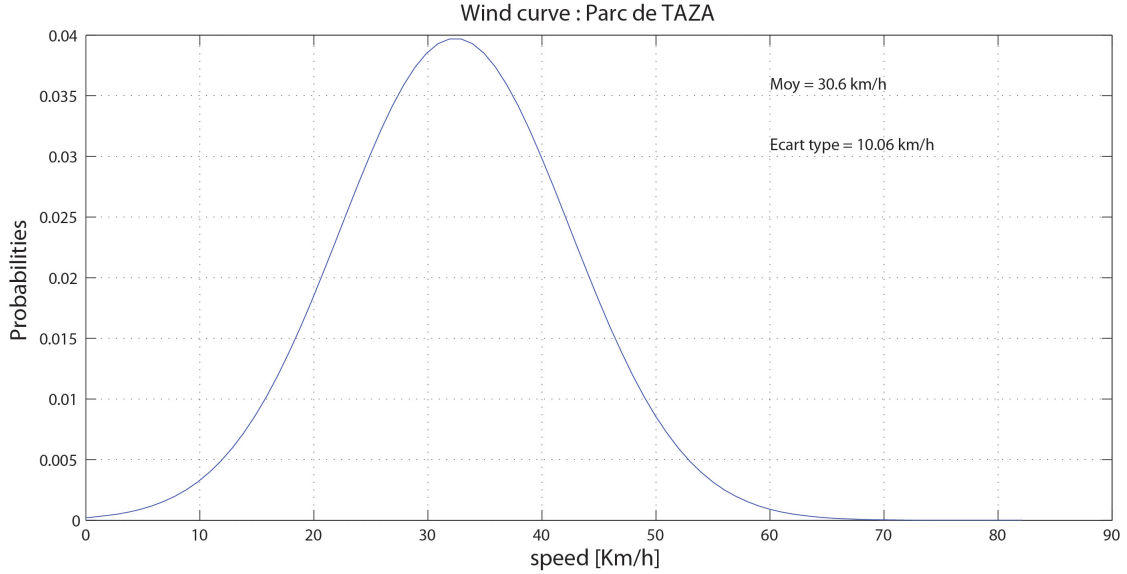


Figure. 5.6. Wind distribution in the TAZA park.

and interpreted. Also, the obtained results are represented in Table 5.3. Subsequently, it will proceed to the calculation of the CC granted to the national electric grid following the introduction of 150 MW of wind energy. The addition of 150 MW of wind in the mix of national production has an impact on improving the safety rate of the electrical system; in effect, the safety rate has increased from 0.0413 h/ year to 0.0398 h/year.

Table. 5.3. Reliability of the hybrid park (conventional + wind).

System	LOLE
National grid + TAZA wind park	0.0398 h/year

In order to analyze the CC of the wind park, we will proceed by the same way as presented above; we will remove a certain capacity of thermal energy and replace it by the wind turbines. Furthermore, using the Matlab program already implemented, we will simulate the different scenarios of existing capacities removed from the national park. The plotted curves in Figure 5.7 are obtained after having to remove simultaneously 30 MW and 33 MW of conventional production capacities; for each case, the simulation was run to calculate the LOLE in function of the injection of [0, 200] MW wind capacity. According to the curves and after the withdrawal of the two conventional capabilities, the LOLE was degraded. However, once the wind parks were injected, the LOLE marked significant improvement.

For those different tests, the TAZA wind farm with its installed capacity of 150 MW may be used to replace only 30 MW units, with the wind power required for the replacement

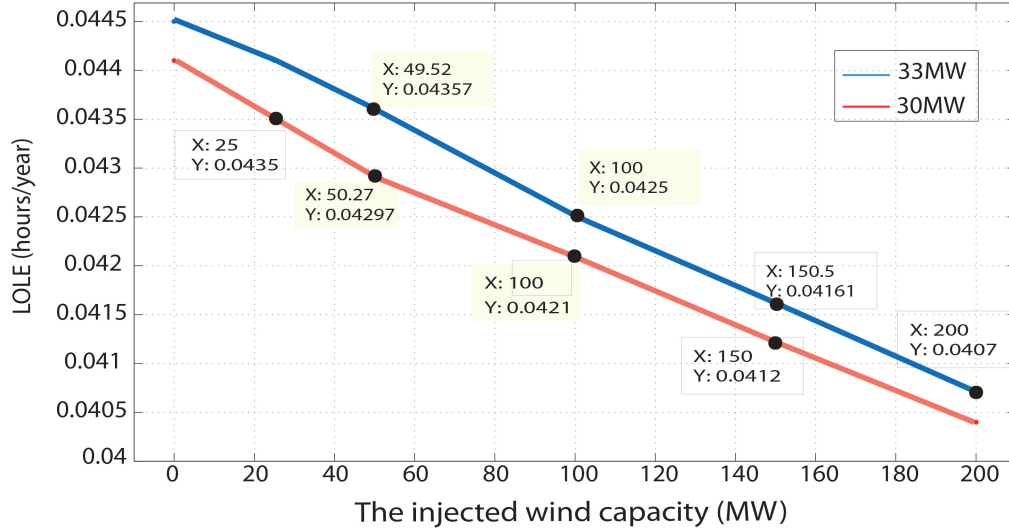


Figure. 5.7. Safety ratio according to the injected wind capacity for 30 MW and 33 MW withdrawn.

is 135 MW that is below 150 MW of the park. As regards the replacement of 33 MW units or more, the number of failure hours in the national grid will increase from 0.0413 to 0.0416 (Figure 5.7). Thus, the TAZA park does not achieve the required level of reliability for the national grid. The results are summarized in Table 5.4.

Table. 5.4. The wind CC of the park of TAZA.

Capacity removed (MW)	Installed wind capacity (MW)	Capacity credit (%)
30	135	22.22
33	160	20.62

5.4 Generalization on the analysis of CC for wind capacity installed on the MNG by 2020

In the previous section, we have studied in detail the integration of TAZA wind farm impact on the safety rate of the national grid, and the conventional production capacity which can be removed without impacting the safety parameters of the grid. In addition, the Moroccan Government envisage the injection of a significant amount of wind parks by the year 2020. Moreover, considering the continuous increase of the annual load consumed at the level of the country, we will go on to consider the impact of all these parks on the national grid in terms of overall operational safety and in terms of the total capacity that can be removed safely.

The Moroccan IEP which consists of injecting a total power of 2000 MW in wind energy before 2020 will contribute certainly in

- Development of Morocco's potential in renewable energy;
- Optimization of fossil source production;
- Postpone the realization of the new conventional power plants of production;
- Improve the safety of the electrical network;
- Improved power quality of electric power served to customers;
- Face the perpetual increase of the annual consumption;
- Winning in the emission of greenhouse gases and contribute to saving our planet against climate change due to greenhouse gases.

The Moroccan IEP is distributed as follows:

- 280MW already achieved and in service;
- 720MW in development by the private sector;
- 1000MW to be built on five new sites, and which will be commissioned between 2018 and 2020 according to the program in Table 5.5.

Table. 5.5. The wind capacities planned to be installed in Morocco before 2020.

Wind farm	Installed power (MW)	Estimated date of commercial exploitation
MIDELT	153.6	30 June 2018
TISKRAD	297.6	30 December 2018
TANGER	99.20	30 June 2018
JBEL LAHDID	201.30	30 June 2019
BOUJDOUR	99.00	30 June 2020

The previous approach to studying the impact of the integration of the TAZA wind farm will be used to determine the operational reliability rate of the power grid, and to calculate the CC. Furthermore, the approach will be used to calculate the CC of wind farms planned to be installed on the national grid before 2020. In a concern to obtain reliable and significant results, the already implemented program is made annually by certain elements, in order to make the assumptions of its functioning closer to reality, particularly:

- The growth rate of demand for energy consumed is about 5%.
- Complete the Matlab program on existing production facilities by means of conventional production facilities which are scheduled to be commissioned before 2020 as shown in Table 5.6.
- As regard the year of study, the wind farms already in operation are well declared in the Matlab program on existing means of production.

Table. 5.6. The conventional capacity installed in Morocco by 2020.

The power stations	Installed power (MW)	Estimated date of commercial exploitation
Coal (Safi)	2×660	31 December 2018
Coal (Jerada)	350 - 135	31 December 2018
Hydraulic (M'dez and El Menzel)	170	31 December 2019

The scenarios decided for the simulation work are as follows:

- The Scenario to add wind capacities of 100, 150, 200, 300, and 1000 MW each time;
- The Scenario to remove from the park of conventional production the respective capacities of 33, 39, 42, 75, 95, 100, 111, 143, 153, and 170 MVA.

The two scenarios were made in order to simulate the wind farms needed to be added before 2020 and to verify the traditional production capacities which can be withdrawn each time following the new integration of the parks. The objective of this work is to

- Calculate the LOLE for each scenario;
- Calculate the wind capacities required to substitute the conventional capacities removed;
- Calculate the CC for different scenarios.

The various simulations realized for the calculation of the safety rate (LOLE) of the electrical system according to the connection of the new wind farms planned before 2020 are represented in Table 5.7, showing that as long as the part of the wind energies increase in the national energy mix, the LOLE improves advantage, since its variation is almost linear, as represented in Figure 5.8.

Table. 5.7. The LOLE (h/year), CC, and the IWC for each conventional capacity removed.

conventional capacities removed (MW)	Injected wind capacities (MW)					CC %	IWC (MW)
	150	300	700	900	1000		
33	0.0417	0.0393	0.0329	0.0297	0.0281	20.62	160
39	0.0430	0.0406	0.0342	0.031	0.0294	19.02	205
42	0.0434	0.0411	0.0346	0.0314	0.0301	20	210
75	0.0454	0.0430	0.0366	0.0334	0.0318	23.07	325
95	0.0470	0.0447	0.0382	0.035	0.0335	23.17	410
100	0.0485	0.0455	0.039	0.0358	0.0343	20.61	485
111	0.0499	0.0471	0.0399	0.0367	0.0351	19.64	565
143	0.0538	0.0508	0.0437	0.0407	0.0383	19.32	740
153	0.0558	0.0530	0.0457	0.0421	0.0403	17.58	870
170	0.0587	0.0555	0.0479	0.0449	0.0418	16.58	1025

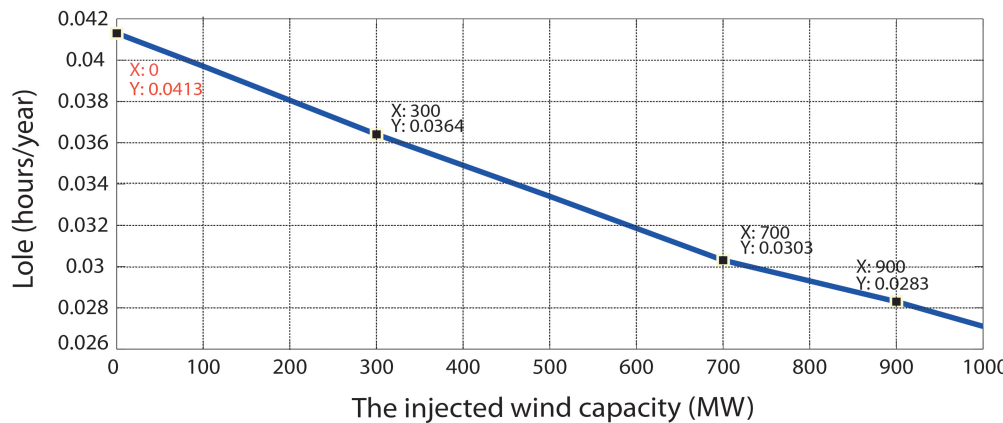


Figure. 5.8. Safety rate (LOLE) according to the injected wind capacity.

The injection of renewable energies based on the wind turbine makes it possible to increase the safety rate of the electrical network in a normal situation and a safe environment. Figure 5.9 shows the simulation results for various scenarios realized in Table 5.7. From the results obtained in Figure 5.9, it can be concluded that

- The advantageous injection of wind energies increases the reliability of the electrical network in an almost linear way.
- In 2020, a scenario is envisaged to substitute a conventional power of about 160 MVA without impacting the safety level of the electrical network. This power is equivalent to two groups of 80 MVA about “ 2×80 MVA”.
- The CC increased until the end of 2017 and subsequently decreased to reach a value in 2020 of 16.58% against a value of 23.17% in 2017. This means that if the wind energy represents a significant part of the mixing energy, we can say that the CC of the wind energy is reduced.

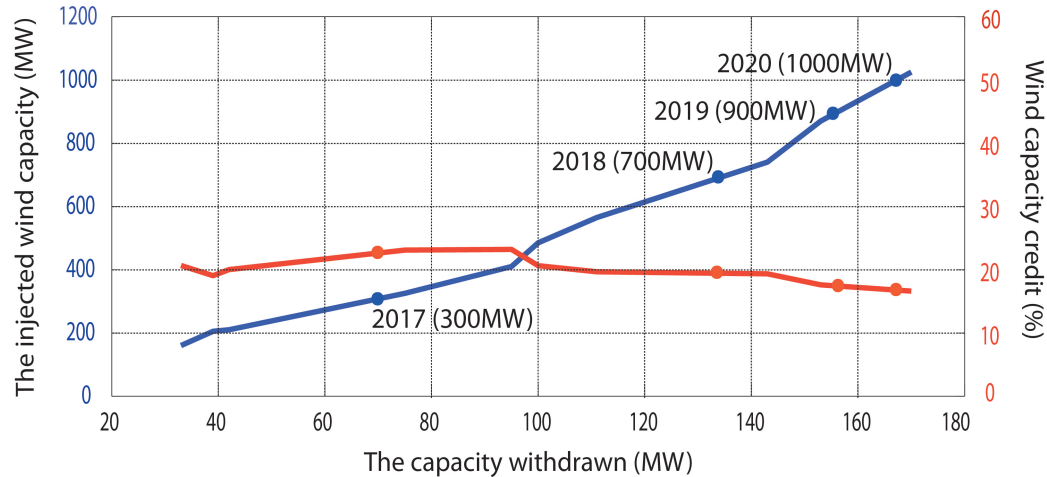


Figure. 5.9. The capacity credit and the wind capacity injected according to the removed conventional capacity.

In the term of this study the Moroccan IEP which aims to achieve a part of wind power of 2000 MW in the national mix energy presents several advantages:

- Allow benefiting from an important level of operating safety of the electrical network;
- Avoid the power supply interruptions in the event of an incident in the grid;
- Allow maintenance operations on conventional production plants, which generally take a long time;
- Benefit from the electrical energy generated from renewable sources with an interesting cost price;
- Adequacy in primary, secondary, and tertiary reserves, this refers to the capacity of the electrical system to cope with any imbalance, for example, in case of an unforeseen change in demand or in case of a loss of production.

5.5 Conclusion

The reliability study conducted in this work has demonstrated that wind energy can contribute to system safety, and replace a part of installed conventional capacity measured by the CC. The CC is estimated basing on the probability of the national grid reliability, which becomes more complex when the system dimension is important. For

this reason, we relied on the existing literature about the reliability and the operation safety, using existing models to deepen them with different parametric criteria. It has also been observed that the CC is reduced linearly according to the injection rate of the wind turbine and is effectively dependent on the conventional power stations considered. Consequently, in a perspective of massive integration of wind power, conventional production will have to be put in place to mitigate the deterioration of CC and preserve the reliability of the system.

This work is published in an indexed journals: [23]

- EL KARKRI, Yassir, EL MAKRINI, Aboubakr, EL MARKHI, Hassane, et al. Assessment of wind power capacity credit in Morocco: Outlook to 2020. Wind Engineering, 2020, vol. 44, no 2, p. 196-207.

Conclusion

This thesis discusses three themes to improve the integration of Grid-connected DFIG-based Wind Turbine. The first contribution deals with the LVRT and HVRT capabilities of wind turbines. Two approaches are proposed in this part. The first one has investigated the performance of the passive and active methods for *FRT* capability of DFIG. Hence, the LVRT strategy is based primarily on the active method, which uses a P controller for controlling the rotor flux; this method is valid only for low voltage dips less than 30%; and for deeper grid faults, an SDBR coupled in series with the stator windings used for the passive method. Besides, the proposed HVRT strategy is based on adding a *DVR*, which provides the balance of the grid voltage by controlling the reactive power. The simulation results have been allowed an indication of the proposed method behavior during any voltage faults. Further, the simulation results obtained using a 1.5MW DFIG connected to the electrical grid report the excellent performance of the proposed strategies for improving the FRT capability of DFIG. The second contribution presents a control algorithm to improve the quality of power and deal with LVRT requirements according to the Spanish grid code. The vector control using the stator-flux-oriented control strategy has been applied to the RSC, and the performance of this control has been verified using DRTS. Moreover, the GSC is controlled to compensate reactive power and reduce the active power oscillations during the unbalanced grid operation. For this reason, the *PR* regulators have been proposed in the stationary reference frame to control the negative- and positive- sequences of the grid currents. The different types of grid voltage sags have been tested. The experiments using CHIL simulation validate the proposed control algorithms for all tests by limiting the grid currents' amplitude, injecting the required reactive power, and stabilizing the active power transferred into the grid. The second part of this thesis introduces a robust and fast diagnosis and fault-tolerant algorithm for DFIG-DC drives. The predictive torque control is applied to the control system. The fault diagnosis has been proposed to be able to detect all types of sensor faults quickly; the proposed algorithm is based just on the measured current, with an exception when lower gain error fault appears, the observed current is used with the measured current in order to ensure the safe and normal system operation. Furthermore, the fault-tolerant strategy is devised based on the fault-index generated by the diagnosis algorithm. When just one sensor is faulty, the healthy sensors are used to recover the faulty one, and when more than one sensor is faulty, the observed currents are used to

replace the faulty signals coming from the measurement. Moreover, the robustness of the proposed algorithm has been experimented by different tests, which confirm that the proposed scheme is independent of the DFIG parameters and the operation mode, and all the mentioned sensor faults can be identified and tolerated accurately.

The last part of this thesis discusses the long-term integration of wind turbines into the Moroccan electrical grid. The reliability study conducted in this part has demonstrated that wind energy can contribute to system safety and replace a part of installed conventional capacity measured by the CC. The CC is estimated in this work basing on the probability of the national grid reliability, which becomes more complicated when the system dimension is essential. For this reason, we relied on the existing literature about reliability and operation safety, using current models to deepen them with different parametric criteria. It has also been observed that the CC is reduced linearly according to the injection rate of the wind turbine and is effectively dependent on the conventional power stations considered. Consequently, in the perspective of the massive integration of wind power, conventional production will have to be put in place to mitigate CC's deterioration and preserve the system's reliability.

Finally two thesis themes are proposed to advance and continue the research work:

Subject 1: Integration of wind turbines based on six-phase DFIG to the grid

- Study of the electrical systems used in wind turbines.
- Study of wind power integration systems for power generation.
- Modeling of six-phase Double Fed Induction Machine.
- Study the impact of grid faults on six-phase DFIG.
- Propose new control strategies for fault ride through capability.

Subject 2: Power quality Improvement of grid connected wind power plants

- Study of the electrical systems used in wind turbines.
- Analysis of power quality in grid connected wind power plant.
- The measurements analysis (voltage and frequency variations, flicker and harmonics.)
- Study of regulatory requirements concerning the power quality of wind turbines.
- Propose new strategies to improve the power quality in grid connected wind power plants.

List of scientific contributions

JCR + Scopus publications

1. Yassir El Karkri 1, Alexis B. Rey-Boué, Hassan EL Moussaoui, Johannes Stöckl and Thomas I. Strasser ” Improved Control of Grid-connected DFIG-based Wind Turbine using Proportional-Resonant Regulators during Unbalanced Grid” Article soumis en Energies (MDPI)
2. Yassir El Karkri, Hassane El Markhi, Tijani Lamhamdi and El Moussaoui Hassan “Assessment of wind power capacity credit in Morocco: Outlook to 2020 ” Wind Engineering journal 2019 (sage track), doi.org/10.1177/0309524X19849835
3. Aboubakr El Makrini, Yassir El Karkri, Youness Boukhriss, Hassane El Markhi, Hassan El Moussaoui “LVRT control strategy of DFIG based wind turbines combining passive and active protection” INTERNATIONAL JOURNAL of RENEWABLE ENERGY RESEARCH, (IJRER, a SCOPUS indexed Journal) page 1258-1269, Vol 7, No 3: September 2017.
4. El Karkri, Yassir., El Markhi, H., El Moussaou, H., Lamhamdi, T. (2018). LVRT and HVRT control strategies of Doubly-Fed Induction Generator. Journal of Electrical Systems, 14(4)
5. El Karkri, Yassir., El Markhi, H., El Moussaou, H., Lamhamdi, T. (2018). ”Robust Current Sensors Fault detection and reconfiguration in DFIG-DC Drives”. (being prepared for submission in IEEE TRANSACTIONS ON INDUSTRIAL ELECTRONICS)

International conference contributions

1. Yassir El Karkri, Tijani Lamhamdi and El Moussaoui Hassan ”High voltage ride-through capability using Dynamic Voltage Restors for doubly fed induction generator” V Jornadas doctorales, Univesidad de Murcia, Espagne, 30mayo 2019.
2. Yassir EL KARKRI, Aboubakr EL MAKRINI, TIJANI LAMHAMDI, Hassane EL MARKHI, and Hassan EL MOUSSAOUI ” Model of Series dynamic resistors with DFIG using for low voltage ride through capability” The 3rd International Conference on Optimization and Application, Meknes, 27-28 Avril 2017.

3. Yassir EL KARKRI, Aboubakr EL MAKRINI, Hassan EL MOUSSAOUI, and Hassane EL MARKHI "High voltage ride-through capability using Dynamic Voltage Restors for doubly fed induction generator based wind turbines" 2ème Colloque Franco-Marocain sur les Energies Renouvelables et leur Intégration aux Réseaux de Transport et de Distribution, Fez, 11-13 Avril 2017.
4. Yassir El Karkri, Hassane El Markhi, Tijani Lamhamdi and El Moussaoui Hassan "A comparison between Series Dynamic Resistors and CROWBAR circuit protection for LVRT capability of Doubly Fed Induction Generator "The International Conference on Renewable Energy and Energy Efficiency FST Fez, November 8 & 9, 2017.
5. Yassir El Karkri, Hassane El Markhi, Hassan El Moussaoui and Tijani Lamhamdi "évaluation du credit de capacite eolien – cas du reseau national marocain rnma" 3 ème Rencontre Nationale des Jeunes Chercheurs en Sciences de l'Ingénieur (RNJC'2017).
6. Yassir El Karkri, Hassane El Markhi, Hassan El Moussaoui and Tijani Lamhamdi" l'integration des eoliennes au reseau electrique "Workshop sur La Gestion des Energies Renouvelables : Enjeux et Perspectives,15 Mai 2017.
7. Yassir El Karkri, Azeroual Mohamed,Hassane El Markhi, Hassan El Moussaoui and Tijani Lamhamdi "Fault Ride-Through control strategy of Double-Fed Induction Generator" 4 ème journée scientifique sur les énergies renouvelables à l'EST de Fès, le 2 Novembre 2017.

Bibliography

- [1] A. Khedher, N. Khemiri, and M. F. Mimouni, “Wind energy conversion system using dfig controlled by backstepping and sliding mode strategies,” *International Journal of Renewable Energy Research (IJRER)*, vol. 2, no. 3, pp. 421–430, 2012.
- [2] T. Ayodele, A. Jimoh, J. Munda, and J. Agee, “Challenges of grid integration of wind power on power system grid integrity: A review,” *world*, vol. 3, 2020.
- [3] A. El Makrini, Y. El Karkri, Y. Boukhriss, H. El Markhi, and H. El Moussaoui, “Lvrt control strategy of dfig based wind turbines combining passive and active protection,” *International Journal of Energy Research*, vol. 7, pp. 1258–1269, 2017.
- [4] P. Kumar and A. K. Singh, “Grid codes: goals and challenges,” in *Renewable Energy Integration*, pp. 17–39, Springer, 2014.
- [5] K. R. Reddy, N. R. Babu, and P. Sanjeevikumar, “A review on grid codes and reactive power management in power grids with wecs,” in *Advances in Smart Grid and Renewable Energy*, pp. 525–539, Springer, 2018.
- [6] R. Perveen, N. Kishor, and S. R. Mohanty, “Off-shore wind farm development: Present status and challenges,” *Renewable and Sustainable Energy Reviews*, vol. 29, pp. 780–792, 2014.
- [7] Y. Boukhris, A. El Makrini, H. El Moussaoui, and H. El Markhi, “Low voltage ride-through capability enhancement of doubly fed induction generator based wind turbines under voltage dips,” *International Journal of Power Electronics and Drive Systems*, vol. 6, no. 4, 2015.
- [8] S. Toumi, Y. Amirat, E. Elbouchikhi, M. Trabelsi, M. Benbouzid, and M. F. Mimouni, “A comparison of fault-tolerant control strategies for a pmsg-based marine

- current turbine system under generatorside converter faulty conditions.,” *Journal of Electrical Systems*, vol. 13, no. 3, 2017.
- [9] E. Ganji and M. Mahdavian, “A controlling method of dfig-based wind turbine for stability improvement of power delivery to the power grid.,” *Journal of Electrical Systems*, vol. 12, no. 3, 2016.
- [10] M. Mohseni and S. M. Islam, “Transient control of dfig-based wind power plants in compliance with the australian grid code,” *IEEE Transactions on Power Electronics*, vol. 27, no. 6, pp. 2813–2824, 2011.
- [11] Y. El Karkri, H. El Markhi, H. El Moussaou, and T. Lamhamdi, “LVRT and HVRT control strategies of doubly-fed induction generator,” *Journal of Electrical Systems*, vol. 14, no. 4, pp. 1–20, 2018.
- [12] J. Faiz and S. Moosavi, “Eccentricity fault detection—from induction machines to dfig—a review,” *Renewable and Sustainable Energy Reviews*, vol. 55, pp. 169–179, 2016.
- [13] A. Subramaniam, A. Sahoo, S. S. Manohar, and S. K. Panda, “Fault diagnostic techniques for induction machines through finite element analysis,” in *2017 20th International Conference on Electrical Machines and Systems (ICEMS)*, pp. 1–4, IEEE, 2017.
- [14] A. Corne, N. Yang, J.-P. Martin, B. Nahid-Mobarakeh, and S. Pierfederici, “Non-linear estimation of stator currents in a wound rotor synchronous machine,” *IEEE Transactions on Industry Applications*, vol. 54, no. 4, pp. 3858–3867, 2018.
- [15] I. Karray, K. B. Kilani, and M. Elleuch, “Advanced controls for wind power plant ancillary services,” in *International Conference on Electrical Engineering and Control Applications*, pp. 277–292, Springer, 2017.
- [16] Z. Gao, C. Cecati, and S. X. Ding, “A survey of fault diagnosis and fault-tolerant techniques—part i: Fault diagnosis with model-based and signal-based approaches,” *IEEE Transactions on Industrial Electronics*, vol. 62, no. 6, pp. 3757–3767, 2015.
- [17] N. Zhang, H. Tang, and C. Yao, “A systematic method for designing a pr controller and active damping of the lcl filter for single-phase grid-connected pv inverters,” *Energies*, vol. 7, no. 6, pp. 3934–3954, 2014.

- [18] E. Afshari, G. R. Moradi, R. Rahimi, B. Farhangi, Y. Yang, F. Blaabjerg, and S. Farhangi, “Control strategy for three-phase grid-connected pv inverters enabling current limitation under unbalanced faults,” *IEEE Transactions on Industrial Electronics*, vol. 64, no. 11, pp. 8908–8918, 2017.
- [19] N. Guerrero-Rodríguez, L. Herrero-de Lucas, S. de Pablo-Gómez, and A. B. Rey-Boué, “Performance study of a synchronization algorithm for a 3-phase photovoltaic grid-connected system under harmonic distortions and unbalances,” *Electric power systems research*, vol. 116, pp. 252–265, 2014.
- [20] Y. El Karkri, A. B. Rey-Boué, H. El Moussaoui, J. Stöckl, and T. I. Strasser, “Improved control of grid-connected dfig-based wind turbine using proportional-resonant regulators during unbalanced grid,” *Energies*, vol. 12, no. 21, p. 4041, 2019.
- [21] “National office of electricity.” <http://www.one.org.ma/>. Accessed: 2018-12-30.
- [22] “Étude d’interconnexion des réseaux électriques sénégal – mauritanie – maroc - espagne.” http://www.renow.itccanarias.org/images/policy/senegal/Secteur_electrique/Etude_dinterconnexion_des_reseaux_electriques_Senegal_Mauritanie_Maroc_Espagne.pdf. Accessed: 2018-12-30.
- [23] Y. El Karkri, A. El Makrini, H. El Markhi, T. Lamhamdi, and H. El Moussaoui, “Assessment of wind power capacity credit in morocco: Outlook to 2020,” *Wind Engineering*, vol. 44, no. 2, pp. 196–207, 2020.
- [24] G. Yuan and R. Liang, “A dfig wind turbine low-voltage ride-through control strategy based on resynchronization of rotor side converter,” in *2017 China International Electrical and Energy Conference (CIEEC)*, pp. 351–355, IEEE, 2017.
- [25] M. Rahimi and M. Parniani, “Low voltage ride-through capability improvement of dfig-based wind turbines under unbalanced voltage dips,” *International Journal of Electrical Power & Energy Systems*, vol. 60, pp. 82–95, 2014.
- [26] Y. El Karkri, H. El Markhi, T. Lamhamdi, and H. El Moussaoui, “A comparison between series dynamic resistors and crowbar circuit protection for lvrt capability of doubly-fed induction generator,” in *IOP Conference Series: Earth and Environmental Science*, vol. 161, 2018.

- [27] S. I. Gkavanoudis and C. S. Demoulias, "A combined fault ride-through and power smoothing control method for full-converter wind turbines employing supercapacitor energy storage system," *Electric Power Systems Research*, vol. 106, pp. 62–72, 2014.
- [28] D. Ramirez, S. Martinez, F. Blazquez, and C. Carrero, "Use of statcom in wind farms with fixed-speed generators for grid code compliance," *Renewable Energy*, vol. 37, no. 1, pp. 202–212, 2012.
- [29] T. Long, S. Shao, P. Malliband, E. Abdi, and R. A. McMahon, "Crowbarless fault ride-through of the brushless doubly fed induction generator in a wind turbine under symmetrical voltage dips," *IEEE Transactions on Industrial Electronics*, vol. 60, no. 7, pp. 2833–2841, 2012.
- [30] P. S. Flannery and G. Venkataramanan, "A fault tolerant doubly fed induction generator wind turbine using a parallel grid side rectifier and series grid side converter," *IEEE Transactions on power electronics*, vol. 23, no. 3, pp. 1126–1135, 2008.
- [31] J. G. Nielsen and F. Blaabjerg, "A detailed comparison of system topologies for dynamic voltage restorers," *IEEE Transactions on Industry Applications*, vol. 41, no. 5, pp. 1272–1280, 2005.
- [32] H. Hatami, F. Shahnia, A. Pashaei, and S. Hosseini, "Investigation on d-statcom and dvr operation for voltage control in distribution networks with a new control strategy," in *2007 IEEE Lausanne Power Tech*, pp. 2207–2212, IEEE, 2007.
- [33] A. Y. Abdelaziz, A. M. Ibrahim, A. M. Asim, A. H. A. Razek, and Y. Hegazy, "Investigation of electrical dynamics of dfig-based wind turbines during severe symmetrical grid voltage dips," in *2012 International Conference on Engineering and Technology (ICET)*, pp. 1–6, IEEE, 2012.
- [34] S.-Y. Li, Y. Sun, T. Wu, Y.-Z. Liang, X. Yu, and J.-M. Zhang, "Analysis of low voltage ride through capability in wind turbine based on dfig," in *2010 International Conference on Electrical and Control Engineering*, pp. 3331–3334, IEEE, 2010.
- [35] M. Chowdhury, N. Hosseinzadeh, M. Billah, and S. Haque, "Dynamic dfig wind farm model with an aggregation technique," in *International Conference on Electrical & Computer Engineering (ICECE 2010)*, pp. 330–333, IEEE, 2010.

- [36] X. Bian, C. Tse, C. Chung, and K. Wang, "Dynamic modeling of large scale power system with facts and dfig type wind turbine," in *The 2nd International Symposium on Power Electronics for Distributed Generation Systems*, pp. 753–758, IEEE, 2010.
- [37] I.-W. Joo, H.-S. Song, and K. Nam, "Source-voltage-sensorless scheme for pwm rectifier under voltage unbalance condition," in *4th IEEE International Conference on Power Electronics and Drive Systems. IEEE PEDS 2001-Indonesia. Proceedings (Cat. No. 01TH8594)*, vol. 1, pp. 33–38, IEEE, 2001.
- [38] H.-s. Song and K. Nam, "Dual current control scheme for pwm converter under unbalanced input voltage conditions," *IEEE transactions on industrial electronics*, vol. 46, no. 5, pp. 953–959, 1999.
- [39] L. Xu, B. R. Andersen, and P. Cartwright, "Vsc transmission operating under unbalanced ac conditions-analysis and control design," *IEEE transactions on Power Delivery*, vol. 20, no. 1, pp. 427–434, 2005.
- [40] I. Etxeberria-Otadui, U. Viscarret, M. Caballero, A. Rufer, and S. Bacha, "New optimized pwm vsc control structures and strategies under unbalanced voltage transients," *IEEE Transactions on Industrial Electronics*, vol. 54, no. 5, pp. 2902–2914, 2007.
- [41] M. Liserre, R. Teodorescu, and F. Blaabjerg, "Multiple harmonics control for three-phase grid converter systems with the use of pi-res current controller in a rotating frame," *IEEE Transactions on power electronics*, vol. 21, no. 3, pp. 836–841, 2006.
- [42] J.-b. Hu, Y.-k. He, and H. Nian, "Enhanced control of dfig-used back-to-back pwm vsc under unbalanced grid voltage conditions," *Journal of Zhejiang University-Science A*, vol. 8, no. 8, pp. 1330–1339, 2007.
- [43] G. Iwanski and W. Koczara, "Sensorless direct voltage control method for stand-alone slip-ring induction generator," in *2005 European Conference on Power Electronics and Applications*, pp. 10–pp, IEEE, 2005.
- [44] F. Martinez-Rodrigo, D. Ramirez, A. B. Rey-Boue, S. De Pablo, and L. C. Herrero-de Lucas, "Modular multilevel converters: Control and applications," *Energies*, vol. 10, no. 11, p. 1709, 2017.

- [45] L. R. Limongi, R. Bojoi, G. Griva, and A. Tenconi, “Digital current-control schemes,” *IEEE industrial electronics magazine*, vol. 3, no. 1, pp. 20–31, 2009.
- [46] N. Jaalam, N. Rahim, A. Bakar, and B. Eid, “Strategy to enhance the low-voltage ride-through in photovoltaic system during multi-mode transition,” *Solar Energy*, vol. 153, pp. 744–754, 2017.
- [47] Y. Liao, H. Li, J. Yao, and K. Zhuang, “Operation and control of a grid-connected dfig-based wind turbine with series grid-side converter during network unbalance,” *Electric Power Systems Research*, vol. 81, no. 1, pp. 228–236, 2011.
- [48] S. Baros and M. Ilić, “Robust ectropy-based cooperative control of a wind dfig for transient stabilization and mppt,” in *2015 IEEE Power & Energy Society General Meeting*, pp. 1–5, IEEE, 2015.
- [49] A. B. Rey-Boue, F. Martinez-Rodrigo, N. Guerrero-Rodríguez, L. C. Herrero-de Lucas, and S. de Pablo, “Enhanced controller for grid-connected modular multilevel converters in distorted utility grids,” *Electric Power Systems Research*, vol. 163, pp. 310–327, 2018.
- [50] S. Gulur, V. M. Iyer, and S. Bhattacharya, “Proportional integral—resonant and dual loop current control structure comparison for grid connected converters in the rotating frame,” in *2018 IEEE Applied Power Electronics Conference and Exposition (APEC)*, pp. 1617–1623, IEEE, 2018.
- [51] E. Gómez, J. Fuentes, A. Molina-García, F. Ruz, and F. Jiménez, “Field tests of wind turbines submitted to real voltage dips under the new spanish grid code requirements,” *Wind Energy: An International Journal for Progress and Applications in Wind Power Conversion Technology*, vol. 10, no. 5, pp. 483–495, 2007.
- [52] D. Santos-Martin, J. Alonso-Martinez, J. E.-G. Carrasco, and S. Arnaltes, “Problem-based learning in wind energy using virtual and real setups,” *IEEE Transactions on Education*, vol. 55, no. 1, pp. 126–134, 2011.
- [53] C. Liu, B. Chen, M. Cheng, A. Champagne, and K. Patel, “Model integration and hardware-in-the-loop (hil) simulation design for the testing of electric power steering controllers,” tech. rep., SAE Technical Paper, 2016.

- [54] T. Chun, M. Choi, and K. Kim, "A programmable low-pass filter based stator flux calculation for a direct vector control of induction motor," in *Proceedings Third Russian-Korean International Symposium on Science and Technology. KORUS'99 (Cat. No. 99EX362)*, vol. 2, pp. 722–726, IEEE, 1999.
- [55] M. Lemaire, P. Sicard, and J. Belanger, "Prototyping and testing power electronics systems using controller hardware-in-the-loop (hil) and power hardware-in-the-loop (phil) simulations," in *2015 IEEE Vehicle Power and Propulsion Conference (VPPC)*, pp. 1–6, IEEE, 2015.
- [56] H. Kakigano, Y. Miura, and T. Ise, "Low-voltage bipolar-type dc microgrid for super high quality distribution," *IEEE transactions on power electronics*, vol. 25, no. 12, pp. 3066–3075, 2010.
- [57] G. Marques and M. F. Iacchetti, "A self-sensing stator-current-based control system of a dfig connected to a dc-link," *IEEE Transactions on Industrial Electronics*, vol. 62, no. 10, pp. 6140–6150, 2015.
- [58] F. Blaabjerg, Z. Chen, and S. B. Kjaer, "Power electronics as efficient interface in dispersed power generation systems," *IEEE transactions on power electronics*, vol. 19, no. 5, pp. 1184–1194, 2004.
- [59] S. M. Cruz, G. D. Marques, P. F. Gonçalves, and M. F. Iacchetti, "Predictive torque and rotor flux control of a dfig-dc system for torque ripple compensation and loss minimization," *IEEE Transactions on Industrial Electronics*, vol. 65, no. 12, pp. 9301–9310, 2018.
- [60] S. Karimi, A. Gaillard, P. Poure, and S. Saadate, "Current sensor fault-tolerant control for wecs with dfig," *IEEE Transactions on Industrial Electronics*, vol. 56, no. 11, pp. 4660–4670, 2009.
- [61] K. Rothenhagen and F. W. Fuchs, "Doubly fed induction generator model-based sensor fault detection and control loop reconfiguration," *IEEE Transactions on Industrial Electronics*, vol. 56, no. 10, pp. 4229–4238, 2009.
- [62] G. H. B. Foo, X. Zhang, and D. M. Vilathgamuwa, "A sensor fault detection and isolation method in interior permanent-magnet synchronous motor drives based on an extended kalman filter," *IEEE Transactions on Industrial Electronics*, vol. 60, no. 8, pp. 3485–3495, 2013.

- [63] N. M. Freire, J. O. Estima, and A. J. M. Cardoso, “A new approach for current sensor fault diagnosis in pmsg drives for wind energy conversion systems,” *IEEE Transactions on Industry Applications*, vol. 50, no. 2, pp. 1206–1214, 2013.
- [64] C. Chakraborty and V. Verma, “Speed and current sensor fault detection and isolation technique for induction motor drive using axes transformation,” *IEEE Transactions on Industrial Electronics*, vol. 62, no. 3, pp. 1943–1954, 2014.
- [65] P. M. Papadopoulos, L. Hadjidemetriou, E. Kyriakides, and M. M. Polycarpou, “Robust fault detection, isolation, and accommodation of current sensors in grid side converters,” *IEEE Transactions on Industry Applications*, vol. 53, no. 3, pp. 2852–2861, 2016.
- [66] Y. Yu, Y. Zhao, B. Wang, X. Huang, and D. Xu, “Current sensor fault diagnosis and tolerant control for vsi-based induction motor drives,” *IEEE Transactions on Power Electronics*, vol. 33, no. 5, pp. 4238–4248, 2017.
- [67] C. Wu, C. Guo, Z. Xie, F. Ni, and H. Liu, “A signal-based fault detection and tolerance control method of current sensor for pmsm drive,” *IEEE Transactions on Industrial Electronics*, vol. 65, no. 12, pp. 9646–9657, 2018.
- [68] X. Wang, Z. Wang, Z. Xu, M. Cheng, W. Wang, and Y. Hu, “Comprehensive diagnosis and tolerance strategies for electrical faults and sensor faults in dual three-phase pmsm drives,” *IEEE Transactions on Power Electronics*, vol. 34, no. 7, pp. 6669–6684, 2018.
- [69] K. Xiahou, Y. Liu, L. Wang, M. Li, and Q. Wu, “Switching fault-tolerant control for dfig-based wind turbines with rotor and stator current sensor faults,” *IEEE Access*, vol. 7, pp. 103390–103403, 2019.
- [70] K. Xiahou, X. Lin, and Q. Wu, “Current sensor fault-tolerant control of dfigs using stator current regulators and kalman filters,” in *2017 IEEE Power & Energy Society General Meeting*, pp. 1–5, IEEE, 2017.
- [71] I. Bahri, M.-W. Naouar, I. Slama-Belkhodja, and E. Monmasson, “Fpga-based fdi of faulty current sensor in current controlled pwm converters,” in *EUROCON 2007-The International Conference on” Computer as a Tool”*, pp. 1679–1686, IEEE, 2007.

- [72] M. Dybkowski and K. Klimkowski, "Stator current sensor fault detection and isolation for vector controlled induction motor drive," in *2016 IEEE International Power Electronics and Motion Control Conference (PEMC)*, pp. 1097–1102, IEEE, 2016.
- [73] K.-S. Lee and J.-S. Ryu, "Instrument fault detection and compensation scheme for direct torque controlled induction motor drives," *IEE Proceedings-Control Theory and Applications*, vol. 150, no. 4, pp. 376–382, 2003.
- [74] T. Kousksou, P. Bruel, A. Jamil, T. El Rhafiki, and Y. Zeraouli, "Energy storage: Applications and challenges," *Solar Energy Materials and Solar Cells*, vol. 120, pp. 59–80, 2014.
- [75] M. Azeroual, A. El Makrini, H. El Moussaoui, and H. EL MARKHI, "Renewable energy potential and available capacity for wind and solar power in morocco towards 2030.," *Journal of Engineering Science & Technology Review*, vol. 11, no. 1, 2018.
- [76] "Intégration des énergies renouvelables dans les systèmes électriques nationaux." <http://www.cop22.org/fr>. Accessed: 2018-12-30.
- [77] K. Choukri, A. Naddami, and S. Hayani, "Renewable energy in emergent countries: lessons from energy transition in morocco," *Energy, Sustainability and Society*, vol. 7, no. 1, p. 25, 2017.
- [78] T. Kousksou, A. Allouhi, M. Belattar, A. Jamil, T. El Rhafiki, A. Arid, and Y. Zeraouli, "Renewable energy potential and national policy directions for sustainable development in morocco," *Renewable and Sustainable Energy Reviews*, vol. 47, pp. 46–57, 2015.
- [79] A. Bloess, W.-P. Schill, and A. Zerrahn, "Power-to-heat for renewable energy integration: A review of technologies, modeling approaches, and flexibility potentials," *Applied Energy*, vol. 212, pp. 1611–1626, 2018.
- [80] R. R. Appino, J. Á. G. Ordiano, R. Mikut, T. Faulwasser, and V. Hagenmeyer, "On the use of probabilistic forecasts in scheduling of renewable energy sources coupled to storages," *Applied energy*, vol. 210, pp. 1207–1218, 2018.

- [81] R. M. Castro and L. A. Ferreira, "A comparison between chronological and probabilistic methods to estimate wind power capacity credit," *IEEE Transactions on Power Systems*, vol. 16, no. 4, pp. 904–909, 2001.
- [82] C. T. Clack, S. A. Qvist, J. Apt, M. Bazilian, A. R. Brandt, K. Caldeira, S. J. Davis, V. Diakov, M. A. Handschy, P. D. Hines, *et al.*, "Evaluation of a proposal for reliable low-cost grid power with 100% wind, water, and solar," *Proceedings of the National Academy of Sciences*, vol. 114, no. 26, pp. 6722–6727, 2017.
- [83] R. Karki and P. Hu, "Impact of wind power growth on capacity credit," in *2007 Canadian Conference on Electrical and Computer Engineering*, pp. 1586–1589, IEEE, 2007.
- [84] K. R. Voorspools and W. D. D'haeseleer, "An analytical formula for the capacity credit of wind power," *Renewable Energy*, vol. 31, no. 1, pp. 45–54, 2006.
- [85] R. N. Allan, R. Billinton, I. Sjariel, L. Goel, and K. So, "A reliability test system for educational purposes-basic distribution system data and results," *IEEE Transactions on Power systems*, vol. 6, no. 2, pp. 813–820, 1991.
- [86] R. Allan and R. Billinton, "Probabilistic assessment of power systems," *Proceedings of the IEEE*, vol. 88, no. 2, pp. 140–162, 2000.
- [87] C. L. T. Borges and J. A. Dias, "A model to represent correlated time series in reliability evaluation by non-sequential monte carlo simulation," *IEEE Transactions on Power Systems*, vol. 32, no. 2, pp. 1511–1519, 2016.
- [88] R. Billinton, H. Chen, and R. Ghajar, "A sequential simulation technique for adequacy evaluation of generating systems including wind energy," *IEEE Transactions on Energy Conversion*, vol. 11, no. 4, pp. 728–734, 1996.
- [89] K. Schenk, R. Misra, S. Vassos, and W. Wen, "A new method for the evaluation of expected energy generation and loss of load probability," *IEEE transactions on power apparatus and systems*, no. 2, pp. 294–303, 1984.
- [90] W. Wangdee and R. Billinton, "Considering load-carrying capability and wind speed correlation of wecs in generation adequacy assessment," *IEEE Transactions on Energy Conversion*, vol. 21, no. 3, pp. 734–741, 2006.

- [91] C. Singh and Y. Kim, “An efficient technique for reliability analysis of power systems including time dependent sources,” *IEEE Transactions on Power Systems*, vol. 3, no. 3, pp. 1090–1096, 1988.
- [92] O. J. Mengshoel, M. Chavira, K. Cascio, S. Poll, A. Darwiche, and S. Uckun, “Probabilistic model-based diagnosis: An electrical power system case study,” *IEEE Transactions on Systems, Man, and Cybernetics-Part A: Systems and Humans*, vol. 40, no. 5, pp. 874–885, 2010.
- [93] Y. Yang, H. Wang, A. Sangwongwanich, and F. Blaabjerg, “Design for reliability of power electronic systems,” in *Power electronics handbook*, pp. 1423–1440, Elsevier, 2018.
- [94] C. PS, *Electric power systems: advanced forecasting techniques and optimal generation scheduling*. CRC press, 2017.
- [95] R. Karki, P. Hu, and R. Billinton, “A simplified wind power generation model for reliability evaluation,” *IEEE transactions on Energy conversion*, vol. 21, no. 2, pp. 533–540, 2006.